The Astrophysical Journal, 920:137 (35pp), 2021 October 20 https://doi.org/10.3847/1538-4357/ac1351

Say Hello to Algol's New Companion Candidates

Lauri Jetsu
Department of Physics, P.O. Box 64, FI-00014, University of Helsinki, Finland; lauri.jetsu@helsinki.fi

Received 2020 May 27; revised 2021 July 8; accepted 2021 July 8; published 2021 October 22

Abstract

Constant orbital period ephemerides of eclipsing binaries give the computed eclipse epochs (C). These ephemerides based on the old data cannot accurately predict the observed future eclipse epochs (O). Predictability can be improved by removing linear or quadratic trends from the $O-C$ data. Additional companions in an eclipsing binary system cause light-time travel effects that are observed as strictly periodic $O-C$ changes. Recently, Hajdu et al. estimated that the probability of detecting the periods of two new companions from the $O-C$ data is only 0.00005. We apply the new discrete chi-square method to 236 yr of $O-C$ data of the eclipsing binary Algol (β Persei). We detect the tentative signals of at least five companion candidates having periods between 1.863 and 219.0 yr. The weakest one of these five signals does not reveal a "new" companion candidate, because its 680.4 ± 0.4 day signal period differs only 1.4σ from the well-known 679.85 ± 0.04 day orbital period of Algol C. We detect these same signals also from the first 226.2 yr of data, and they give an excellent prediction for the last 9.2 yr of our data. The orbital planes of Algol C and the new companion candidates are probably coplanar because no changes have been observed in Algol's eclipses. The 2.867 day orbital period has been constant since it was determined by Goodricke.

Unified Astronomy Thesaurus concepts: Astronomy data analysis (1858); Eclipsing binary stars (444); Algol variable stars (24); Time series analysis (1916); Multiple stars (1081)

1. Introduction

The oldest preserved historical document of the discovery of a variable star is the ancient Egyptian papyrus Cairo 86637, where naked-eye observations of Algol's eclipses have been recorded into the Calendar of Lucky and Unlucky days (Porceddu et al. 2008, 2018; Jetsu et al. 2013; Jetsu & Porceddu 2015). Montanari re-discovered its variability in the year 1669. Goodricke (1783) determined the orbital period $P_{\rm orb} = 2\overset{\rm d}{.}867$ of this eclipsing binary (EB). The close-orbit eclipsing stars are Algol A (B8 V) and Algol B (K2 IV). Curtiss (1908) discovered the $1\overset{\rm y}{.}863$ wide-orbit third companion Algol C (K2 IV). Direct interferometric images of these three members have been obtained (e.g., Zavala et al. 2010; Baron et al. 2012).

Periodic long-term changes occur in the observed (O) minus the computed (C) primary eclipse epochs of EBs. The most probable causes are a third body (e.g., Li et al. 2018), a magnetic activity cycle (e.g., Applegate 1992), or an apsidal motion (e.g., Borkovits et al. 2005). Hajdu et al. (2019) searched for third bodies in a large sample of 80,000 EBs. They detected 992 triple systems from the $O-C$ data, and only 4 candidates that may have a fourth body. Their fourth-body detection rate was $4/80{,}000 = 0.00005$. Recently, Jetsu (2020, hereafter Paper I) formulated the new discrete chi-square method (DCM). He applied DCM to the $O-C$ data of XZ And and detected the periods of a third and a fourth body.

In Algol, the mass transfer from the less massive Algol B ($0.8m_{\odot}$) to the more massive Algol A ($3.7m_{\odot}$) should cause a long-term $P_{\rm orb}$ period increase (Kwee 1958), which should have been observed as quadratic long-term $O-C$ changes (Kiseleva et al. 1998). Long-term $P_{\rm orb}$ increase or quadratic $O-C$ changes have not been observed in Algol since its period was determined 238 yr ago. However, its orbital period modulation does cause negative and positive $O-C$ changes. The short-term low amplitude $O-C$ changes follow $1\overset{\rm y}{.}863$ orbital motion cycle of Algol C, while the high-amplitude $O-C$ changes follow $30^{\rm y}$ and $200^{\rm y}$ quasi-periodic activity cycles (Applegate 1992). The physical origin of period changes is not fully understood, because Algol's puzzling $O-C$ diagram contains unknown signals and trends (e.g., Frieboes-Conde et al. 1970; Applegate 1992). We apply DCM to Algol's $O-C$ data because this method can detect many signals superimposed on unknown trends.

Kim et al. (2018) note that their TIDAK database $O-C$ ephemerides "cannot be used for the prediction of future times of the primary or secondary minima." These ephemerides are determined by eliminating linear or quadratic trends from the available $O-C$ data (Kreiner et al. 2001). They usually need to be redetermined when new data are obtained. Although the $O-C$ changes caused by a third body are strictly periodic, the predictions usually fail to separate aperiodic trends from periodic signals (e.g., Bours et al. 2014; Lohr et al. 2015; Song et al. 2019). Furthermore, the detection rate of third bodies from $O-C$ data is extremely low (e.g., Hajdu et al. 2019). Against this background, it is totally unexpected that we can detect numerous periods in Algol's $O-C$ data, as well as predict its $O-C$ changes.

We present our most important results in main text Figures 1–3 and Table 1. We describe Figures A1–A3 and Tables A1–A3 inthe beginning of our Appendix. The remaining appendix Figures A4–A15 and Tables A4–A15 are described in the main text.

2. Data

The epochs of the observed light-curve minima give the observed (O) values. We obtained the $n = 2238$ observed eclipse epochs of Algol from the 2018 version of the TIDAK database (Kim et al. 2018). These eclipse epochs have been determined by hundreds of astronomers during the past two centuries. The nights when these eclipses could be observed

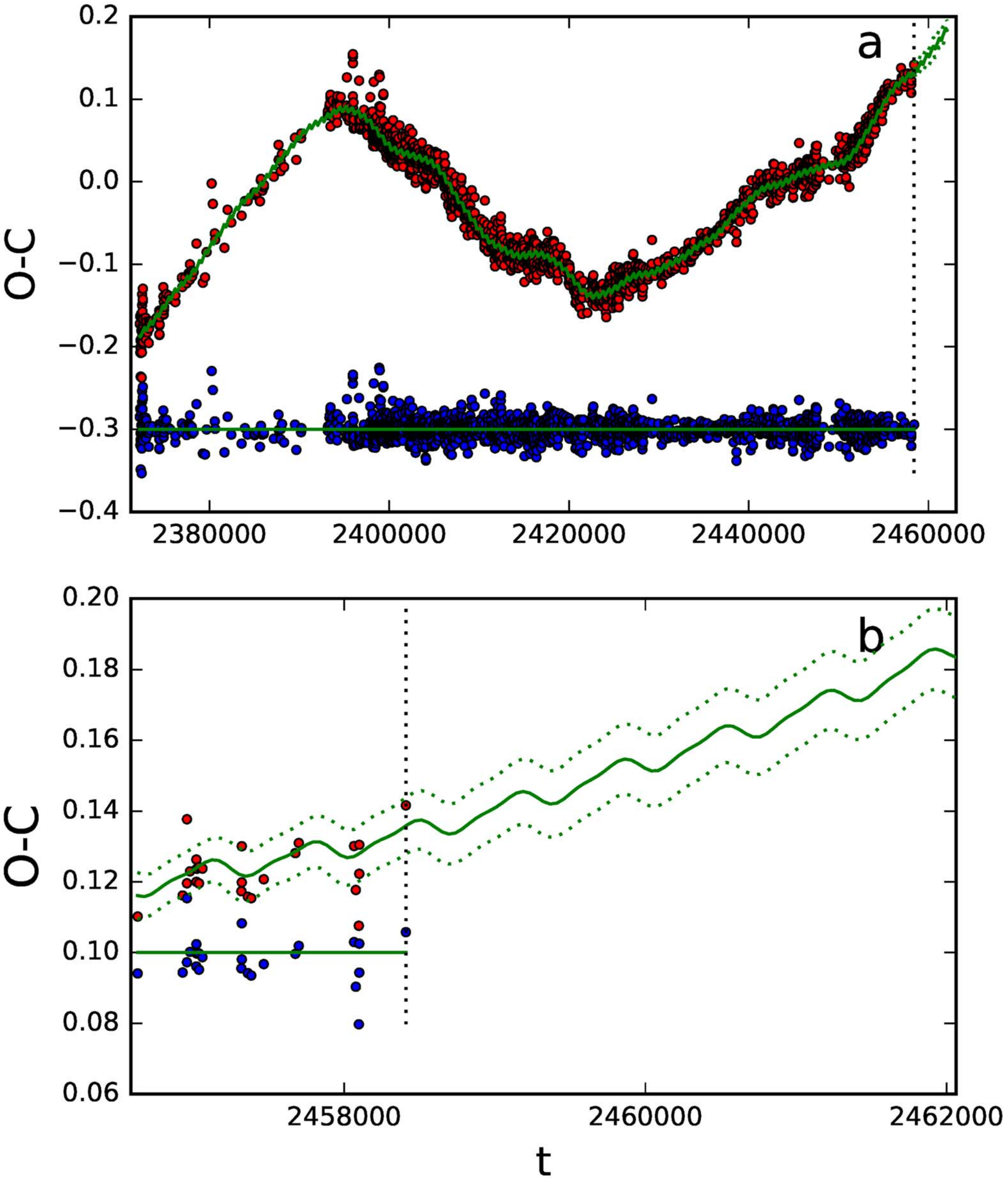

Figure 1. All data: eccentric orbit analysis (Section 5.1.2). (a) Best five-signal $\mathcal{M} = 3 + 6$ model, the sum of the three-signal model $\mathcal{M} = 3$ for original data and two-signal $\mathcal{M} = 6$ model for residuals (green continuous curve), is overplotted on all $O - C$ data (red dots). Residuals (blue dots) are offset to level −0.3 (horizontal line). Notice the tiny flickering caused by 127 rotations of Algol C around Algol AB. The vertical dotted line marks the last observation (2018 October 18), where prediction for the next 10 yr begins. (b) Previous 5 yr of data and residuals (red and blue circles). Residuals are offset to level +0.10 (horizontal line). Continuous and dotted green lines denote the $\mathcal{M} = 3 + 6$ model and its $\pm 3\sigma$ error limits. Units are $[t]$ = HJD and $[O - C]$ = (days).

were known beforehand. Every eclipse lasted eight hours. Both dimming and brightening took four hours. The probability for a negative or positive mid-eclipse epoch error was the same, because the eclipse light curve was symmetric. It is therefore probable that the observational errors follow a Gaussian distribution, the epoch values contain no observational trends, and the observational errors are not heteroskedastic. Naturally, the accuracy of these data improves toward modern times, because the observational techniques have improved. We study only the primary minimum epochs when the dimmer Algol B eclipses the brighter Algol A. Therefore, we reject all 14 secondary minima, because they occur $P_{\mathrm{orb}}/2$ after the primary minima. We analyze only the remaining $n = 2224$ primary minima between 1782 November 12 and 2018 October 18. These data are given in Table A4 ($\Delta T = 86171^{\mathrm{d}} = 236^{\mathrm{y}}$). We obtain the computed (C) epoch values from the TIDAK database ephemeris:

$$\mathrm{HJD}\ 2445641.5135 + 2.86730431E. \tag{1}$$

This ephemeris predicts that all Algol's primary eclipses occur at multiples HJD $2445641.5135 + E \times P_{\mathrm{orb}}$, where $P_{\mathrm{orb}} = 2^{\mathrm{d}}.86730431$ is the orbital period of Algol and E is an integer number. This constant orbital period ephemeris "model" is quite accurate, because all $O - C$ values are between $-0^{\mathrm{d}}.24$ and $+0^{\mathrm{d}}.15$ during 236 yr.

Out of all 2224 estimates, only 197 have an error estimate. For example, none of the 1226 first older estimates has anerror estimate. However, this does not mean that these values without error estimates are unreliable or inconsistent. The error estimates are available for only about 10% of data. These are all new observations after the year 1921. The range of these known errors is between $0^{\mathrm{d}}.0002$ and $0^{\mathrm{d}}.013$. The most accurate

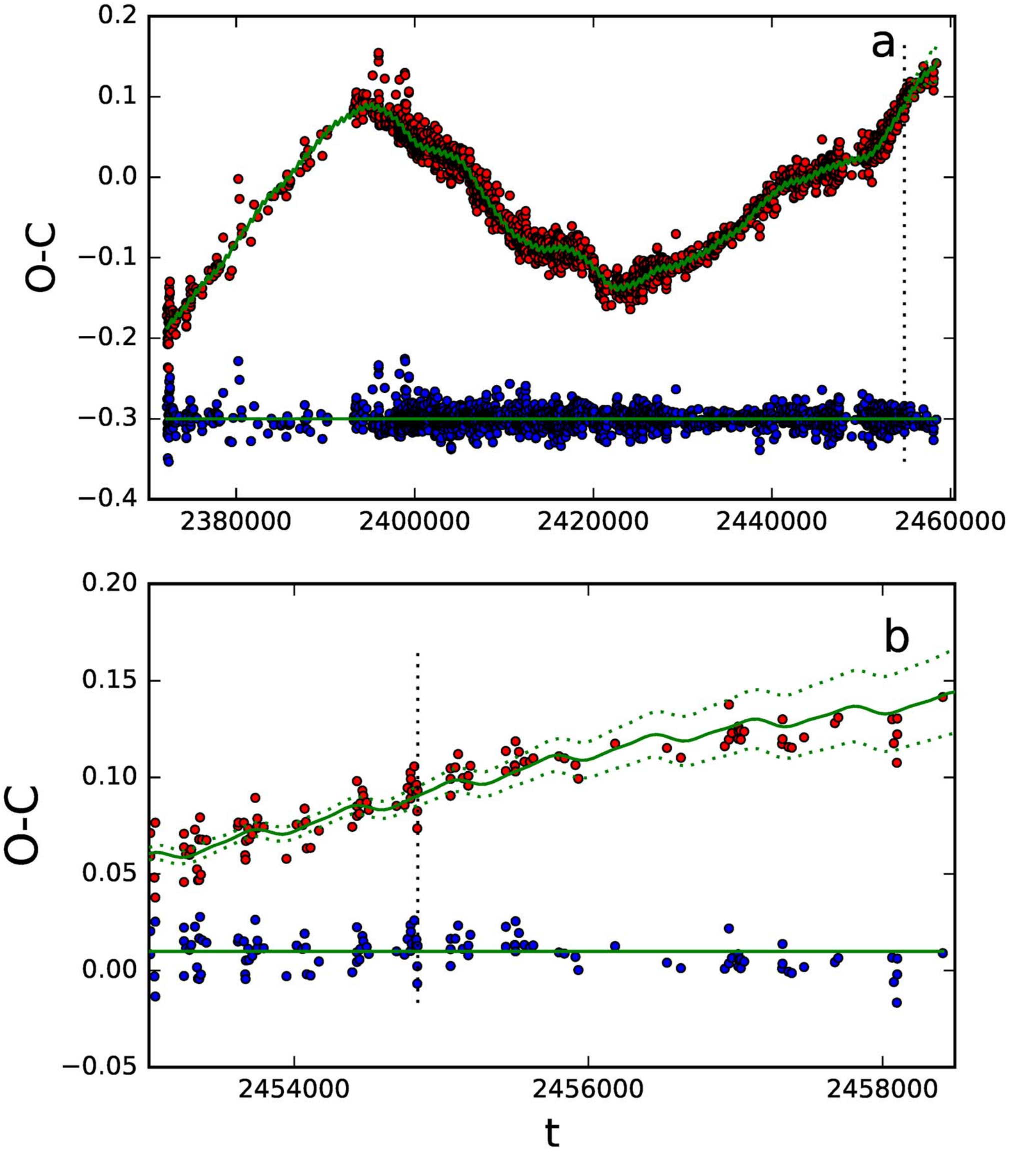

Figure 2. First 226$^\text{y}$ data eccentric orbit analysis (Section 5.2). (a) Model $\mathcal{M} = 3 + 6$ (Table A10). Otherwise as in Figure 1(a). (b) Prediction for Last 9$^\text{y}$ data. Otherwise as in Figure 1(b).

TIDAK database $O - C$ values have four decimals. Because the errors are not known for over 90% of observations, we use arbitrary errors $\sigma_i = 0\overset{\text{d}}{.}00010$ for all $O - C$ values. These arbitrary numerical values do not influence our results, because we use the same weight $w_i = \sigma_i^{-2}$ for every observation, and we compute the DCM test statistic z from the sum of squared residuals (Equation (8)). We will also show that a weighted DCM search, where the $O - C$ data accuracy improves toward modern times, does not alter our results (Section 5.4).

We also analyze shorter subsamples of all data (Table A5). In Section 5.2, we apply DCM to the first 226.2 yr of all data (First 226$^\text{y}$ data). This gives us a prediction for the last 9.2 yr of all data (Last 9$^\text{y}$ data). In Section 5.2, the same DCM procedures are also applied to the first 185.5 yr of all data (First 185$^\text{y}$ data), and the last 50 yr of all data (Last 50$^\text{y}$ data).

3. DCM Method

The DCM notations for the data are $y_i = y(t_i) \pm \sigma_i$, where t_i are the observing times and σ_i are the errors ($i = 1, 2, \ldots, n$). The time span of the data is $\Delta T = t_n - t_1$. The midpoint of data is $t_{\text{mid}} = t_1 + \Delta T/2$.

We analyze these data with DCM, which can detect many signals superimposed on arbitrary trends. Detailed instructions for using the DCM python code were given in the appendix of Paper I. In this current study, we provide all necessary information for reproducing our DCM analysis of Algol data.[1] DCM model is

$$g(t) = g(t, K_1, K_2, K_3) = h(t) + p(t). \tag{2}$$

It is a sum of periodic and aperiodic functions

$$h(t) = h(t, K_1, K_2) = \sum_{i=1}^{K_1} h_i(t) \tag{3}$$

$$h_i(t) = \sum_{j=1}^{K_2} B_{i,j} \cos(2\pi j f_i t) + C_{i,j} \sin(2\pi j f_i t) \tag{4}$$

---

[1] All necessary files for reproducing our results are published in the Zenodo database: doi 10.5281/zenodo.5082125.

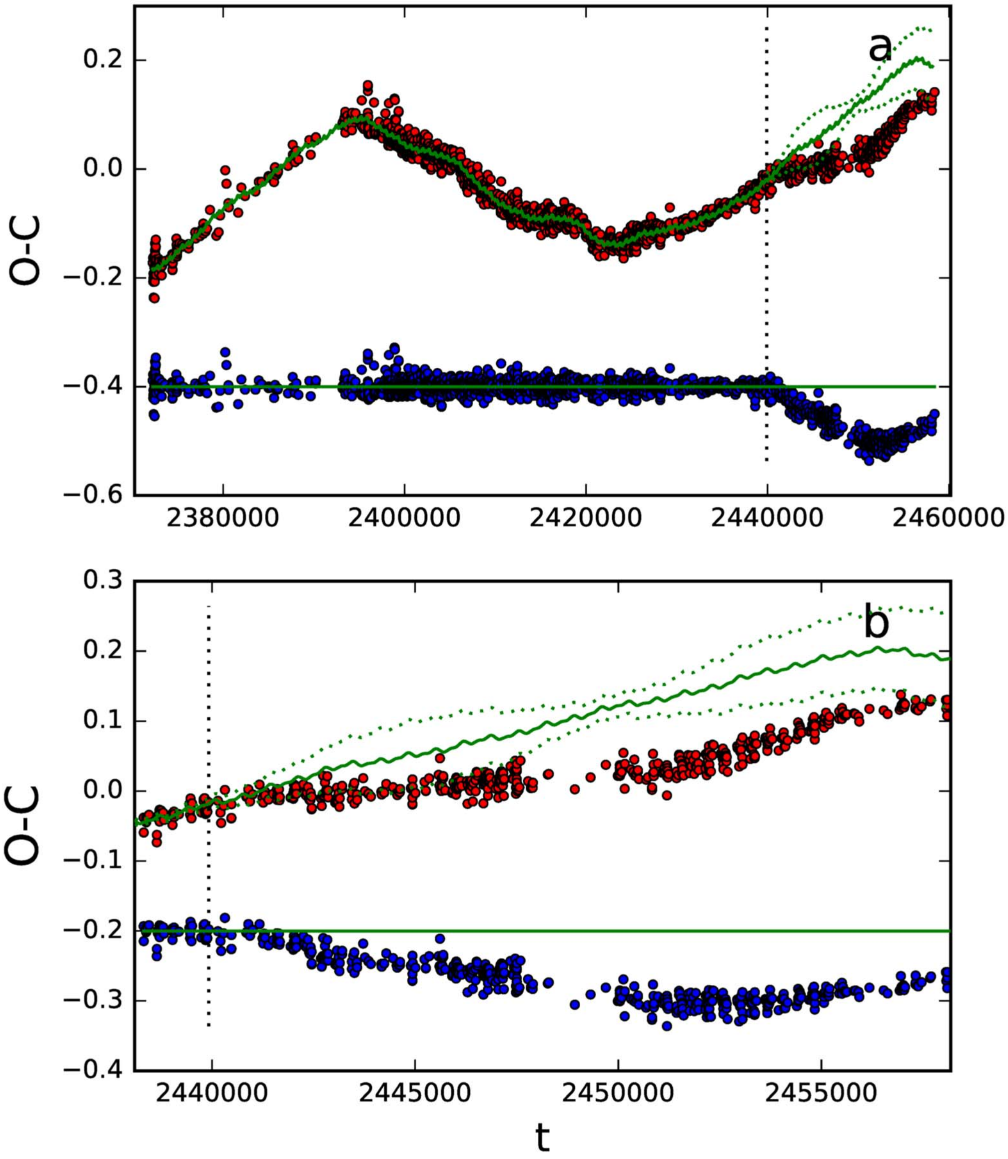

Figure 3. First 185^y data eccentric orbit analysis (Section 5.3). (a) Model $\mathcal{M} = 4 + 6$ (Table A11). Otherwise as in Figure 1(a). (b) Prediction for Last 50^y data. Otherwise as in Figure 1(b).

$$p(t) = p(t, K_3) = \sum_{k=0}^{K_3} p_k(t) \tag{5}$$

$$p_k(t) = M_k\left[\frac{2(t - t_{\rm mid})}{\Delta T}\right]^k. \tag{6}$$

The periodic $h(t)$ function is a sum of K_1 harmonic $h_i(t)$ signals having frequencies f_i. The signal order is K_2. These signals are superimposed on the aperiodic K_3-order polynomial trend $p(t)$.

In the original DCM version, the $p(t)$ terms were $M_k[(2t)/\Delta T]^k$ (Paper I: Equation (5)) and the first time point t_1 was subtracted from all time points t_i before modeling. For odd and even k values, every $M_k[(2t)/\Delta T]^k$ term could only increase or decrease monotonically during the whole ΔT interval, because the argument $(2t)/\Delta T$ was always positive. In our new formulation (Equation (6)), the even $k = 2, 4, \ldots$ terms $M_k[2(t - t_{\rm mid})/\Delta T]^k$ can now both increase and decrease during the whole ΔT interval. This increases the flexibility of the model. Furthermore, it is no longer necessary to subtract the first observing time t_1 before the modeling. Note that the $2(t - t_{\rm mid})/\Delta T$ argument equals -1 at t_1, and $+1$ at t_n. Hence, the scale of polynomial M_k coefficients (Equation (6)) is comparable to the scale of trigonometric $B_{i,j}$ and $C_{i,j}$ coefficients (Equation (4)). This change of $p(t)$ trend terms from $p_k(t) = M_k[(2t)/\Delta T]^k$ to $p_k(t) = M_k[2(t - t_{\rm mid})/\Delta T]^k$ does not change the detected signal periods in any of the analyzed $O - C$ samples.

Our abbreviation "model$_{K_1,K_2,K_3}$" refers to a $g(t)$ model having orders K_1, K_2, and K_3. The free parameters are $\bar{\beta} = [\beta_1, \beta_2, ..., \beta_\eta] = [B_{1,1}, C_{1,1}, f_1, ..., B_{K_1,K_2}, C_{K_1,K_2}, f_{K_1}, M_0, ..., M_{K_3}]$, where $\eta = K_1 \times (2K_2 + 1) + K_3 + 1$ is the number of free parameters. We divide the free parameters $\bar{\beta}$ into two groups, $\bar{\beta}_I$ and $\bar{\beta}_{II}$. The first group of free parameters are the frequencies $\bar{\beta}_I = [f_1, ..., f_{K_1}]$. These frequencies make the $g(t)$ model nonlinear, because all free parameters are not eliminated from all partial derivatives $\partial g/\partial \beta_i$. If the $\bar{\beta}_I$ frequencies are fixed to constant known tested numerical values, the model becomes linear, because all partial derivatives $\partial g/\partial \beta_i$ no longer contain any free parameters. In this case, the solution for the remaining

Table 1
Third-body Circular Orbits (Section 5.5)

	Periods		Amplitudes		$m_3^{i=90}$	$a_3^{i=90}$	$m_3^{i=60}$	$a_3^{i=60}$	$m_3^{i=30}$	$a_3^{i=30}$	
	(days)	(yr)	(days)	($m_\odot$)	(au)	($m_\odot$)	(au)	($m_\odot$)	(au)	Name	
$\boldsymbol{p}_6$	79,999 ± 1216	219.0 ± 3.3	$\boldsymbol{A}_6$	0.287 ± 0.005	2.50 ± 0.02	44.7 ± 0.4	3.03 ± 0.03	42.6 ± 0.3	6.94 ± 0.08	32.2 ± 0.2	Algol H
$\boldsymbol{p}_5$	24,246 ± 872	66.4 ± 2.4	$\boldsymbol{A}_5$	0.018 ± 0.002	0.27 ± 0.02	26.1 ± 0.5	0.31 ± 0.02	25.9 ± 0.5	0.56 ± 0.04	25.0 ± 0.5	Algol G
$\boldsymbol{p}_4$	12,294 ± 109	33.7 ± 0.3	$\boldsymbol{A}_4$	0.018 ± 0.001	0.43 ± 0.03	16.19 ± 0.04	0.50 ± 0.04	16.06 ± 0.01	0.91 ± 0.07	15.2 ± 0.05	Algol F
$\boldsymbol{p}_3$	10,145 ± 30	27.78 ± 0.08	$\boldsymbol{A}_3$	0.0097 ± 0.0004	0.26 ± 0.01	14.596 ± 0.002	0.30 ± 0.01	14.50 ± 0.01	0.54 ± 0.02	14.053 ± 0.005	Algol E
$\boldsymbol{p}_2$	7290 ± 29	19.96 ± 0.08	$\boldsymbol{A}_2$	0.007 ± 0.001	0.24 ± 0.03	11.72 ± 0.07	0.28 ± 0.04	11.67 ± 0.08	0.49 ± 0.07	11.34 ± 0.12	Algol D
$\boldsymbol{p}_1$	680.4 ± 0.4	1.863 ± 0.001	$\boldsymbol{A}_1$	0.0064 ± 0.0007	1.2 ± 0.1	2.14 ± 0.04	1.4 ± 0.2	2.09 ± 0.04	2.8 ± 0.4	1.82 ± 0.07	Algol C

Note. Periods ($\boldsymbol{p}_1$, ...$\boldsymbol{p}_6$) and amplitudes ($\boldsymbol{A}_1$, ..., $\boldsymbol{A}_6$) used to compute the third mass m_3 and semimajor axis a_3 estimates (Equations (18) and (19)). Inclination alternatives are $i = 90°$, $60°$, and $30°$. The last column gives our tentative object names. We emphasize that our approximate m_3 and a_3 estimates are based on four assumptions. (1) All six signals are caused by the LTTE of wide-orbit candidates. (2) Correct hierarchical system alternative is Configuration 1 (Figure A15). (3) All orbits are circular. (4) Every candidate can be treated as a "third body." In other words, the effects of other candidates inside the "third-body" orbit can be ignored in Equations (18) and (19).

second group of free parameters, $\bar{\beta}_{II} = [B_{1,1}C_{1,1},\ ...,\ B_{K_1,K_2},\ C_{K_1,K_2},\ M_0,\ ...,\ M_{K_3}]$, is unambiguous. We refer to this type of model and their free parameter solutions when we use the concepts "linear model" and "unambiguous result."

The DCM model residuals are

$$\epsilon_i = y(t_i) - g(t_i) = y_i - g_i. \tag{7}$$

For every combination $\bar{\beta}_I = [f_1, f_2,\ ...,\ f_{K_1}]$ of tested frequencies, we compute the DCM test statistic

$$z = z(f_1, f_2,\ ...,\ f_{K_1}) = \sqrt{R/n} \tag{8}$$

from the sum of squared residuals $R = \sum_{i=1}^{n} \epsilon_i^2$ of a nonweighted linear model least-squares fit. We use this nonweighted test statistic, because the errors for the data are unknown.

The global periodogram minimum is at

$$z_{\rm min} = z(f_{1,\rm best}, f_{2,\rm best}, \ldots, f_{K_1,\rm best}), \tag{9}$$

where $f_{1,\rm best}, f_{2,\rm best}, \ldots, f_{K_1,\rm best}$ are the frequencies of the best DCM model for the data. Every scalar value of this z periodogram is computed from K_1 frequency values. For example, the $K_1 = 2$ periodogram could be plotted like a map, where f_1 and f_2 are the coordinates, and $z = z(f_1, f_2)$ represents the height. However, a graphical presentation for $K_1 \geqslant 3$ is impossible, because it requires more than three dimensions. In Paper I, we solved this problem by presenting only the following one-dimensional slices of the full periodograms:

$$\begin{aligned}
z_1(f_1) &= z(f_1, f_{2,\rm best},\ ...,\ f_{K_1,\rm best})\\
z_2(f_2) &= z(f_{1,\rm best}, f_2, f_{3,\rm best},\ ...,\ f_{K_1,\rm best})\\
z_3(f_3) &= z(f_{1,\rm best}, f_{2,\rm best}, f_3, f_{4,\rm best}, \ldots, f_{K_1,\rm best})\\
z_4(f_4) &= z(f_{1,\rm best}, f_{2,\rm best}, f_{3,\rm best}, f_4, f_{5,\rm best}, f_{K_1,\rm best})\\
z_5(f_5) &= z(f_{1,\rm best}, f_{2,\rm best}, f_{3,\rm best}, f_{4,\rm best}, f_5, f_{K_1,\rm best})\\
z_6(f_6) &= z(f_{1,\rm best}, f_{2,\rm best}, f_{3,\rm best}, f_{4,\rm best}, f_{5,\rm best}, f_6).
\end{aligned} \tag{10}$$

In the above $K_1 = 2$ map analogy, $z_1(f_1)$ would represent the height at the f_1 coordinate when moving along the constant line $f_2 = f_{2,\rm best}$ that crosses the global minimum $z_{\rm min}$.

DCM determines the following $h_i(t)$ signal parameters:

$$\begin{aligned}
P_i &= 1/f_i = \text{Period}\\
A_i &= \text{Peak to peak amplitude}\\
t_{\rm i,min,1} &= \text{Deeper primary minimum epoch}\\
t_{\rm i,min,2} &= \text{Secondary minimum epoch (if present)}\\
t_{\rm i,max,1} &= \text{Higher primary maximum epoch}\\
t_{\rm i,max,2} &= \text{Secondary maximum epoch (if present)},
\end{aligned}$$

and the M_k parameters of the $p(t)$ trend. For us, the most interesting parameters are the signal periods P_i and the signal amplitudes A_i, and the $p(t)$ trend coefficient M_1.

We determine the DCM model parameter errors with the bootstrap procedure (Efron & Tibshirani 1986, 1994). During each bootstrap round, we select a random sample $\bar{\epsilon}^*$ from the residuals $\bar{\epsilon}$ of the DCM model (Equation (7)). Each ϵ_i can be chosen as many times as the random selection happens to favor it. This gives the artificial bootstrap data sample

$$y_i^* = g_i + \epsilon_i^*.$$

The DCM model for each $\bar{y}^*$ sample gives one estimate for every model parameter. For each particular model parameter, its error estimate is the standard deviation of all estimates obtained from all $\bar{y}^*$ bootstrap samples. We have already used this same bootstrap procedure in our TSPA and CPS methods (Jetsu & Pelt 1999; Lehtinen et al. 2011). Finally, we note that our bootstrap procedure cannot assess the bias in the y_i input data, which first contaminates the ϵ_i values and then also the $\epsilon_i^\star$ and $y_i^\star$ values.

We use the Fisher test to compare any pair $g_1(t)$ and $g_2(t)$ of simple and complex models. Their number of free parameters ($\eta_1 < \eta_2$) and their sums of squared residuals (R_1, R_2) give the test statistic

$$F_R = \left(\frac{R_1}{R_2} - 1\right)\left(\frac{n - \eta_2 - 1}{\eta_2 - \eta_1}\right). \tag{11}$$

Our null hypothesis is

H_0: "*The complex model $g_2(t)$ does not provide a significantly better fit to the data than the simple model $g_1(t)$.*"

Under H_0, the test statistic F_R has an F distribution with (ν_1, ν_2) degrees of freedom, where $\nu_1 = \eta_2 - \eta_1$ and $\nu_2 = n - \eta_2$ (Draper & Smith 1998). The probability for F_R reaching values higher than F is called the critical level $Q_F = P(F_R \geqslant F)$. We reject the H_0 hypothesis if

$$Q_F < \gamma_F = 0.001, \tag{12}$$

where γ_F is the preassigned significance level. It represents the probability of falsely rejecting H_0 when it is in fact true. The H_0 rejection means that we rate the complex $g_2(t)$ model better than the simple $g_1(t)$ model.

The Q_F critical level becomes smaller when F_R increases. In other words, the H_0 hypothesis rejection probability increases for larger F_R values. The basic idea of the Fisher test is simple. The sum of complex model residuals R_2 decreases when the η_2 number of free parameters increases. When the complex model has more η_2 free parameters, the first $(R_1/R_2 - 1)$ term increases F_R (Equation (11)), but at the same time, the second $(n - \eta_2 - 1)/(\eta_2 - \eta_1)$ penalty term decreases F_R. In conclusion, this second penalty term prevents overfitting.

The key ideas of DCM are

1. The nonlinear DCM model $g(t)$ of Equation (2) becomes linear when the frequencies $f_1,\ ...,\ f_{K_1}$ are fixed to their tested numerical values. These linear models give unambiguous results.
2. DCM tests a dense grid of all possible frequency combinations $f_1 > f_2 > ... > f_{K_1}$. For every frequency combination, the linear model least-squares fit gives the test statistic
$$\begin{aligned}
z &= \sqrt{\chi^2/n}\ \text{if errors } \sigma_i \text{ are known}\\
z &= \sqrt{R/n}\ \text{if errors } \sigma_i \text{ are unknown},
\end{aligned}$$
where $\chi^2 = \sum_i^n \epsilon_i^2/\sigma_i^2$, $R = \sum_i^n \epsilon_i^2$ and $\epsilon_i = y_i - g_i$ are the model residuals.
3. The $f_1 > f_2 > ... > f_{K_1}$ grid combination of the best DCM model minimizes the z-test statistic.
4. The bootstrap method gives the error estimates for all model parameters.

5. All different K_1-, K_2-, and K_3-order nested models are compared using the Fisher test, which reveals the best one of all models (Draper & Smith 1998; Allen 2004).

In short, DCM applies the following robust and well-tested statistical approaches: linear least-squares fits (Idea 1), χ^2- and R-test statistic (Idea 2), dense tested frequency grids (Idea 3), bootstrap utilizing residuals (Idea 4), and Fisher test comparison of nested models (Idea 5).

The caveats of DCM are as follows:

1. DCM is designed for periodicity detection, but it gives no direct significance estimates for these detected periodicities. In this sense, DCM resembles our former TSPA and CPS methods (Jetsu & Pelt 1999; Lehtinen et al. 2011). DCM utilizes indirect Fisher test significance estimates to identify the best model among all tested models, but it gives no significance estimates for the detected periodicities of this best model. We will later discuss our indirect significance estimates, especially in connection with the look-elsewhere effect (Section 6.6).
2. The best frequency combination can be missed if the tested grid is too sparse (Idea 3). However, an adequately dense tested frequency grid eliminates the possibility for this kind of an error. The caveat is that denser grids require more computation time.

   For example, all three-signal z_1, z_2, and z_3 periodograms for the original data are continuous and display no abrupt jumps, because the periodogram values for all close tested frequencies correlate (see Figure A6). Because the frequencies of the minima of all these periodograms are accurately determined, there is no need to test an even denser grid (i.e., more trials), because this would not alter the final result of the nonlinear iteration (Paper I: Equation (18)). In other words, the detected period values would no longer change if we increased the number of of tested frequencies (Paper I: n_L and n_S trials). Because DCM gives no direct significance estimates for the detected periods (Caveat 1), there is no need to determine the number of independent trials, like, for example, the number of independent tested frequencies (e.g., Jetsu & Pelt 2000, their Equation (A.1)).
3. If the grid of each tested $f_1 > f_2 > ... > f_{K_1}$ frequency contains n_f values, the total number of tested frequency combinations is proportional to $\propto n_f^{K_1}$. For example, it took about one month for an ordinary PC to compute the four-signal DCM model$_{4,2,1}$ search, and to analyze its 20 bootstrap samples (Table A7, model $\mathcal{M} = 4$).
4. Some DCM models are unstable because they are simply wrong models for the data. For example, a wrong $p(t)$ trend order K_3, or a search for too many K_1 signals, can cause such instability. In this paper, we denote such unstable models with “Um.” We denote the two signatures of such unstable models with

“Ad” = Dispersing amplitudes = Amplitudes and/or amplitude errors disperse.

“If” = Intersecting frequencies = At least two model frequencies are too close to each other.

Both of the above instabilities were defined in Paper I (Section 4.3), where a typical example of the wildly oscillating signals was also shown in Figure 6 of Paper I.

DCM tests all reasonable alternative linear models for the data and determines the unambiguous results for the best values of their free parameters. This brute numerical approach finds the best model among all alternative models. DCM “works like winning a lottery by buying all lottery tickets” (Paper I).

4. Third-body $O - C$ Changes

The light-time travel effect (LTTE) caused by a third body is

$$(O - C) = \frac{K}{\sqrt{(1 - e^2\cos^2\omega)}} \times \left[\frac{1 - e^2}{1 + e\cos\nu(t)}\sin(\nu(t) + \omega) + e\sin\omega\right] = \frac{a\sin i}{173.15} \times \left[\frac{1 - e^2}{1 + e\cos\nu(t)}\sin(\nu(t) + \omega) + e\sin\omega\right], \tag{13}$$

where

$$K = \frac{a\sin i\sqrt{1 - e^2\cos^2\omega}}{173.15} \tag{14}$$

(Irwin 1952). This relation gives the EB orbit around the common center of mass of all three stars. The orbit parameters are the semimajor axis ($[a] =$ au), the orbital plane inclination ($[i] =$ rad), the eccentricity of orbit (e), the longitude of periastron ($[\omega] =$ rad), the true anomaly ($[\nu] =$ rad), and the amplitude of the light-time travel effect:

$$K = A/2, \tag{15}$$

which is half of the peak to peak amplitude A of the observed $O - C$ changes ($[A] =$ days).

We compute the true anomaly from the Fourier expansion

$$\nu(t) = M(t) + \left(2e - \frac{1}{4}e^3\right)\sin[M(t)] + \frac{5}{4}e^2\sin[2M(t)] + \frac{13}{12}e^3\sin[3M(t)] + O(e^4), \tag{16}$$

where

$$M(t) = \frac{2\pi(t - t_p)}{p}, \tag{17}$$

is the mean anomaly (Mueller 1995; Roy 2005). The other parameters are the EB orbit pericenter epoch ($[t_p] =$ HJD), the third-body orbital period ($[p] =$ days) and the omitted fourth-order terms ($[O(e^4)] =$ rad).

If the orbit is circular ($e = 0$), the third -body mass m_3 can be solved from the mass function

$$f(m_3) = \frac{m_3\sin i^3}{(m_1 + m_2 + m_3)^2} = \frac{[173.15(A/2)]^3}{p^2}, \tag{18}$$

where m_1 and m_2 are the masses of EB (Wolf et al. 1999; Zasche & Wolf 2007; Manzoori 2016; Esmer et al. 2021). The semimajor axis of the third-body orbit is

$$a_3 = a\frac{(m_1 + m_2)}{m_3}, \tag{19}$$

where $a = 173.15(A/2)/\sin i$.

For a circular third-body orbit, the suitable $O - C$ curve DCM model order is $K_2 = 1$, the pure sinusoid (Equation (13): $e = 0$). For an eccentric $e > 0$ third-body orbit, the $O - C$ curve is not a pure sinusoid, and the suitable DCM model order is $K_2 = 2$ (Hoffman et al. 2006).

5. Results

Here, we present separately the DCM period search results for all data (Section 5.1), First 226^{y} data (Section 5.2), and First 185^{y} data (Section 5.3). We also make some additional experiments (Section 5.4).

5.1. All Data

5.1.1. All Data: Trend

In Table A6, the Fisher test is used to compare the results for all data in 12 separate DCM period searches between $P_{\min} = 6000^{\mathrm{d}}$ and $P_{\max} = 80000^{\mathrm{d}}$. These models have one, two, or three signals ($K_1 = 1$, 2, or 3). The third-body orbits can be eccentric ($K_2 = 2 \equiv e > 0$). The alternative tested $p(t)$ trends are $K_3 = 0$, 1, 2, or 3. Table A6 contains many "–" because it makes no sense to compare the same pair of models twice, nor to compare the model to itself. The total number of compared pairs is $(12 \times 11)/2$. For example, the Fisher test comparison of the one-signal $\mathcal{M} = 1$ and $\mathcal{M} = 2$ models gives a large test statistic value $F = 2821$. The critical level Q_F of this F value falls below the computational[2] accuracy of 10^{-16} (Table A6: $Q_F < 10^{-16}$). This means that the linear $K_3 = 1$ trend model$_{1,2,1}$ is absolutely certainly a better model than the constant $K_3 = 0$ trend model$_{1,2,0}$. The upward arrow "$\uparrow$" indicates this result. Note that Table A6 contains numerous "$Q_F < 10^{-16}$" cases, where the identification of the better model is absolutely certain.

All column $\mathcal{M} = 10$ arrows point upwards ($\uparrow$), and all line $\mathcal{M} = 10$ arrows point leftwards ($\leftarrow$) in Table A6. Hence, this stable $\mathcal{M} = 10$ model is better than all other 11 alternative models. This best DCM model$_{3,2,1}$ for all data is a sum of $K_1 = 3$ signals having an order $K_2 = 2$ and a linear $K_3 = 1$ trend. We use this $K_3 = 1$ linear trend in all analysis of original data. The meaning of this linear trend is discussed later (Section 6.4, Equation (27)). We will also show that all data contain only three $K_2 = 2$ order signals between 8000 and 80,000 days (Section 5.1.2).

Four of the 12 models are unstable "Um" (Table A6: $\mathcal{M} = 3$, 5, 8, and 9). There are three models where the detected period exceeds ΔT time span of data (Table A6: $\mathcal{M} = 2$, 3, and 7). They are denoted with the symbol "Lp" = Leaking period = At least one detected period exceeds ΔT time span of data.

5.1.2. All Data: Eccentric Orbits

In Table A6, we compared $(12 \times 11)/2$ pairs of models against each other. The better model in each pair was identified with the Fisher test: the complex model above "$\uparrow$," or the simple model on the left "$\leftarrow$."

The structure of our Table A7 is more complicated, because we squeeze all DCM eccentric orbit search results for all data into this single table. We search for periods between 8000 and 80,000 days. The left side of this table gives the detected periods and amplitudes. The right side gives the Fisher test comparison results. For example, the one-signal $\mathcal{M} = 1$ model period and amplitude are $P_1 = 88183^{\mathrm{d}} \pm 816^{\mathrm{d}}$ and $A_1 = 0\overset{\mathrm{d}}{.}313 \pm 0\overset{\mathrm{d}}{.}004$. The next six "–" notations for this $\mathcal{M} = 1$ model mean that it has no other periods P_2, P_3, or P_4, nor amplitudes A_2, A_3 or A_4. A Fisher test comparison between this one-signal model$_{1,2,1}$ ($\mathcal{M} = 1$) and the two-signal model$_{2,2,1}$ ($\mathcal{M} = 2$) gives an extreme test statistic value $F = 183$. The critical level $Q_F < 10^{-16}$ confirms that $\mathcal{M} = 2$ model is certainly the better one in this pair of models. A comparison of the $\mathcal{M} = 1$ model to the $\mathcal{M} = 3$ and $\mathcal{M} = 4$ models gives the same result.

For the next $\mathcal{M} = 2$, 3, and 4 models, the number of detected periods and amplitudes increases one by one. The number of Fisher tests decreases one by one, because it is unnecessary to test the same pair of models twice ("–"), nor to compare any model to itself ("–").

The periods and amplitudes for the one-, two-, and three-signal models are consistent (Table A7: $\mathcal{M} = 1$–3). When we detect a new signal, we redetect the same old earlier signal periods and amplitudes for models having less signals. The one-signal $\mathcal{M} = 1$ model shows a leaking period "Lp," because the $P_1 = 88183^{\mathrm{d}}$ period exceeds the $\Delta T = 86171^{\mathrm{d}}$ time span of data. The two- and the three-signal $\mathcal{M} = 2$ and $\mathcal{M} = 3$ models are stable, but the $\mathcal{M} = 4$ model is not ("Um").

The one-dimensional $z_1(f_1)$, $z_2(f_2)$, $z_3(f_3)$, and $z_4(f_4)$ periodogram slices (Equation (10)) of the $\mathcal{M} = 4$ model are shown in Figure A4. The transparent diamonds denote the locations of the red $z_1(f_1)$, the blue $z_2(f_2)$, the green $z_3(f_3)$, and the yellow $z_4(f_4)$ periodogram minima. These minima are clearly separated.

The four-signal $\mathcal{M} = 4$ model is unstable because it suffers from the amplitude dispersion "Ad" effect. The periodograms of this model do not betray this effect (Figure A4), but the exceedingly high-amplitude green $h_3(t)$ and yellow $h_4(t)$ signals do (Figure A5). The errors of both A_3 and A_4 amplitudes are large. The $P_4 = 55172^{\mathrm{d}}$ period is about two times longer than the $P_3 = 26846^{\mathrm{d}}$ period. DCM exploits the antiphase sum of these two dispersing high-amplitude signals for modeling all data.

The stable three-signal $\mathcal{M} = 3$ model is a better model for all data than the failing unstable "Um" four-signal $\mathcal{M} = 4$ model. The Fisher test reveals with an absolute certainty of $Q_F < 10^{-16}$ that this three-signal $\mathcal{M} = 3$ model is also better than the $\mathcal{M} = 1$ model or the $\mathcal{M} = 2$ model (Table A7: two times "$\uparrow$" in Col. 8).

Model $\mathcal{M} = 3$ periodogram minima are also clearly separated (Figure A6, lower panel). When all three periodograms are plotted in the same scale, the two $z_1(f_1)$ and $z_2(f_2)$ periodogram minima appear to be shallower than the $z_3(f_3)$ periodogram minimum, because the high-amplitude $h_3(t)$ signal dominates in this three-signal $\mathcal{M} = 3$ model (Figure A6, upper panel). This 79999^{d} period $h_3(t)$ signal has a much bigger impact on the sum of squared residuals R than the two lower-amplitude 20358^{d} period $h_1(t)$ and 24742^{d} period $h_2(t)$ signals. This three-signal $\mathcal{M} = 3$ model is shown in Figure A7. The level of residuals, denoted by blue dots, is stable and there are no trends. Each $h_j(t_i)$ signal

$$y_{i,j} = y_i - [g(t_i) - h_j(t_i)] \tag{20}$$

is also shown separately (Figure A8). The red $h_1(t)$ and the blue $h_2(t)$ curves show two minima and two maxima, but the green

---

[2] This is the computational Q_F estimate accuracy for the f.cdf subroutine in the scipy.optimize Python library.

large-amplitude $h_3(t)$ curve shows only one minimum and one maximum.

It takes about one month for an ordinary PC to compute the results for the four-signal $\mathcal{M}=4$ model, as well as to analyze at 20 twenty bootstrap samples (Table A7: $\text{model}_{4,2,1}$). The computation of a five-signal model would take several months. Fortunately, there is no fourth or fifth signal between 8000 and 80,000 days in all data, because the $\mathcal{M}=4$ model is unstable ("Um"). The three-signal $\mathcal{M}=3$ model is the best model for all data. Therefore, we can search for additional periods shorter than 8000 days from the $\mathcal{M}=3$ model residuals.

Because the $\mathcal{M}=3$ model residuals contain no trends, we analyze them by using $K_3=0$ models having a constant $p(t)$ level. The period search between 500^{d} and 8000^{d} gives two new periods, $680\overset{\mathrm{d}}{.}4$ and 7290^{d} (Table A7, model $\mathcal{M}=6$). In the three-signal $\mathcal{M}=7$ model, the periods $P_2=7124^{\mathrm{d}}$ and $P_3=7698^{\mathrm{d}}$ give $[P_2^{-1}-P_3^{-1}]^{-1} = 95541^{\mathrm{d}} \pm 13902^{\mathrm{d}}$, which is equal to the time span $\Delta T=86171^{\mathrm{d}}$ of all data (Table A7: $\mathcal{M}=7$). In other words, the difference between the real $P_2=7124^{\mathrm{d}}$ and the spurious $P_3=7698^{\mathrm{d}}$ period is one round during ΔT. Our symbol for this type of spurious periods is "Sp" = Spurious period = unreal periods caused by the data time span and real periodicity.

Therefore, we reject the $\mathcal{M}=7$ model, and the best model for residuals is the $\mathcal{M}=6$ model. In this analysis of residuals, DCM again consistently redetects the same periods and amplitudes of earlier models having fewer signals. The model $\mathcal{M}=6$ periodograms, and the model itself, are shown in Figures A9 and A10. The last two $680\overset{\mathrm{d}}{.}4$ and 7290^{d} signals detected from the residuals are shown in Figure A11. As expected of a real $O-C$ signal, both curves have only one minimum and one maximum. These two signals are 44.8 and 41.0 times weaker than the strongest first-detected 79999^{d} signal.

For the original data, DCM detects simultaneously the three signals and the trend of the $\mathcal{M}=3$ model. For the residuals, the same applies to the two signals and the trend of the $\mathcal{M}=6$ model. In this sense, DCM differs from the "prewhitening" technique, which requires that the trend must be determined and removed before even one signal at the time can be detected (e.g., Reinhold et al. 2013). This "'prewhitening" technique, which applies the discrete Fourier transform (DFT), was compared to DCM in Paper I (Section 6).

We conclude that DCM detects five signals from all data ($n=2224$). The full model for all Algol's $O-C$ data is the sum of the $\mathcal{M}=3$ model for the original data and the $\mathcal{M}=6$ model for the residuals (Table A7). Our notation for this sum

$$\text{model}_{3,2,1} + \text{model}_{2,2,0}$$

of two models in Table A7 is simply the "$\mathcal{M}=3+6$ model." This model is denoted by the green continuous line in Figures 1(a) and (b). Its standard deviation of residuals is $0\overset{\mathrm{d}}{.}011$. We also give a 10 yr prediction for Algol's $O-C$ changes after our last observation on 2018 October 18 (Figure 1(b)).

5.1.3. All Data: Circular Orbits

In our Appendix, we show that if an eccentric orbit $O-C$ curve has a period p, then this curve is a sum of two circular orbit $O-C$ curves having periods p and $p/2$. For this reason, the DCM period search results obtained for circular orbits in this section can be used to check the eccentric orbit results presented earlier in Section 5.1.2, and vice versa (Table A13).

For a third-body circular orbit, the correct DCM model $h_i(t)$ signal order is $K_2=1$ (Equation (13): $e=0$). We fix the $p(t)$ trend to $K_3=1$ and search for the correct K_1 number of circular orbit sinusoidal signals in all data. Two alternative approaches are tested. We will show that both approaches give the same results.

In the first alternative approach, we search for one, two, three, and four sinusoidal circular orbit signals having periods between 8000 and 80,000 days in all data (Table A8). The one-signal $\mathcal{M}=1$ model is stable. The two-, three-, and four-signal $\mathcal{M}=2$, $\mathcal{M}=3$, and $\mathcal{M}=4$ models are unstable ("Um") because they all suffer from dispersing amplitudes "Ad." The largest periods ("Lp") in these three models exceed the all data time span $\Delta T=86171^{\mathrm{d}}$.

From the $\mathcal{M}=4$ model residuals, we detect the fifth sinusoidal signal period 10175^{d} (Table A8: $\mathcal{M}=5$). The next $\mathcal{M}=6$ model is unstable ("Um"), and it is also rejected with the Fisher test criterion (Equation (12)).

DCM detects signatures of five sinusoidal signals having periods longer than 8000 days. Therefore, we search for shorter periods from the $\mathcal{M}=5$ model residuals. This reveals three additional sinusoidal $\mathcal{M}=9$ model signals (Table A8). The next four-signal model $\mathcal{M}=10$ is rejected with the Fisher test criterion (Equation (12)).

In our first alternative approach, the best circular orbit model is the $\mathcal{M}=4+5+9$ model (Table A8).

Our typical number of tested periods is $n_{\mathrm{L}}=80$ in the long search and $n_{\mathrm{S}}=40$ in the short search. We use these dense grids to eliminate the "trial factor" error (Section 3: Caveat 2). Computation time is proportional to $\propto n_{\mathrm{L}}^{K_1}$ and $\propto n_{\mathrm{S}}^{K_1}$. For a larger number of signals, our dense tested grids take a long time to compute. For example, the computation of the four-signal model for all data, and its 20 bootstrap samples, takes about one month for an ordinary PC.

In the second alternative approach we also search for circular orbit periods between 8000 and 80,000 days. However, we reduce the computation time dramatically by testing only $n_{\mathrm{L}}=30$ and $n_{\mathrm{S}}=8$ frequencies. In this case, an ordinary PC can perform the six-signal DCM search in about one week. Unlike in the first alternative approach, we do not need to search for the fifth and sixth signals from the four-signal model residuals. We can perform the five- and the six-signal DCM search directly in all original data. The four-, five-, and six-signal circular orbit model results for all original data are given in Table A9. All $\mathcal{M}=1$, 2, and 3 models suffer from amplitude dispersion "Ad," as well as from leaking periods "Lp," because their largest detected periods exceed ΔT. Model $\mathcal{M}=3$ also suffers from intersecting frequencies ("If"). We reject it with the Fisher test criterion (Equation (12)). The best circular orbit model for all original data is the five-sinusoidal-signal $\mathcal{M}=2$ model. The $\mathcal{M}=2$ model periodogram is shown in Figure A12. The periodogram minimum of the largest $P_5=120740^{\mathrm{d}}$ period is real, because the violet $z_5(f_5)$ curve in the lower panel turns upwards at smaller tested frequencies (i.e., periods larger than ΔT). The $\mathcal{M}=2$ model itself is shown in Figure A13.

From model $\mathcal{M}=2$ residuals, we find two periods shorter than 8000 days (Table A9: $\mathcal{M}=5$). We reject model $\mathcal{M}=6$, because the periods $P_1=7034^{\mathrm{d}} \pm 148^{\mathrm{d}}$ and $P_2=7478^{\mathrm{d}} \pm 82^{\mathrm{d}}$ give $(P_1^{-1}-P_2^{-1})^{-1} = 118469^{\mathrm{d}} \pm 46755^{\mathrm{d}}$. Hence, the spurious

"Sp" period P_1 is connected to the real period P_2 and the time span $\Delta T = 86171^{\rm d}$ of all data.

The second alternative approach best circular orbit model is the $\mathcal{M} = 2 + 5$ model (Table A9).

We compare the results of our two alternative approach circular orbit DCM analyses in Table A12. All results are consistent. The periods and amplitudes agree within their error limits. We detect the same five longer sinusoidal signal periods from the original data and the same two shorter period sinusoids from the residuals. We get these consistent results even after dramatically reducing the number of tested frequencies. Hence, these two analyses do not suffer from the "trial factor" effect (Section 3: Caveat 2). The dispersing amplitudes "Ad" or the leaking periods "Lp" do not mislead this analysis either.

5.2. First $226^{\rm y}$ Data

The eccentric orbit DCM search results for the subsample First $226^{\rm y}$ data are given in Table A10. The one-signal $\mathcal{M} = 1$ model and two-signal $\mathcal{M} = 2$ model suffer from leaking periods ("Lp"). The stable three-signal $\mathcal{M} = 3$ model is the best one for the original data, because the four-signal $\mathcal{M} = 4$ model is unstable ("Um").

For the $\mathcal{M} = 3$ model residuals, the best model is the $\mathcal{M} = 6$ model. We reject model $\mathcal{M} = 7$, because the relation $[P_2^{-1} - P_3^{-1}]^{-1} = 81963^{\rm d} \pm 13594^{\rm d}$ reveals that the third $P_3 = 7757^{\rm d}$ period is a spurious "Sp" period connected to the real period $P_2 = 7078^{\rm d}$ and the time span $\Delta T = 82602^{\rm d}$ of data.

The best model for First $226^{\rm y}$ data is the $\mathcal{M} = 3 + 6$ model (Table A10). This model is shown in Figure 2. It gives an excellent prediction for the next 9 yr of the Last $9^{\rm y}$ data (Figure 2(b)). The standard deviation of prediction residuals is only $0\overset{\rm d}{.}0078$ ($n = 50$). It is smaller than the standard deviation $0\overset{\rm d}{.}011$ of the predictive $\mathcal{M} = 3 + 6$ model residuals ($n = 2174$). However, the larger errors of the older observations can explain this contradiction. The main conclusion is that our 9 yr prediction succeeds.

5.3. First $185^{\rm y}$ Data

The eccentric orbit DCM search results for the shortest subsample First $185^{\rm y}$ data are given in Table A11. The one-signal $\mathcal{M} = 1$ model is stable. The two- and three-signal $\mathcal{M} = 2$ and $\mathcal{M} = 3$ models are unstable (Table A11: "Um"). The best model for First $185^{\rm y}$ data is the stable four-signal $\mathcal{M} = 4$ model.

For the $\mathcal{M} = 4$ model residuals, the stable $\mathcal{M} = 6$ model is the best one, because the $\mathcal{M} = 7$ model is unstable ("Um")

The best $\mathcal{M} = 4 + 6$ model for the First $185^{\rm y}$ data is shown in Figure 3. Our 50 yr prediction succeeds only for the first few years (Figure 3(b)). However, this is no surprise, because the time span of predictive data is only $\Delta T = 67680^{\rm d} = 185^{\rm y}$. For this reason, the longest and the strongest detected predictive signal period is $P_4 = 62992^{\rm d} = 172^{\rm y}$ (Table A11: $\mathcal{M} = 4$). This high-amplitude signal determines the long-term prediction trend for the Last $50^{\rm y}$ data. We have already shown that the correct period for this long-term trend would be $219^{\rm y}$ (Table A7: $\mathcal{M} = 3$, Table A10: $\mathcal{M} = 3$). The short $185^{\rm y}$ time span of the First $185^{\rm y}$ data prevents the detection of this correct $219^{\rm y}$ period. The correct $219^{\rm y}$ signal trend turns upwards more slowly than the wrong $172^{\rm y}$ signal trend. This is the simple reason for the failure of our 50 yr prediction for the First $185^{\rm y}$ data.

The Last $50^{\rm y}$ data prediction error shows a peculiarity that seems to defy the laws of statistics. First, the $\pm 3\sigma$ prediction error increases, as one would expect (Figure 3(b): green dotted lines). Surprisingly, this prediction error then begins to decrease, and the prediction becomes very accurate close to HJD 2450000. After this, the prediction error begins to increase again. This peculiarity certainly requires an explanation.

The reason for this peculiarity could already be inferred from the black interference curve in Figure A3 (lowest right panel: $P_1 = 24771$). The scatter of the $g(t)$ interference curve is not the same at all phases. In this particular case, this scatter increases close to the maxima, but it decreases close to the minima. The largest and the smallest scatter coincides with the phases when the first time derivative fulfills $\dot{g}(t) = 0$.

However, the above-mentioned effects in Figure A3 are caused by interference of only two signals, while the peculiar error limit effect in Figure 3 occurs in the $\mathcal{M} = 4 + 6$ model sum of six signals. We show this model for 20 bootstrap samples in Figure A14 (red dotted curves). The scatter of these curves increases when the predictive data end at the dotted black vertical line. However, all dotted red curves converge close to the vertical continuous black line at HJD 2450000. After this line, they diverge again. Before this line, the data show an increasing trend, but the positive slope is decreasing (Figure 3(a): red circles). A suitable model would be $\dot{g}(t) > 0$ and $\ddot{g}(t) < 0$. After this line, this slope is still positive, but it is increasing. Now, the suitable model would be $\dot{g}(t) > 0$ and $\ddot{g}(t) > 0$. This means that there is a turning point $\dot{g}(t) = 0$ close to this HJD 2450000 epoch, where the $\ddot{g}(t)$ sign changes from negative to positive. The second-derivative sign change of *any* function forces this function to change its direction twice. This $\mathcal{M} = 4 + 6$ model turning point forces the bootstrap model solutions to converge. This simple effect explains why the prediction error increases, decreases, and again increases (Figure 3: green dotted lines).

Our turning-point hypothesis would explain the gap in $O - C$ data close to HJD 2450000 (Figure A14: vertical continuous line). There are no such gaps in Algol's modern $O - C$ data, not even during the two world wars. The TIDAK database contains only four $O - C$ values between HJD 2448288 and HJD 2449988 (≡4.6 yr). Even today, one of these four is still marked "unpublished" (1997, Drozdz: HJD 2449317.4171). Close to the above-mentioned turning point, the $O - C$ data no longer supported the well-established expected long-term $\dot{g}(t) > 0$ and $\ddot{g}(t) < 0$ trend. Perhaps for this reason, contradictory new data were not published at that time. Only when the new $\dot{g}(t) > 0$ and $\ddot{g}(t) > 0$ trend was securely established did the continuous flow of supporting $O - C$ observations begin again.

We conclude that, except for the first few years, our Last $50^{\rm y}$ data prediction fails. However, our turning-point epoch prediction of HJD 2450000 is excellent.

5.4. Additional Experiments

We divide all original data into two parts. Both halves are too short for the detection of the long 219 yr period. This hampers their period analysis. In the first low-accuracy half, we detect only one signal of about 137 yr. From the more accurate second half, we detect four signals of 1.86 30.9, 39.7, and

103.3 yr. The shortest one is equal to the orbital period of Algol C.

We also test two alternatives, where the weights of observations increase linearly. In two alternative experiments, the weights are doubled or quadrupled during the time span of all data. In both cases, the five strongest signals detected from the weighted data are identical to those detected from nonweighted data (Table A7, $\mathcal{M} = 3{+}6$ model).

5.5. *Signals Identified in All Data*

The eccentric orbit analysis indicates that all data contains five signals (Table A7, $\mathcal{M} = 3{+}6$). Here, we argue that the correct number of signals may also be six. We use bold letters $\boldsymbol{p}_1$, $\boldsymbol{p}_2$, $\boldsymbol{p}_3$, $\boldsymbol{p}_4$, $\boldsymbol{p}_5$, and $\boldsymbol{p}_6$ for the periods of these signals (Table 1). This notation helps the readers to separate these six periods from the numerous other $P_1, P_2, \ldots, P_6, p, p_1, p_2, p_3$, and p' periods. We use the tentative names Algol C, Algol D, Algol E, Algol F, Algol G, and Algol H for the objects possibly connected to these periods. The corresponding peak to peak amplitudes are $\boldsymbol{A}_1$, $\boldsymbol{A}_2$, $\boldsymbol{A}_3$, $\boldsymbol{A}_4$, $\boldsymbol{A}_5$, and $\boldsymbol{A}_6$.

Our six-signal argument relies on two tables. The first table compares the eccentric and circular orbit analysis periods for all data (Table A13). The second table compares the periods detected in three different samples: All data, First 226^{y} data, and First 185^{y} data (Table A14).

In our Appendix, we apply DCM to simulated $O - C$ data (Equation (13)). We show that the four following different effects are encountered when the $O - C$ data contains either one period p, or two periods p_1 and p_2.

"Correct-p": DCM detects the correct period p.
"Half-p": DCM detects the spurious period $p/2$.
"Double-p": DCM detects the spurious period $2p$.
"Interference-p'": DCM detects the spurious period p' caused by p_1 and p_2 interference (Equation (A7)).

The "Half-p" and "Double-p" effects can mislead the DCM analysis of low-eccentricity $O - C$ curves, which resemble pure sinusoids.

There is only one minimum and one maximum in the real $O - C$ curve caused by the LTTE of a single third body. This third body can approach and recede only once during one orbital period p. Hence, the $O - C$ "p' interference" curves having two minima and two maxima cannot be caused by one body alone, but they may indicate the presence of more than one body.

In Sections 5.5.1–5.5.5, we illustrate one $\boldsymbol{p}_1$, $\boldsymbol{p}_2$, $\boldsymbol{p}_3$, $\boldsymbol{p}_4$, $\boldsymbol{p}_5$, and $\boldsymbol{p}_6$ signal at a time and how the four effects mentioned above can explain all eccentric and all circular orbit DCM period search results.

5.5.1. *Signal* $\boldsymbol{p}_6 = 79999^{d} = 219^{y}.0$

The circular orbit signal period $P_{c,7} = 120740^{\mathrm{d}} \pm 41002^{\mathrm{d}}$ differs by about $\pm 1\sigma$ from the eccentric orbit period $\boldsymbol{p}_6 = P_{e,5} = 79999^{\mathrm{d}} \pm 1216^{\mathrm{d}}$ (Table A13). Hence, the circular and eccentric orbit analyses give the same correct $\boldsymbol{p}_6$ period ("Correct-p" effect).

This $\boldsymbol{p}_6$ period is two times longer than the next circular orbit period $P_{c,6} = 42422^{\mathrm{d}} \pm 640^{\mathrm{d}}$ ("Half-p" effect). The $\boldsymbol{p}_6 = 219^{\mathrm{y}}$ signal curve shows only one minimum and one maximum (Figure A8: lowest panel, green curves), because the two strongest circular orbit $P_{c,7}$ and $P_{c,6}$ signals are "in phase." These results confirm that DCM succeeds in detecting the p and $p/2$ regularities illustrated in Figure A1 and Table A3.

DCM detects the $\boldsymbol{p}_6 = 219^{\mathrm{y}}$ signal in all data and First 226^{y} data (Table A14). The too-short First 185^{y} data time span prevents the detection of the $\boldsymbol{p}_6$ period. Therefore, the largest detected $P_4 = 62992^{\mathrm{d}} \pm 2499^{\mathrm{d}}$ period differs by more than $\pm 3\sigma$ from $\boldsymbol{p}_6$.

We use an amplitude estimate $\boldsymbol{A}_6 = A_{e,5} = 0^{\mathrm{d}}.287 \pm 0^{\mathrm{d}}.005$ for this $\boldsymbol{p}_6 = 219^{\mathrm{y}}$ signal (Table A13).

5.5.2. *Signals* $\boldsymbol{p}_5 = 24247^{d} = 66.^{y}4$ *and* $\boldsymbol{p}_4 = 12294^{d} = 33.^{y}7$

The connection between the eccentric orbit $\boldsymbol{p}_5 = P_{e,4} = 24{,}742^{\mathrm{d}} \pm 141^{\mathrm{d}}$ signal and the circular orbit $P_{c,5} = 24{,}747^{\mathrm{d}} \pm 872^{\mathrm{d}}$ signal is definitely the "Correct-p" effect (Table A13). The "Half-p" effect certainly connects this $\boldsymbol{p}_5$ signal also to circular orbit $P_{c,4} = 12{,}294^{\mathrm{d}} \pm 109^{\mathrm{d}}$ signal.

However, two questions need to be answered. Why does the $\boldsymbol{p}_5 = 66.^{\mathrm{y}}4$ signal show two minima and two maxima (Figure A8: midpanel, blue curves)? This is impossible for any single third-body eccentric orbit. Why are the $A_{c,5}$ and $A_{c,4}$ amplitudes of the two circular orbit $P_{c,5}$ and $P_{c,4}$ signals practically equal (Table A13)?

The easiest answer to both questions would be that the $\boldsymbol{p}_5 = 66.^{\mathrm{y}}4$ and $\boldsymbol{p}_4 = 33.^{\mathrm{y}}7$ signals represent two separate independent signals, which are "off phase." Their "Interference-p'" effect could induce the two unequal minima and two unequal maxima of the blue $O - C$ curve (Figure A8), which resembles the black interference curve in Figure A3. In this case, the circular orbit $P_{c,4} = 12294^{\mathrm{d}} \pm 109^{\mathrm{d}}$ signal could represent a real fourth independent $\boldsymbol{p}_4 = 33.^{\mathrm{y}}7$ signal.

The $\boldsymbol{p}_5 = 66.^{\mathrm{y}}4$ signal is detected in all data and First 226^{y} data (Table A14). This $\boldsymbol{p}_5$ signal is not detected in the shortest First 185^{y} data sample, but the $\boldsymbol{p}_4 = 33.^{\mathrm{y}}7$ signal is. We conclude that the $\boldsymbol{p}_5 = 66.^{\mathrm{y}}4$ and $\boldsymbol{p}_4 = 33.^{\mathrm{y}}7$ signals are most probably two independent real signals.

The amplitudes of the circular orbit $P_{c,5}$ and $P_{c,4}$ signals give our $\boldsymbol{A}_5 = A_{c,5} = 0^{\mathrm{d}}.018 \pm 0^{\mathrm{d}}.002$ and $\boldsymbol{A}_4 = A_{c,4} = 0^{\mathrm{d}}.018 \pm 0^{\mathrm{d}}.001$ amplitude estimates for the $\boldsymbol{p}_5$ and $\boldsymbol{p}_4$ signals (Table A13).

Here, we have shown that the eccentric orbit $\boldsymbol{p}_5 = 66.^{\mathrm{y}}4$ signal may arise from the "Interference-p'" effect of two circular orbit $\boldsymbol{p}_5 = 66.^{\mathrm{y}}4$ and $\boldsymbol{p}_4 = 33.^{\mathrm{y}}7$ sinusoids. Later, we will present an alternative explanation (Figure A15: Configurations 2 and 3).

5.5.3. *Signal* $\boldsymbol{p}_3 = 10{,}144^{d} = 27.^{y}8$

None of the eccentric orbit periods is close to the circular orbit period $P_{c,3} = 10{,}144^{\mathrm{d}} \pm 30^{\mathrm{d}} = 27.^{\mathrm{y}}8 \pm 0.^{\mathrm{y}}1$ (Table A13). However, the "Double-p" effect certainly connects this $P_{c,3}$ period to the eccentric orbit period $P_{e,3} = 20358^{\mathrm{d}} \pm 128^{\mathrm{d}}$. This $P_{e,3}$ signal shows two maxima and two minima (Figure A8: lower panel, red curves). These two equal maxima and two equal minima are symmetric. This kind of symmetry is detected in our simulations of low-eccentricity spurious double sinusoids (Table A2: "Dp" ≡ "Double-p" effect). Therefore, the $P_{c,3}$ period probably represents a real signal $\boldsymbol{p}_3 = 27.^{\mathrm{y}}8$.

The eccentric orbit $P_{e,3} = 20{,}358^{\mathrm{d}}$ signal is detected in all data, First 226^{y} data, and First 185^{y} data (Table A14). This means that DCM detects the $\boldsymbol{p}_3 \approx P_{e,3}/2$ signal in all three different samples.

Our amplitude estimate for this $\boldsymbol{p}_3 = 27.^{\rm y}8$ signal is $\boldsymbol{A}_3 = A_{c,3} = 0^{\rm d}.0097 \pm 0^{\rm d}.0004$ (Table A13).

In this section, we have shown that the eccentric orbit $P_{e,3} = 56.^{\rm y}0$ signal probably represents the "double wave" of the $\boldsymbol{p}_3 = 27.^{\rm y}8$ signal. We will later present an alternative explanation (Figure A15: Configuration 3).

5.5.4. Signal $\boldsymbol{p}_2 = 7269^{\rm d} = 20.^{\rm y}0$

The eccentric orbit $\boldsymbol{p}_2 = P_{e,2} = 7269^{\rm d} \pm 29^{\rm d}$ signal and the circular orbit $P_{c,2} = 7395^{\rm d} \pm 37^{\rm d}$ signal are certainly connected (Table A13: "Correct-p" effect).

Like any real third-body $O - C$ curve, this $\boldsymbol{p}_2 = 20.^{\rm y}0$ signal shows only one minimum and one maximum (Figure A11: lower panel blue curves). DCM detects this $\boldsymbol{p}_2 = 20.^{\rm y}0$ signal in all data and First $226^{\rm y}$ data (Table A14). In the shortest First $185^{\rm y}$ data sample, this $\boldsymbol{p}_2$ period may be connected to its double period $P_3 = 15429^{\rm d} \pm 222^{\rm d}$ (Table A14: "Double-p" effect).

Our amplitude estimate for this $\boldsymbol{p}_2 = 20.^{\rm y}0$ signal is $\boldsymbol{A}_2 = A_{e,2} = 0^{\rm d}.007 \pm 0^{\rm d}.001$ (Table A13).

5.5.5. Signal $\boldsymbol{p}_1 = 680.4^{\rm d} = 1.^{\rm y}86$

The eccentric orbit and circular orbit DCM searches give the same $\boldsymbol{p}_1 = 680^{\rm d}.4 \pm 0^{\rm d}.4 = 1.^{\rm y}863 \pm 0.^{\rm y}001$ signal (Table A13: "Correct-p" effect).

DCM detects this $\boldsymbol{p}_1 = 1.^{\rm y}863$ signal from all three samples (Table A14). Like any real $O - C$ curve, this signal shows only one minimum and one maximum (Figure A11: higher panel red curves).

We use $\boldsymbol{A}_1 = A_{e,1} = 0^{\rm d}.0064 \pm 0^{\rm d}.0007$ (Table A13). This signal is discussed later in greater detail (Section 6.3).

5.5.6. Two Weakest Signals

DCM detects indications of two additional weaker signals $P_{c,2} = 2986^{\rm d} \pm 39^{\rm d}$ (Table A12) and $P_2 = 3387^{\rm d} \pm 17^{\rm d}$ (Table A14). They could be separate signals because their $\pm 3\sigma$ error limits do not overlap. They are 0.80 and 0.45 weaker than the weakest detected $\boldsymbol{p}_1 = 1.^{\rm y}863$ signal. We cannot confirm whether these two weakest signals are real or spurious.

6. Discussion

Applegate's (1992) mechanism cannot explain the numerous strictly periodic $O - C$ signals of Algol, because quasi-periodic activity cycles are never regular. Apsidal motion follows only one period. The LTTE of Algol's companion candidates could cause these numerous strictly periodic cycles. Assuming circular orbits, we use $m_1 = 3.7 m_\odot$ and $m_2 = 0.8 m_\odot$ (Zavala et al. 2010) to compute the m_3 mass and the a_3 semimajor axis estimates for these tentative companion candidates (Table 1). These approximate mass and semimajor axis estimates are obtained by assuming that each candidate is a "third" component. The effects of other candidates inside the orbit of the "third" component are ignored in Equations (18) and (19).

6.1. Hierarchical Structure

We call the eclipsing Algol A and Algol B pair the central eclipsing binary (cEB). Algol C is called a wide-orbit star (WOS), as well as all other new tentative companion candidates. We use the same hierarchical system diagrams as Tokovinin (2021).

Our first hierarchical system diagram shows the circular orbit $i = 90°$ inclination case of Table 1 (Figure A15: Configuration 1). The eight members in this configuration are cEB and six WOSs. The orbital periods of WOS candidates are between 1.863 and 219.0 yr. The most massive ($m_3 = 2.50 m_\odot$) companion candidate, Algol H, is also the most distant one ($a_3 = 44.7$ au). The four other WOS candidates are low-mass stars ($0.23 m_\odot \leqslant m_3 \leqslant 0.43 m_\odot$). The closest $m_3^{i=90} = 1.16 m_\odot$ companion candidate has an orbital period $\boldsymbol{p}_1 = 680^{\rm d}.4 \pm 0^{\rm d}.4$, which is close to the known orbital period $P_{\rm orb} = 679^{\rm d}.85 \pm 0^{\rm d}.04$ of Algol C (Zavala et al. 2010). We will discuss this probable detection of Algol C later in Section 6.3.

Our second hierarchical system diagram shows one alternative for Configuration 1 (Figure A15: Configuration 2). The seven members are cEB and five WOSs. We have already shown that the sum of "off-phase" sinusoidal $\boldsymbol{p}_5 = 66.^{\rm y}4$ and $\boldsymbol{p}_4 \approx \boldsymbol{p}_5/2 = 33.^{\rm y}7$ signals can cause the $\boldsymbol{p}_5 = 66.^{\rm y}4$ period double wave (Section 5.5.2). However, a single $\boldsymbol{p}_5 = 66.^{\rm y}4$ long-period binary can cause a similar effect if the masses of its members are unequal. These unequal masses could also explain the two unequal maxima and minima of the blue $O - C$ curve in Figure A8. The red lines in our Configuration 2 diagram show this hypothetical long-period $\boldsymbol{p}_5 = 66.^{\rm y}4$ binary having an orbital period $\boldsymbol{p}_6 = 219.^{\rm y}0$ around the barycentre of the whole system (Figure A15).

Our third hierarchical system diagram is a minor modification of Configuration 2 (Figure A15: Configuration 3). The seven members are, again, cEB and five WOSs. Now we take the five periods of the $\mathcal{M} = 3 + 6$ model as such. Signal $66.^{\rm y}4$ is not separated into two signals (Section 5.5.2). We use the full $P_{e,3} = 55.^{\rm y}8$ signal period, not the half of this period (Section 5.5.3). This $P_{e,3} = 55.^{\rm y}8$ signal could also represent a long-period binary, where the masses of both components are approximately equal. In Configuration 3, the two long-period $\boldsymbol{p}_5 = 66.^{\rm y}4$ and $P_{e,3} = 55.^{\rm y}8$ binaries orbit each other during $\boldsymbol{p}_6 = 219.^{\rm y}0$. This may be the most stable one of our three configuration alternatives, because the cEB and the remaining two inner-orbit WOSs would only weakly perturb the two hypothetical long-period binaries, and vice versa. This type of quintuple binary system has been discovered (e.g., Zasche & Uhlař 2013, their Figure 2 of V994 Her).

6.2. Detectability

In binaries, the radial velocity observations can reveal the presence of a third body, like in the discovery of Algol C (Curtiss 1908). For nearby hierarchical systems, combined astrometric orbit and radial velocity observations can be used to solve their detailed structure (e.g., Tokovinin 2021). When Hajdu et al. (2019) searched for WOSs from the $O - C$ data of 80,000 EBs, they detected 992 systems having one WOS, but only 4 systems possibly had two WOSs. Our DCM analysis of Algol's $O - C$ data suggests the presence of five or six WOSs. These $O - C$ data cannot reveal a lot about the structure of this hierarchical system, not even the exact number of stars (Figure A15: Configurations 1, 2, or 3). However, we can give some ideas that may help in the detection of Algol's WOS candidates. Here, we assume that the candidate orbits are circular and their orbital plane inclinations are $i_3 = 90°$ (Table 1). In Configuration 1, the observed maximum and minimum radial velocities of WOS candidates are

$$v_{\rm max} = v_0 + \frac{2\pi a_3}{p_3} \qquad (21)$$

$$v_{\rm min} = v_0 - \frac{2\pi a_3}{p_3}, \qquad (22)$$

where $v_0 = 4.0 \ {\rm km\ s^{-1}}$ is Algol's radial velocity (Wilson 1953).

The angular distance between Algol and its WOSs changes constantly. We compute these angular distance changes in Algol's cEB frame of rest. At the $O-C$ curve minima and maxima, the largest distance changes are

$$\Delta a_{\rm max}(\Delta t) = 2a_3 \sin(\pi \Delta t / p_3) \qquad (23)$$

during a time interval $\Delta t \leqslant p_3/2$. For longer time intervals, we use $\Delta t = p_3/2$, which gives $\Delta a_{\rm max} = 2a_3$. The smallest

$$\Delta a_{\rm min}(\Delta t) = a_3[1 - \cos(\pi \Delta t / p_3)] \qquad (24)$$

distance changes coincide with the $O-C$ curve mean level. This relation holds for $t_0 \leqslant p_3$. For longer time intervals, we use $\Delta t = p_3$, which gives $\Delta a_{\rm min} = 2a_3$.

The proper motion of Algol is $\mu_0 = 2.49 \ {\rm mas\ yr^{-1}}$ (van Leeuwen 2007). The minimum and maximum proper motion of each candidate is

$$\mu_{\rm min} = \mu_0 - \mu_c \qquad (25)$$

$$\mu_{\rm max} = \mu_0 + \mu_c, \qquad (26)$$

where $\mu_c = \Delta a_{\rm max}(\Delta t = 1^{\rm y})$ is the maximum proper motion during 1 yr. Note that $\mu_{\rm min} = 0$ for every candidate, because their $\mu_c > \mu_0$.

We emphasize that our $\Delta a_{\rm min}$ and $\Delta a_{\rm max}$ estimates refer to the candidate distance changes with respect to cEB, while our $\mu_{\rm min}$ and $\mu_{\rm max}$ estimates refer to the proper motion of all members in the sky.

All parameters of Equations (21)–(26) are given in Table A15. The two estimates for $\Delta a_{\rm min}$ and $\Delta a_{\rm max}$ are computed for observations spanning 5 or 20 yr. This information is useful for future searches of our Algol member candidates.

In 2020 December, the latest third Gaia data release (DR3) confirmed no certain detections $\pm 4''$ around Algol and only one certain $\pm 40''$ detection. In their analysis of Gaia DR3 data, Torra et al. (2020) note that "most problems come from the bright sources and the strange image profiles." They rejected 8159.3 million bright sources, 158.0 million very bright sources, and 4066.7 million odd window profiles. Algol is definitely "too bright." Its brightness profile is constantly changing due to the movement of the known members Algol A, Algol B, and Algol C, let alone due to the primary and secondary eclipses. Therefore, Gaia could not have measured the positions and movements of the objects in our Table A15.

The Algol H candidate would be easiest to detect because its distance from the cEB is the largest. This most massive candidate is very probably also the brightest candidate. At the moment, its $O-C$ curve is close to the mean level (Figure A8: left-hand lowest panel green $h_3(t)$ curve). Hence, Algol H would be close to its projected maximum $a_3 = 1569$ mas distance from cEB. The cEB is receding from us because its $O-C$ values are increasing for the next 50 yr. Currently, Algol H would be approaching us at its minimum radial velocity $v_{\rm min} = -2 \ {\rm km\ s^{-1}}$ (Table A15). The distance changes between cEB and Algol H would be small, only $\Delta a_{\rm min} = 4$ or 64 mas during the next 5 or 20 yr.

Direct interferometric images have been obtained of Algol A, Algol B, and Algol C (e.g., Zavala et al. 2010; Baron et al. 2012). If Algol B and Algol C really are less massive than our distant Algol H candidate, why did the earlier interferometric imaging not reveal the presence of this massive candidate? First, this Algol H candidate is about 20 times farther away from the cEB than Algol C, which means that the area of interferometric imaging should have been about $20 \times 20 = 400$ larger. Second, this Algol H candidate could be a long-period binary, where both members are much less massive and much dimmer than a single $2.50 m_{\odot}$ star (Figure A15: Configurations 2 and 3). One or two members of this long-period binary could be an evolved object, like a white dwarf. Third, Zavala et al. (2010) and Baron et al. (2012) applied a three-star model. Algol H's contribution to their modeled total flux would have remained constant because its position did not change during their observations (Table A15). We conclude that using an over 400 times larger imaging area, and a model of at least four stars, may lead to the interferometric detection of this distant Algol H candidate. The detection of the other four less massive candidates with this technique is much more challenging (Table 1: $i = 90°$, $0.23 m_{\odot} \leqslant m_3 \leqslant 0.43 m_{\odot}$). However, the $\Delta a_{\rm min}$ and $\Delta a_{\rm max}$ values of these less massive candidates show that their movements are easier to detect even during shorter periods of observations (Table A15).

Powell et al. (2021) studied the sextuple-eclipsing binary system TIC 168789840 with the speckle interferometry technique. They could resolve this hierarchical system of three eclipsing binaries. Their estimate for the outer period in this hierarchical system was about 2000 yr. Algol is about 20 times closer to us than TIC 168789840 ($d \approx 570$ pc). The orbital period of our Algol H candidate is about 200 yr. Hence, it might be possible to detect Algol H with speckle interferometry.

6.3. Algol C Detection

DCM detects the weakest $\boldsymbol{p}_1 = 680\overset{\rm d}{.}4 \pm 0\overset{\rm d}{.}4$ signal in all three samples: all data, First $226^{\rm y}$ data, and First $185^{\rm y}$ data. This $\boldsymbol{p}_1$ signal is 44.8 times weaker than the strongest $\boldsymbol{p}_6$ signal (Table 1). DCM detects this weakest $\boldsymbol{p}_1$ signal although it is buried under the interference of five stronger $\boldsymbol{p}_2$, $\boldsymbol{p}_3$, $\boldsymbol{p}_4$ $\boldsymbol{p}_5$, and $\boldsymbol{p}_6$ signals and a linear $p(t)$ trend. The period of this $\boldsymbol{p}_1$ signal differs only 1.4σ from the known orbital period $P_{\rm orb} = 679\overset{\rm d}{.}85 \pm 0\overset{\rm d}{.}04$ of Algol C (Zavala et al. 2010). This indicates that all other five detected stronger signals are real periodicities, but it does not irrefutably prove this idea. Our $O-C$ data contains 127 rounds of Algol C around Algol AB, and this orbit is known to be stable (Zavala et al. 2010; Baron et al. 2012; Jetsu et al. 2013). Our lower limit for the mass of Algol C (Table 1: $i = 90°$ and $1.2 m_{\odot}$) is smaller than the interferometric estimates by Zavala et al. (2010, $i = 83\overset{\circ}{.}7 \pm 0\overset{\circ}{.}1$ and $1.5 \pm 0.1 m_{\odot}$) and Baron et al. (2012, $i = 83\overset{\circ}{.}66 \pm 0\overset{\circ}{.}03$ and $1.76 \pm 0.15 m_{\odot}$). This indicates that not even DCM can retrieve the full amplitude of this weak Algol C signal when it is buried under five stronger signals and a linear trend.

6.4. Stability

All detected signals are strictly periodic because they are also detected in the 9.2 yr shorter subsample First $226^{\rm y}$ data. Except for the $\boldsymbol{p}_2$ and $\boldsymbol{p}_5$ signals, the other four signals are also detected in the 50 yr shorter subsample First $185^{\rm y}$ data. This apparent absence of these two $\boldsymbol{p}_2$ and $\boldsymbol{p}_5$ signals in First $185^{\rm y}$ data could be explained by the "Half-p" and "Double-p" effects (Table A14). However, strict periodicity alone does not prove that Algol's hierarchical system is stable.

The perturbations of WOS can cause periodic cEB orbital plane changes (Soderhjelm 1975, Equation (27)). Such long-term orbital plane changes with respect to the line of sight may even stop the eclipses completely, or at least reduce the depth of eclipses, as in the case of AY Mus (Soderhjelm 1974). However, the cEB orbital plane is stable for $\Psi = 0°$ or $90°$, where Ψ is the angle between the cEB and WOS orbital planes. This is the case for Algol C, the only currently known WOS of Algol (Baron et al. 2012, $\Psi = 90^{\circ}\!.20 \pm 0^{\circ}\!.32$). No changes have been observed in the eclipses of Algol in modern times, and these events were most probably also observed over 3000 yr ago (Jetsu et al. 2013). This is possible only if all WOSs have $\Psi = 0°$ or $90°$. If the orbital planes of all WOS are coplanar, then all WOSs must have $\Psi = 90°$, because this is the known case for Algol C. If all WOS orbits were not coplanar, this would certainly reduce the stability of this system and perhaps also weaken or stop the observed eclipses.

The mass transfer from the less massive Algol B to the more massive Algol A should increase the orbital period (Kwee 1958, Equation (5)). The numerous published mass transfer rate estimates range from $10^{-13}\ m_{\odot}\,{\rm yr}^{-1}$ to $10^{-7}\ m_{\odot}\,{\rm yr}^{-1}$ (Jetsu et al. 2013, Section 4). However, no regular long-term period increase has been observed since Goodricke (1783) discovered Algol's periodicity. All WOSs can also perturb the cEB by other physical mechanisms, like the Kozai effect (Kozai 1962), or the combination of the Kozai cycle and tidal friction (Fabrycky & Tremaine 2007). Against this background, our linear $K_3 = 1$ trend result for $p(t)$ is surprising (Section 5.1.1). For 236 yr, Algol's orbital period has been constant,

$$P_{\rm orb} = \left(\frac{1}{P_0} - \frac{2M_1}{\Delta T}\right)^{-1} = 2^{\rm d}\!.86732870, \qquad (27)$$

where $P_0 = 2^{\rm d}\!.86730431$ (Equation (1)) and $M_1 = 0.1278$ is the $p(t)$ coefficient for the $\mathcal{M} = 3$ model in Table A7. This causes the linear $O - C$ change of $0^{\rm d}\!.256$ in Figure A7 (upper panel: dotted line). It also means that LTTE effects alone can explain all observed $O - C$ changes. No additional effects, like the quadratic $K_3 = 2$ trend caused by mass transfer, are needed to explain these $O - C$ data.

In the future, long-term integrations may confirm the dynamical stability of this system. Currently, even the exact number of WOS candidates remains unknown, because three different hierarchical system diagrams can explain the detected WOS periods (Figure A15: Configurations 1, 2, and 3). For any WOS period p_3, the correct m_3, e_3, a_3, i_3, ω_3, and Ψ_3 initial value combinations for the long-term integrations are also unknown. Therefore, our $O - C$ data cannot give an unambiguous solution for this stability problem. Whether or not this system is stable, we can determine the p_3 periods that are observed today.

6.5. Predictability

We admit that an unambiguous identification of all individual signals from the interference sum of numerous signals is not always possible. One example is the $\boldsymbol{p}_5$ and $\boldsymbol{p}_4$ signal identification in Section 5.5.2. However, this whole identification problem is irrelevant from the predictability point of view. The sum of identified signals is equal to the sum of unidentified signals. Both alternatives give the same prediction.

The linear and quadratic EB ephemerides cannot predict the exact epochs of future eclipses (e.g., Kreiner et al. 2001; Kim et al. 2018). For $O - C$ changes caused by a third body, these predictions also usually fail, as in Bours et al. (2014, their Figure 7), Lohr et al. (2015) or Song et al. (2019, their Figure 1). Different $O - C$ subsets can give different periods, but this does not mean that there is something wrong with the period search methods themselves, like DCM. Our 9.2 yr $O - C$ prediction for Algol is based on First $226^{\rm y}$ data (Figure 2). Strict periodicity can explain why this prediction succeeds. Predictability is impossible without strict periodicity. This prediction would fail, if even one of our detected signals were not strictly periodic, or if the $K_3 = 1$ linear $p(t)$ trend were wrong.

Our next 50 yr prediction is based on First $185^{\rm y}$ data. Except for the first few years, this long-term prediction fails (Figure 3). The reason for this failure is simple. The longest $172^{\rm y}$ period detected from First $185^{\rm y}$ data is not correct. The short $\Delta T = 185$ yr time span of this sample prevents the detection of the correct signal period $219^{\rm y}$. This correct signal can be detected only from all data and First $226^{\rm y}$ data. Together with the $0^{\rm d}\!.26$ trend $p(t)$, this highest $0^{\rm d}\!.29$ amplitude dominating $219^{\rm y}$ signal determines all long-term $O - C$ predictions. The insignificant long-term trend contribution of all other weaker signals is always less than $\pm 0^{\rm d}\!.03$, because the sum of their amplitudes is $0^{\rm d}\!.06$. Although our 50 yr prediction for the $O - C$ level fails (Figure 3), we get an excellent prediction for the turning-point epoch at HJD 2450000 (Figure A14).

New $O - C$ data after 2018 October can already be used to test our prediction for the next 10 yr (Figure 1(b)). These predictions should improve in the future, when all orbital period estimates become more accurate. Predictability should ultimately prove that all these signals are orbital periods. At the moment, we cannot prove this. In the history of astronomy, the seasons of the year posed a similar problem. Their 1 yr periodicity was detected easily, but the reasons for it were understood much later: the orbit of Earth around the Sun, and the tilted axis of Earth. However, it was possible to predict the seasons without understanding their origin. Our detected periods of Algol are certainly there, and for some reason or another, they can be used for predictions.

6.6. Look-elsewhere Effect

We test over 30 models having free parameters between $\eta = 6$ and 22 (Tables A6–A11). The total number of free parameters is even higher when the model for the original data is added to the model for the residuals. For example, the best $\mathcal{M} = 3 + 6$ model for all data has $\eta = 17 + 11 = 28$ free parameters (Figure 1). Our search for the correct model over a vast parameter space increases the probability for finding spurious apparently significant signals. This is called the "look-elsewhere effect" (e.g., Miller 1981; Bayer & Seljak 2020). There are statistical methods that can account for the "look-elsewhere effect" and give direct significance estimates S for the periods of models having different degrees of freedom (e.g., Bayer & Seljak 2020, their Equation (3.12)).

DCM applies the Fisher test to compare the significance of all pairs of simple and complex models. The Fisher test identifies the best model among all tested models (Equations (11) and (12)). This approach does not account for the "look-elsewhere effect", because it gives no direct significance estimate S for the periodicities of this best model. Nevertheless, we can present several arguments indicating that the "look-elsewhere effect" has no significant impact on our results.

1. We apply the robust Fisher test to compare any complex model having more signals than any simple model. We use the preassigned significance level $\gamma_F = 0.001$ to reject the simple model (Equation (12)). This prevents overfitting because the probability that this best model selection fails is always smaller than 1 out of 1000. In many cases, the extreme $Q_F < 10^{-16}$ critical levels confirm that the complex model is absolutely certainly better than the simple model. This confirms that the data contain more signals than those present in the simple model. Our indirect Q_F significance estimates confirm the presence of additional complex model periodicities, but they do not give us direct S significance estimates for these periodicities. Regardless of the "look-elsewhere effect", the Fisher test can confirm that the five-signal $\mathcal{M} = 3 + 6$ model is the best model for all data.
2. The z periodogram values of close tested frequencies correlate and display no sudden jumps (see Section 3: Caveat 2). At some tested frequency grid density level, this means that the detected period values no longer depend on the number of tested periods (Paper I: n_L and n_S). These unambiguous best period values are obtained from linear models. Increasing the number of tested periods does not change the values of these detected periods. Hence, the tested frequency grid density is not a trial factor effect ("look-elsewhere effect") that can change the five-period values of our best $\mathcal{M} = 3 + 6$ model.
3. For all $O - C$ data, we use the Fisher test to compare constant, linear, quadratic, and cubic $p(t)$ trends for one-, two-, and three-signal models (Table A6). The linear $K_3 = 1$ trend is the best one. This means that if the $O - C$ data had been computed with the period $2\overset{\mathrm{d}}{.}86732870$ (Equation (27)), the best trend would have been the constant $K_3 = 0$ trend. After exploring numerous trend and signal combination alternatives in the vast free parameter space, we arrive at this simplest alternative: no trend at all in the $O - C$ data! Although the "look-elsewhere effect" is certainly present, DCM detects this simplest trend alternative for our five-signal $\mathcal{M} = 3 + 6$ model.
4. Our $\mathcal{M} = 3 + 6$ model prediction is excellent (Figure 2). This indicates that the "look-elsewhere effect," or any other spurious effect, does not mislead DCM periodicity detection.

6.7. Uncertainties

The time span of our data is "only" 236 yr. Our biggest uncertainty is therefore the longest detected 219 yr periodicity. It has been claimed that the DFT can sometimes detect clear signal periods slightly longer than the ΔT time span of data, "but with poor resolution" (Horne & Baliunas 1986). The detection of periods close to ΔT depends strongly on the signal-to-noise ratio of the data. Such detections may not always succeed in our case, because we detect the 172 yr period from the shortest sample of 185 yr. This period is shorter than the time span of this particular sample. We do not detect this "old" 172 yr period from the longer samples of 226 and 236 yr, but we do detect the "new" 219 yr period. New additional $O - C$ data may, or may not, confirm that this 219 yr period of ours is correct.

The direct discovery of Algol H would solve the above problem for good. Eggen (1948) analyzed Algol's $O - C$ data. He arrived at an orbital period of 188.4 yr for this hypothetical distant companion. Irwin (1952) estimated its orbital elements. We argue that this distant Algol H candidate may be currently found about $1\overset{''}{.}6$ away from the cEB, the eclipsing pair Algol A and Algol B.

As for other uncertainties, we cannot determine the exact number of stars in this hierarchical system, but this does not prevent us from presenting an excellent 9.2 yr prediction based on the first 226 yr of $O - C$ data (Figure 2). We admit that our longer 50 yr prediction fails because our 172 yr period detected in the shortest 185 yr sample is wrong (Figure 3). However, our turning point in this same prediction would explain the 4 yr gap in the published $O - C$ data around the year 1995 (Figure A14). It will be interesting to see how well we can predict future $O - C$ data after 2018 October (Figure 1(b)).

7. Conclusions

The ephemerides of EBs can be improved by removing linear or quadratic trends from the observed (O) minus computed (C) eclipse epochs (e.g., Kreiner et al. 2001; Kim et al. 2018). However, even such improved ephemerides cannot predict the exact epochs of future eclipses. The LTTE of a third body causes strictly periodic predictable $O - C$ changes (Irwin 1952). The typical third- and fourth-body detection rates from $O - C$ data are low, only 992/80,000 and 4/80,000, respectively (Hajdu et al. 2019). Eclipse epoch predictions based on linear or quadratic trends, and LTTEs, usually fail because aperiodic trends mislead the detection of periodic signals (e.g., Bours et al. 2014; Lohr et al. 2015; Song et al. 2019).

Considering this general background, it is unprecedented that our new DCM can detect five strictly periodic signals from 236 yr of Algol's $O - C$ data (Figure 1(a)). These tentative companion candidate orbital periods are between 1.863 and 219.0 yr. One of these periods is definitely not a surprise, because our 680.4 ± 0.4 day period estimate for the weakest detected signal differs only 1.4σ from the well-known 679.85 ± 0.04 day orbital period of Algol C. From our $O - C$ data alone, we cannot determine the exact number of companions in Algol's hierarchical system or the stability of this system.

From the shorter 226.2 yr subsample, we detect these same five above-mentioned strictly periodic signals. They give an excellent prediction for the last 9.2 yr of our $O - C$ data (Figure 2(b)). Although it is impossible to detect the longest 219 yr period from our shortest analyzed subsample of 185 yr, we can still predict the $O - C$ data turning-point epoch in the year 1995 (Figure 3(b)). This unexpected turning-point event could explain the odd publication gap in the otherwise continuous modern $O - C$ data of Algol.

We detect the linear $O - C$ trend, which confirms that Algol's orbital period has not changed since it was discovered by Goodricke (1783). The orbital planes of Algol C and the new other wide-orbit star candidates are probably coplanar because Algol's eclipses were observed already in ancient Egypt (Jetsu et al. 2013; Jetsu & Porceddu 2015; Porceddu et al. 2018).

In the bigger picture, the predictions for complex nonlinear models rarely succeed. We give a prediction for the next decade of Algol's $O - C$ changes after 2018 October 18 (Figure 1(b)). These future $O - C$ changes may prove that the abstract DCM approach works for complex nonlinear models and that Algol's data merely allowed us to check this.

We thank Dr. Chun-Hwey Kim for sending us the TIDAK database $O - C$ data of Algol. We also thank Dr. Sara Beck, Dr. Lindsay Ward, Dr. Gerard Samolyk, Dr. Stella Kafka, and Dr. Nancy Morrison, who helped us in finding the $O - C$ data of Algol from the Lichtenknecker Database of the BAV. This work has made use of NASA's Astrophysics Data System (ADS) services and the data from the European Space Agency (ESA) mission Gaia. We thank Linux Specialist Markus Minkkinen and Dr. Sebastian Porceddu from the Center for Information Technology (University of Helsinki). Their computer support during the Covid-19 pandemic crisis enabled us to complete this work.

Appendix
DCM Analysis of Simulated $O - C$ Data

We describe Figures A1–A3 and Tables A1–A3 in the beginning of this Appendix, and Figures A4–A15 and Tables A4–A15 in the main text. If the third-body orbit is circular ($e = 0$), the suitable DCM model order is $K_2 = 1$, because the $O - C$ curve is a pure sinusoid (Equation (13): $e = 0$). If the third-body orbit is not circular ($e > 0$), the $O - C$ curve is not a pure sinusoid. In this case, the suitable DCM model order for these eccentric orbits is $K_2 = 2$ (Hoffman et al. 2006). Our notations for circular ($e = 0$) and eccentric ($e > 0$) orbit $O - C$ curves are

$$(O - C)_{e=0} \tag{A1}$$

$$(O - C)_{e>0}. \tag{A2}$$

These $(O - C)_{e>0}$ and $(O - C)_{e=0}$ curves have the same peak-to-peak amplitude A for any p, t_p, e, and ω combination (Equations (13)–(17)). Our notation for their difference curve is

$$(O - C)_{\rm diff} = (O - C)_{e>0} - (O - C)_{e=0} \tag{A3}$$

having a peak to peak amplitude $A_{\rm diff}$. The amplitude ratio is

$$\Delta A = A_{\rm diff}/A. \tag{A4}$$

We also determine the phase differences

$$\Delta\phi_{\rm min} = (t_{\rm 2nd.min} - t_{\rm 1st.min})/p \tag{A5}$$

$$\Delta\phi_{\rm max} = (t_{\rm 2nd.max} - t_{\rm 1st.max})/p, \tag{A6}$$

of two first minimum ($t_{\rm 1st.min}$, $t_{\rm 2nd.min}$) and maximum ($t_{\rm 1st.max}$, $t_{\rm 2nd.max}$) epochs of the $(O - C)_{\rm diff}$ curve.

We simulate three cases of artificial $O - C$ data (Table A1: Cases I, II, and III). The simulated $O - C$ values are computed for the real data time points t_i from Table A4 ($n = 2224$). We add $0\overset{\rm d}{.}005$ Gaussian random errors to these simulated $O - C$ values. A DCM period search for these simulated $O - C$ data is performed between 8000 and 80,000 days. We also use the same period interval in our DCM analysis of real data (Sections 5.1–5.4)

A.1. Case I: Simulated Eccentric Orbit Data

In this section, we use p, A, t_p, e, and ω values of Case I (Table A1). Our Figure A1 shows all 40 $(O - C)_{e>0}$ and $(O - C)_{e=0}$ curve pairs, as well as their $(O - C)_{\rm diff}$ difference curves. We study only cases with $e \leqslant 0.4$ because our $\nu(t)$ Fourier expansion (Equation (16)) does not give the exact quantitative $\nu(t)$ values for higher eccentricities. However, our $\nu(t)$ estimates are sufficient for illustrating how eccentric orbit $(O - C)_{e>0}$ curves deviate from purely sinusoidal circular orbit $(O - C)_{e=0}$ curves.

The ΔA, $\Delta\phi_{\rm min}$, and $\Delta\phi_{\rm max}$ values for 40 eccentric $(O - C)_{e>0}$ curves are given above each panel of Figure A1. When the eccentricity e increases, the amplitude ratio ΔA increases. At the same time, the $(O - C)_{\rm diff}$ curve symmetry decreases, because the $\Delta\phi_{\rm min}$ and $\Delta\phi_{\rm max}$ values deviate more from 0.5. Both of these effects confirm that when eccentricity increases, the $(O - C)_{e>0}$ curve deviates more from the pure $(O - C)_{e=0}$ sinusoid. One symmetry remains: adding 180° to ω reverses the $\Delta\phi_{\rm min}$ and $\Delta\phi_{\rm max}$ pair values.

A.1.1. Case I: Correct Model Analysis

In Case I, the correct one-signal DCM model for simulated data has an order $K_2 = 2 \equiv e > 0$ (model$_{1,2,0}$). The number of signals ($K_1 = 1$) and the signal order ($K_2 = 2$) are both correct. The results for the DCM search with this correct model are given in Table A2. This table has the same structure as Figure A1. For example, the results for combination $e = 0.05$ and $\omega = 0°$ are given in the upper-left corner of both Table A2 and Figure A1.

DCM always detects the correct period p, because the ratio P_1/p is close to unity for all 40 e and ω combinations. The amplitude ratio A_1/A is close to unity for lower eccentricities $e \leqslant 0.2$. This ratio decreases for higher eccentricities. Yet, even in these cases the amplitude ratio is $A_1/A \geqslant 0.95$. The inaccuracy of our $\nu(t)$ Fourier expansion (Equation (16)) may partly explain this A_1/A ratio decrease. DCM can certainly detect the correct simulated signal period $p = 45976^{\rm d}$ and amplitude $A = 0\overset{\rm d}{.}0994$. Our abbreviation for this correct p period detection is "Correct-p" effect.

For eccentricities close to $e = 0$, the $(O - C)_{\rm e>0}$ curves for $P_1 = p$ and $P_1 = 2p$ periods are nearly identical. We use the abbreviation "Dp" to highlight all P_1 values for lower eccentricities $e \leqslant 0.1$ (Table A2). In these cases, the spurious double-period $P_1 = 2p$ detection is possible, if the grid of tested frequencies is too sparse. The probability for detecting this spurious $P_1 = 2p$ period would of course decrease if our chosen simulated data error $0\overset{\rm d}{.}005$ were smaller. We call this spurious $2p$ period detection "Double-p" effect.

A.1.2. Case I: Wrong Model Analysis

Here, we analyze again the same one-signal simulated eccentric orbit $(O - C)_{e>0}$ data of Case I, but our two-signal DCM model$_{2,1,0}$ is wrong. The number of signals ($K_1 = 2$) and the signal order ($K_2 = 1$) are both wrong. In other words, we make the false assumption that the one-signal eccentric orbit

Table A1
Cases I, II, and III

	Col. 1 (days)	Col. 2 (days)	Col. 3 (HJD)	Col. 4 Dimensionless	Col. 5 (°)	Col. 6 Figure	Col. 7 Table
Case I	$p = 45{,}976$	$A = 0.0994$	$t_p = 2373019.94$	$e = 0.05, 0.10, 0.20, 0.30$ or 0.40	$\omega = 0, 45, 90, 135, 180, 225, 270$ or 315	A1	A2, A3
Case II	$p_1 = 12{,}295$ $p_2 = 46{,}159$	$A_1 = 0.0174$ $A_2 = 0.1024$	$t_{p1} = 2375140.04$ $t_{p2} = 2372653.76$	$e_1 = 0$ $e_2 = 0$	$\omega_1 = 0$ $\omega_2 = 0$	A2	⋯
Case III	$p_1 = 12{,}304$ $p_2 = 25{,}274$	$A_1 = 0.0187$ $A_2 = 0.020$	$t_{p1} = 2374760.75$ $t_{p2} = 2380427.13$	$e_1 = 0$ $e_2 = 0$	$\omega_1 = 0$ $\omega_2 = 0$	A3	⋯

Note. Cols. 1–5 give the $O - C$ curve period (p), peak-to-peak amplitude (A), pericenter epoch (t_p), eccentricity (e), and periastron longitude (ω) (Equations (13)–(17)). Cols. 6–7 give the connected figures and tables.

Table A2
Case I: Correct Model Results

		$\omega = 0°$	$\omega = 45°$	$\omega = 90°$	$\omega = 135°$	$\omega = 180°$	$\omega = 225°$	$\omega = 270°$	$\omega = 315°$
$e = 0.05$	P_1	45978 Dp	45933 Dp	45996 Dp	45968 Dp	46082 Dp	45946 Dp	45976 Dp	46001 Dp
	A_1	0.0995	0.0995	0.0996	0.0990	0.0990	0.0998	0.0993	0.0995
	P_1/p	1.00	1.00	1.00	1.00	1.00	1.00	1.00	1.00
	A_1/A	1.00	1.00	1.00	1.00	1.00	1.00	1.00	1.00
$e = 0.10$	P_1	46016 Dp	45952 Dp	45874 Dp	45920 Dp	45997 Dp	45921 Dp	45943 Dp	45981 Dp
	A_1	0.0996	0.0995	0.0990	0.0986	0.0990	0.0994	0.0990	0.0991
	P_1/p	1.00	1.00	1.00	1.00	1.00	1.00	1.00	1.00
	A_1/A	1.00	1.00	1.00	0.99	1.00	1.00	1.00	1.00
$e = 0.20$	P_1	46004	46057	46058	45990	46020	46038	46093	45970
	A_1	0.0990	0.0984	0.0977	0.0985	0.0987	0.0983	0.0976	0.0984
	P_1/p	1.00	1.00	1.00	1.00	1.00	1.00	1.00	1.00
	A_1/A	1.00	0.99	0.98	0.99	0.99	0.99	0.98	0.99
$e = 0.30$	P_1	46074	46056	46004	45937	45980	46053	45959	46001
	A_1	0.0977	0.0964	0.0964	0.0975	0.0978	0.0968	0.0960	0.0981
	P_1/p	1.00	1.00	1.00	1.00	1.00	1.00	1.00	1.00
	A_1/A	0.98	0.97	0.97	0.98	0.98	0.97	0.96	0.99
$e = 0.40$	P_1	46084	46251	45930	45934	46079	46292	45929	45882
	A_1	0.0954	0.0939	0.0930	0.0960	0.0948	0.0932	0.0935	0.0960
	P_1/p	1.00	1.00	1.00	1.00	1.00	1.01	1.00	1.00
	A_1/A	0.96	0.94	0.94	0.96	0.95	0.94	0.94	0.96

Note. Simulated $(O - C)_{e>0}$ data signal period is $p = 45{,}976^{\rm d}$. Signal peak-to-peak amplitude is $A = 0\overset{\rm d}{.}0994$. For different e and ω combinations, the one-signal DCM model$_{1,2,0}$ search detects periods P_1 and peak-to-peak amplitudes A_1. The abbreviation "Dp" denotes Double-p effect cases, where spurious period $P_1 \sim 2p$ may be detected if the tested frequency grid is too sparse.

$(O - C)_{e>0}$ curve is a sum of two circular orbit $(O - C)_{e=0}$ curves. The results for this wrong model analysis are given in Table A3. Note that this table also has the same structure as Table A2 and Figure A1.

The correct period $P_2 = p$ is always detected because the P_2/p ratio is very close to unity for all 40 e and ω combinations. The period of the weaker detected signal is always $P_1 \approx P_2/2 \approx p/2$. Furthermore, the accuracy of this approximation increases when e increases! Both of the p and $p/2$ periods are certainly detected at larger eccentricities $e \geqslant 0.2$. The A_2/A_1 amplitude ratio of these p and $p/2$ signals decreases for higher eccentricities. This happens at the expense of the P_2 signal, because A_2/A decreases by about 10% when eccentricity increases from $e = 0.05$ and 0.40. All these effects are also illustrated in Figure A1.

For nearly circular orbits $e \leqslant 0.10$, the A_2/A_1 signal amplitude ratio is between 19 and 47. We use the abbreviation "Hp" to highlight the cases where the detection of weaker spurious $p/2$ period signal requires a denser tested frequency grid (Table A2). Our abbreviation for this spurious $p/2$ period detection is "Half-p" effect.

Some ω values can eliminate the symmetry of the $(O - C)_{e>0}$ curve even at these low $e \leqslant 0.10$ eccentricities, like the $e = 0.10$ and $\omega = 45°$ combination $(O - C)_{e>0}$ curve that shows no "Hp" effect.

It is important to realize that every real eccentric orbit $(O - C)_{e>0}$ curve can be presented as a sum of a purely sinusoidal circular orbit $(O - C)_{e=0}$ curve and a nearly sinusoidal $(O - C)_{\rm diff}$ curve. The respective periods of these curves are p, p, and $\sim p/2$. All three curves are "in phase," and

Table A3
Case I: Wrong Model Results

		$\omega = 0°$	$\omega = 45°$	$\omega = 90°$	$\omega = 135°$	$\omega = 180°$	$\omega = 225°$	$\omega = 270°$	$\omega = 315°$
$e = 0.05$	P_1	24823 Hp	23076 Hp	24924 Hp	24927 Hp	24793 Hp	23813 Hp	24554 Hp	24867 Hp
	A_1	0.0021	0.0025	0.0026	0.0021	0.0024	0.0024	0.0028	0.0021
	P_2	46032	46032	46018	45973	46003	46072	46055	45982
	A_2	0.0990	0.0994	0.0994	0.0991	0.0995	0.0990	0.0995	0.0994
	P_2/P_1	1.85	1.99	1.85	1.84	1.85	1.93	1.88	1.85
	A_2/A_1	47.1	39.8	38.2	47.2	41.4	41.2	35.5	47.3
	P_2/p	1.00	1.00	1.00	1.00	1.00	1.00	1.00	1.00
	A_2/A	1.00	1.00	1.00	1.00	1.00	1.00	1.00	1.00
$e = 0.10$	P_1	24993 Hp	22788	23172	24840 Hp	25051 Hp	23170	24418 Hp	24900 Hp
	A_1	0.0044	0.0052	0.0048	0.0044	0.0044	0.0052	0.0051	0.0045
	P_2	46043	45996	45937	45998	46032	46025	46121	45993
	A_2	0.0988	0.0992	0.0992	0.0986	0.0993	0.0987	0.0987	0.0988
	P_2/P_1	1.84	2.02	1.98	1.85	1.84	1.99	1.89	1.85
	A_2/A_1	22.4	19.1	20.7	24.2	22.6	19.0	19.4	22.0
	P_2/p	1.00	1.00	1.00	1.00	1.00	1.00	1.00	1.00
	A_2/A	0.99	1.00	1.00	0.99	1.00	0.99	0.99	0.99
$e = 0.20$	P_1	23010	23029	22848	22899	23024	23044	22863	22879
	A_1	0.0098	0.0089	0.0092	0.0095	0.0096	0.0096	0.0097	0.0094
	P_2	45953	46029	45973	45955	46000	46074	45941	45962
	A_2	0.0974	0.0975	0.0981	0.0974	0.0973	0.0974	0.0978	0.0973
	P_2/P_1	2.00	2.00	2.01	2.01	2.00	2.00	2.01	2.01
	A_2/A_1	9.9	11.0	10.7	10.2	10.1	10.1	10.1	10.4
	P_2/p	1.00	1.00	1.00	1.00	1.00	1.00	1.00	1.00
	A_2/A	0.98	0.98	0.99	0.98	0.98	0.98	0.98	0.98
$e = 0.30$	P_1	22977	23116	22833	22996	23098	23048	22806	23085
	A_1	0.0135	0.0135	0.0139	0.0139	0.0135	0.0134	0.0140	0.0141
	P_2	46069	46073	45987	46018	46060	46030	45942	45976
	A_2	0.0940	0.0944	0.0962	0.0949	0.0940	0.0947	0.0961	0.0949
	P_2/P_1	2.00	1.99	2.01	2.00	1.99	2.00	2.01	1.99
	A_2/A_1	7.0	7.0	6.9	6.8	7.0	7.1	6.9	6.7
	P_2/p	1.00	1.00	1.00	1.00	1.00	1.00	1.00	1.00
	A_2/A	0.94	0.95	0.97	0.95	0.94	0.95	0.97	0.95
$e = 0.40$	P_1	22998	23119	22916	22899	23068	23210	22909	22976
	A_1	0.0166	0.0166	0.0167	0.0178	0.0165	0.0164	0.0170	0.0174
	P_2	45997	46089	45978	45961	46054	46267	45983	45917
	A_2	0.0901	0.0909	0.0938	0.0922	0.0898	0.0904	0.0934	0.0920
	P_2/P_1	2.00	1.99	2.01	2.01	2.00	1.99	2.01	2.00
	A_2/A_1	5.4	5.5	5.6	5.2	5.4	5.5	5.5	5.3
	P_2/p	1.00	1.00	1.00	1.00	1.00	1.01	1.00	1.00
	A_2/A	0.91	0.91	0.94	0.93	0.90	0.91	0.94	0.92

Note. Simulated $(O-C)_{\mathrm{e}>0}$ signal period is $p = 45{,}976^{\mathrm{d}}$. Signal peak-to-peak amplitude is $A = 0\overset{\mathrm{d}}{.}0994$. For different e and ω combinations, the two-signal DCM model$_{2,1,0}$ search detects signals having periods P_1 and P_2, and peak-to-peak amplitudes A_1 and A_2. The abbreviation "Hp" highlights the Half-p effect cases, where the detection of a weaker $P_1 \sim p/2$ signal requires a denser tested frequency grid.

Table A4
$O - C$ Data

t (days)	y (days)	σ_y (days)
2372238.35100	−0.17216	0.00010
2372284.23700	−0.16303	0.00010
2372301.39700	−0.20686	0.00010

Note. Only the first three of all $n = 2224$ values are shown. The arbitrary $0\overset{\mathrm{d}}{.}00010$ errors give the correct format for our data file (file1), because dcm.py requires that the third column of file1 contains some numerical values for the errors. Because these errors are unknown, we use equal weights for all observations, and the numerical values of these errors are irrelevant (see the appendix of Paper I: TestStat ≠ 1).

therefore the eccentric orbit $(O-C)_{\mathrm{e}>0}$ sum curve has only one minimum and one maximum.

A.2. Case II: Correct Model Analysis

In Case II, the simulated data contains a sum of two sinusoidal circular orbit $(O-C)_{e=0}$ signals having periods $p_1 = 12{,}295^{\mathrm{d}}$ and $p_2 = 46{,}159^{\mathrm{d}}$ (Figure A2). The other parameters can be found in Table A1 (Case II). The higher-amplitude p_2 signal dominates over the lower-amplitude p_1 signal. These red and blue $(O-C)_{e=0}$ curves, and their black $(O-C)_{1+2}$ interference curve, are shown in Figure A2.

In Case II, the correct circular orbit model is DCM model$_{2,1,0}$. This model has the correct number of signals $(K_1 = 2)$ and the correct order $(K_2 = 1)$. DCM detects the

Table A5
Samples

Sample	n $\cdots$	t_1 (HJD)	t_n (HJD)	ΔT (days)	 (yr)	file1
All data	2224	2372238.351	2458409.7612	86,171.4102	235.9	1hjdAlgol.dat
First 226^{y} -data	2174	2372238.351	2454839.9189	82,601.5679	226.2	2hjdAlgol.dat
Last 9^{y} data	50	2455063.566	2458409.7612	3346.1952	9.2	$\cdots$
First 185^{y} data	1731	2372238.351	2439918.358	67,680.007	185.3	3hjdAlgol.dat
Last 50^{y} data	493	2440144.8771	2458409.7612	18,264.8841	50.0	$\cdots$

Note. Number of observations (n), first observing time (t_1), last observing time (t_n), time span (ΔT), and data file (file1).

correct simulated $P_1 = 12286^{\text{d}} \pm 18^{\text{d}}$ and $P_2 = 46122^{\text{d}} \pm 57^{\text{d}}$ signal periods, as well as the correct amplitudes $A_1 = 0\overset{\text{d}}{.}0170 \pm 0\overset{\text{d}}{.}0004$ and $A_2 = 0\overset{\text{d}}{.}1019 \pm 0\overset{\text{d}}{.}0003$. In short, DCM succeeds in detecting both simulated circular orbit $(O-C)_{\text{e}=0}$ signals.

A.3. Case II: Wrong Model Analysis

Here, we analyze Case II simulated data using the wrong eccentric orbit one-signal DCM model$_{1,2,0}$. Both the number of signals ($K_1 = 1$) and the model order ($K_2 = 2$) are wrong. We detect the $P_1 = 46{,}400^{\text{d}} \pm 81^{\text{d}}$ period signal having a peak-to-peak amplitude $A_1 = 0\overset{\text{d}}{.}1015 \pm 0\overset{\text{d}}{.}0005$. Because the $p_2 = 46{,}159^{\text{d}}$ period of the stronger signal dominates in the black $(O-C)_{1+2}$ interference curve of Figure A2, this detected P_1 period is close to, but slightly larger than, the p_2 period. Our DCM search result for P_1 is confirmed by the distance between the black $(O-C)_{1+2}$ interference curve minima, which is indeed longer than the distance between the dominating blue $(O-C)_2$ curve minima (Figure A2).

A.4. Case III: Correct Model Analysis

In Case III, the simulated sinusoidal $(O-C)_{\text{e}=0}$ signal periods are $p_1 = 12{,}304^{\text{d}}$ and $p_2 = 25{,}274^{\text{d}}$ (Figure A3). The signal amplitudes are nearly equal (Table A1: Case II). The correct model for these simulated data is the DCM model$_{2,1,0}$, which searches for the sum of two circular orbit $(O-C)_{\text{e}=0}$ curves ($K_1 = 2$, $K_2 = 1$). DCM detects the correct $P_1 = 12{,}322^{\text{d}} \pm 20^{\text{d}}$ and $P_2 = 25{,}259^{\text{d}} \pm 89^{\text{d}}$ signals, as well as the correct amplitudes $A_1 = 0\overset{\text{d}}{.}0190 \pm 0\overset{\text{d}}{.}0004$ and $A_2 = 0\overset{\text{d}}{.}020 \pm 0\overset{\text{d}}{.}0003$. Again, DCM succeeds in detecting both simulated circular orbit $(O-C)_{\text{e}=0}$ signals.

A.5. Case III: Wrong Model Analysis

Finally, the same simulated Case III data are analyzed by using the wrong eccentric DCM model$_{1,2,0}$. In other words, we search for only one eccentric orbit $(O-C)_{\text{e}>0}$ signal when the data contains two circular orbit $(O-C)_{\text{e}=0}$ signals. DCM detects a signal having $P_1 = 24{,}771^{\text{d}} \pm 34^{\text{d}}$ and $A_1 = 0\overset{\text{d}}{.}0319 \pm 0\overset{\text{d}}{.}0005$. The simulated p_1 and p_2 signals' interference period is

$$p' = k(p_1^{-1} - p_2^{-1})^{-1}, \tag{A7}$$

where $k = \pm 1, \pm 2, \ldots$ is the phase difference during p'. In this particular case, $k = 1$ gives $p' = 23976^{\text{d}}$. This black double wave $(O-C)_{1+2}$ curve is shown in Figure A3. DCM detects this "correct" interference signal period p', which is repeated throughout the whole data. We call this spurious interference period p' detection "Interference-p'" effect.

The black p' interference $(O-C)_{1+2}$ curve shows two minima and two maxima because the red p_1 period and the blue p_2 period sinusoids are "off phase" (Figure A3). Therefore, this black $(O-C)_{1+2}$ curve cannot represent a real eccentric orbit $(O-C)_{\text{e}>0}$ curve.

Table A6

All Data Trend (Section 5.1.1): One-, Two-, and Three-signal ($K_1 = 1$, 2 and 3) Models ($\mathcal{M}$) Have Eccentric Third-body Orbits ($K_2 = 2 \equiv e > 0$)

Period Analysis: All Original Data = 1hjdAlgol.dat

$\mathcal{M}$	Model	$\mathcal{M} = 2$ model$_{1,2,1}$	$\mathcal{M} = 3$ model$_{1,2,2}$	$\mathcal{M} = 4$ model$_{1,2,3}$	$\mathcal{M} = 5$ model$_{2,2,0}$	$\mathcal{M} = 6$ model$_{2,2,1}$	$\mathcal{M} = 7$ model$_{2,2,2}$	$\mathcal{M} = 8$ model$_{2,2,3}$	$\mathcal{M} = 9$ model$_{3,2,0}$	$\mathcal{M} = 10$ model$_{3,2,1}$	$\mathcal{M} = 11$ model$_{3,2,2}$	$\mathcal{M} = 12$ model$_{3,2,3}$	dcm.dat
1	model$_{1,2,0}$	↑	↑	↑	↑	↑	↑	↑	↑	↑	↑	↑	1hjd13R120S.dat
	$\eta = 6$	$F = 2821$	$F = 1542$	$F = 1154$	$F = 684$	$F = 815$	$F = 702$	$F = 623$	$F = 498$	$F = 503$	$F = 461$	$F = 427$	
	$R = 1.0678$	$Q_F < 10^{-16}$	$Q_F < 10^{-16}$	$Q_F < 10^{-16}$	$Q_F < 10^{-16}$	$Q_F < 10^{-16}$	$Q_F < 10^{-16}$	$Q_F < 10^{-16}$	$Q_F < 10^{-16}$	$Q_F < 10^{-16}$	$Q_F < 10^{-16}$	$Q_F < 10^{-16}$	
2	model$_{1,2,1}$	–	↑	↑	↑	↑	↑	↑	↑	↑	↑	↑	1hjd13R121S.dat
	$\eta = 7$	–	$F = 116$	$F = 142$	$F = 67$	$F = 183$	$F = 154$	$F = 137$	$F = 106$	$F = 120$	$F = 109$	$F = 101$	
Lp	$R = 0.4698$	–	$Q_F < 10^{-16}$	$Q_F < 10^{-16}$	$Q_F < 10^{-16}$	$Q_F < 10^{-16}$	$Q_F < 10^{-16}$	$Q_F < 10^{-16}$	$Q_F < 10^{-16}$	$Q_F < 10^{-16}$	$Q_F < 10^{-16}$	$Q_F < 10^{-16}$	
3	model$_{1,2,2}$	–	–	↑	↑	↑	↑	↑	↑	↑	↑	↑	1hjd13R122S.dat
Um	$\eta = 8$	–	–	$F = 161$	$F = 34$	$F = 190$	$F = 154$	$F = 134$	$F = 100$	$F = 115$	$F = 103$	$F = 95$	
Ad, Lp	$R = 0.4468$	–	–	$Q_F < 10^{-16}$	$Q_F < 10^{-16}$	$Q_F < 10^{-16}$	$Q_F < 10^{-16}$	$Q_F < 10^{-16}$	$Q_F < 10^{-16}$	$Q_F < 10^{-16}$	$Q_F < 10^{-16}$	$Q_F < 10^{-16}$	
4	model$_{1,2,3}$	–	–	–	←	↑	↑	↑	↑	↑	↑	↑	1hjd13R123S.dat
	$\eta = 9$	–	–	–	$F = -7.4$	$F = 186$	$F = 142$	$F = 119$	$F = 85$	$F = 102$	$F = 90$	$F = 82$	
	$R = 0.4165$	–	–	–	$Q_F = 1$	$Q_F < 10^{-16}$	$Q_F < 10^{-16}$	$Q_F < 10^{-16}$	$Q_F < 10^{-16}$	$Q_F < 10^{-16}$	$Q_F < 10^{-16}$	$Q_F < 10^{-16}$	
5	model$_{2,2,0}$	–	–	–	–	↑	↑	↑	↑	↑	↑	↑	1hjd13R220S.dat
Um	$\eta = 11$	–	–	–	–	$F = 629$	$F = 319$	$F = 222$	$F = 134$	$F = 148$	$F = 127$	$F = 112$	
Ad	$R = 0.4270$	–	–	–	–	$Q_F < 10^{-16}$	$Q_F < 10^{-16}$	$Q_F < 10^{-16}$	$Q_F < 10^{-16}$	$Q_F < 10^{-16}$	$Q_F < 10^{-16}$	$Q_F < 10^{-16}$	
6	model$_{2,2,1}$	–	–	–	–	–	←	↑	↑	↑	↑	↑	1hjd13R221S.dat
	$\eta = 12$	–	–	–	–	–	$F = 7.3$	$F = 15$	$F = 7.7$	$F = 41$	$F = 34$	$F = 30$	
	$R = 0.3324$	–	–	–	–		$Q_F = 0.0068$	$Q_F = 2.9 \times 10^{-7}$	$Q_F = 3.4 \times 10^{-6}$	$Q_F < 10^{-16}$	$Q_F < 10^{-16}$	$Q_F < 10^{-16}$	
7	model$_{2,2,2}$	–	–	–	–	–	–	↑	↑	↑	↑	↑	1hjd13R222S.dat
	$\eta = 13$	–	–	–	–	–	–	$F = 23$	$F = 7.8$	$F = 49$	$F = 39$	$F = 34$	
Lp	$R = 0.3313$	–	–	–	–	–		$Q_F = 1.8 \times 10^{-6}$	$Q_F = 3.3 \times 10^{-5}$	$Q_F < 10^{-16}$	$Q_F < 10^{-16}$	$Q_F < 10^{-16}$	
8	model$_{2,2,3}$	–	–	–	–	–	–	–	←	↑	↑	↑	1hjd13R223S.dat
Um	$\eta = 14$	–	–	–	–	–	–	–	$F = 0.34$	$F = 57$	$F = 43$	$F = 36$	
Ad	$R = 0.3279$	–	–	–	–	–	–	–	$Q_F = 0.71$	$Q_F < 10^{-16}$	$Q_F < 10^{-16}$	$Q_F < 10^{-16}$	
9	model$_{3,2,0}$	–	–	–	–	–	–	–	–	↑	↑	↑	1hjd13R320S.dat
Um	$\eta = 16$	–	–	–	–	–	–	–	–	$F = 170$	$F = 86$	$F = 59$	
Ad, If	$R = 0.3277$	–	–	–	–	–	–	–	–	$Q_F < 10^{-16}$	$Q_F < 10^{-16}$	$Q_F < 10^{-16}$	
10	model$_{3,2,1}$	–	–	–	–	–	–	–	–	–	←	←	1hjd13R321S.dat
	$\eta = 17$	–	–	–	–	–	–	–	–	–	$F = 0.72$	$F = 2.9$	
	$R = 0.3042$	–	–	–	–	–	–	–	–	–	$Q_F = 0.39$	$Q_F = 0.055$	
11	model$_{3,2,2}$	–	–	–	–	–	–	–	–	–	–	←	1hjd13R322S.dat

Table A6
(Continued)

Period Analysis: All Original Data = 1hjdAlgol.dat													
$\mathcal{M}$	Model	$\mathcal{M} = 2$ model$_{1,2,1}$	$\mathcal{M} = 3$ model$_{1,2,2}$	$\mathcal{M} = 4$ model$_{1,2,3}$	$\mathcal{M} = 5$ model$_{2,2,0}$	$\mathcal{M} = 6$ model$_{2,2,1}$	$\mathcal{M} = 7$ model$_{2,2,2}$	$\mathcal{M} = 8$ model$_{2,2,3}$	$\mathcal{M} = 9$ model$_{3,2,0}$	$\mathcal{M} = 10$ model$_{3,2,1}$	$\mathcal{M} = 11$ model$_{3,2,2}$	$\mathcal{M} = 12$ model$_{3,2,3}$	dcm.dat
	$\eta = 18$	–	–	–	–	–	–	–	–	–	–	$F = 5.1$	
	$R = 0.3041$	–	–	–	–	–	–	–	–	–	–	$Q_F = 0.024$	
12	model$_{3,2,3}$	–	–	–	–	–	–	–	–	–	–	–	1hjd13R323S.dat
	$\eta = 19$	–	–	–	–	–	–	–	–	–	–	–	
	$R = 0.3034$	–	–	–	–	–	–	–	–	–	–	–	

Note. Trend orders $K_3 = 0$, 1, 2, and 3 for $p(t)$ are compared. The Fisher test is used to compare DCM search results between 8000 and 80,000 days. Notations are " ↑ " ≡ complex model above is better than left-side simple model, and " ← " ≡ left-side simple model is better than the complex model above. Parameters are F = Fisher test statistic and Q_F = critical level. The control file is dcm.dat. Unstable models are denoted with "Um." They have dispersing amplitudes "Ad," or intersecting frequencies "If." Some models have leaking periods "Lp" larger than $\Delta T = 86{,}171^{\mathrm{d}}$. The best DCM model for all data is a linear trend $K_3 = 1$ order model$_{3,2,1}$.

Table A7

All Data Eccentric Orbits (Section 5.1.2)

Col. 1	Col. 2	Col. 3	Col. 4	Col. 5	Col. 6	Col. 7	Col. 8	Col. 9	Col. 10
		Search between 8000 and 80,000 days							
		Period Analysis: All Original Data = 1hjdAlgol.dat				Fisher Test			
$\mathcal{M}$	Model	P_1 and A_1(days)	P_2 and A_2(days)	P_3 and A_3(days)	P_4 and A_4(days)	model$_{2,2,1}$	model$_{3,2,1}$	model$_{4,2,1}$	dcm.dat
1	model$_{1,2,1}$	88183 ± 816 Lp	⋯	⋯	⋯	↑	↑	↑	1hjd14R121S.dat
	$\eta = 7$	0.313 ± 0.004	⋯	⋯	⋯	$F = 183$	$F = 120$	$F = 90$	
Lp	$R = 0.4698$					$Q_F < 10^{-16}$	$Q_F < 10^{-16}$	$Q_F < 10^{-16}$	
2	model$_{2,2,1}$	24984 ± 99	80087 ± 744	⋯	⋯	⋯	↑	↑	1hjd14R221S.dat
	$\eta = 12$	0.0316 ± 0.0008	0.288 ± 0.004	⋯	⋯	⋯	$F = 41$	$F = 31$	
	$R = 0.3324$					⋯	$Q_F < 10^{-16}$	$Q_F < 10^{-16}$	
3	model$_{3,2,1}$	20358 ± 128	24742 ± 142	79999 ± 1216	⋯	⋯	⋯	↑	1hjd14R321S.dat
	$\eta = 17$	0.013 ± 0.001	0.029 ± 0.001	0.287 ± 0.005	⋯	⋯	⋯	$F = 19$	
	$R = 0.3042$					⋯	⋯	$Q_F < 10^{-16}$	
4	model$_{4,2,1}$	14912 ± 165	20984 ± 232	26846 ± 250	55172 ± 528	⋯	⋯	⋯	1hjd14R421S.dat
Um	$\eta = 22$	0.020 ± 0.004	0.039 ± 0.003	0.4 ± 0.6 Ad	0.5 ± 0.6 Ad	⋯	⋯	⋯	
Ad	$R = 0.2913$					⋯	⋯	⋯	
		Search between 500 and 8000 days							
		Period analysis: Three-signal residuals = 1hjd14R321SResiduals.dat				Fisher Test			
$\mathcal{M}$	Model	P_1 and A_1(days)	P_2 and A_2(days)	P_3 and A_3(days)		model$_{2,2,0}$	model$_{3,2,0}$		dcm.dat
5	model$_{1,2,0}$	680.3 ± 0.4	⋯	⋯		↑	↑		1hjd58R120S.dat
	$\eta = 6$	0.0062 ± 0.0006	⋯	⋯		$F = 17$	$F = 12$		
	$R = 0.2950$					$Q_F < 10^{-16}$	$Q_F < 10^{-16}$		
6	model$_{2,2,0}$	680.4 ± 0.4	7290 ± 29	⋯		⋯	↑		1hjd58R220S.dat
	$\eta = 11$	0.0064 ± 0.0007	0.007 ± 0.001	⋯		⋯	$F = 6.3$		
	$R = 0.2840$			⋯		⋯	$Q_F = 8.1 \times 10^{-6}$		
7	model$_{3,2,0}$	680.1 ± 0.3	7124 ± 43	7698 ± 75 Sp		⋯	⋯		1hjd58R320S.dat
Um	$\eta = 16$	0.0065 ± 0.0009	0.0066 ± 0.0007	0.005 ± 0.001		⋯	⋯		
Sp	$R = 0.2800$					⋯	⋯		

Note. Col. 1: Model number $\mathcal{M}$. Col. 2: model$_{K_1,K_2,K_3}$, η= number of free parameters and R = sum of squared residuals. Cols. 3–6: period analysis results: detected periods P_1, ..., P_4 and amplitudes A_1, ..., A_4. Cols. 7–9: Fisher test results. Col. 10: control file is dcm.dat. Model $\mathcal{M} = 3 + 6$ is the best one for all data.

Table A8

All Data Circular Orbits (Section 5.1.3: First Alternative)

		Search between 8000 and 80,000 days							
		Period Analysis: All Original Data = 1hjdAlgol.dat				Fisher Test			
$\mathcal{M}$	Model	P_1 and A_1(days)	P_2 and A_2(days)	P_3 and A_3(days)	P_4 and A_4(days)	model$_{2,1,1}$	model$_{3,1,1}$	model$_{4,1,1}$	dcm.dat
1	model$_{1,1,1}$ $\eta = 5$ $R = 0.9998$	59474 ± 255 0.199 ± 0.001	⋯ ⋯	⋯ ⋯	⋯ ⋯	↑ $F = 863$ $Q_F < 10^{-16}$	↑ $F = 598$ $Q_F < 10^{-16}$	↑ $F = 503$ $Q_F < 10^{-16}$	1hjd14R111S.dat
2 Um Ad, Lp	model$_{2,1,1}$ $\eta = 8$ $R = 0.4610$	45204 ± 350 0.091 ± 0.003	145483 ± 13700 Lp 0.8 ± 0.2 Ad	⋯ ⋯	⋯ ⋯	⋯ ⋯ ⋯	↑ $F = 154$ $Q_F < 10^{-16}$	↑ $F = 149$ $Q_F < 10^{-16}$	1hjd14R211S.dat
3 Um Ad,Lp	model$_{3,1,1}$ $\eta = 11$ $R = 0.3814$	12338 ± 55 0.0177 ± 0.0006	45423 ± 424 0.094 ± 0.004	145456 ± 15326 Lp 0.8 ± 0.2 Ad	⋯ ⋯	⋯ ⋯ ⋯	⋯ ⋯ ⋯	↑ $F = 120$ $Q_F < 10^{-16}$	1hjd14R311S.dat
4 Um Ad,Lp	model$_{4,1,1}$ $\eta = 14$ $R = 0.3280$	12352 ± 58 0.0188 ± 0.0006	24773 ± 562 0.018 ± 0.001	42610 ± 556 0.088 ± 0.004	145456 ± 16180 Lp 0.9 ± 0.2 Ad	⋯ ⋯ ⋯	⋯ ⋯ ⋯	⋯ ⋯ ⋯	1hjd14R411S.dat
		Search between 8000 and 80,000 days							
		Period analysis: Four-signal residuals = 1hjd14R411SResiduals.dat				Fisher Test			
$\mathcal{M}$	Model	P_1 and A_1(days)	P_2 and A_2(days)			model$_{2,1,0}$			dcm.dat
5	model$_{1,1,0}$ $\eta = 4$ $R = 0.3072$	10175 ± 83 0.0087 ± 0.0005	⋯ ⋯			← $F = 2.6$ $Q_F = 0.047$			1hjd56R110S.dat
6 Um If	model$_{2,1,0}$ $\eta = 7$ $R = 0.3061$	9248 ± 302 If 0.021 ± 0.002	10175 ± 160 If 0.009 ± 0.002			⋯ ⋯ ⋯			1hjd56R210S.dat
		Search between 500 and 8000 days							
		Period analysis: Five-signal residuals = 1hjd56R110SResiduals.dat				Fisher Test			
$\mathcal{M}$	Model	P_1 and A_1(days)	P_2 and A_2(days)	P_3 and A_3(days)		model$_{2,1,0}$	model$_{3,1,0}$	model$_{4,1,0}$	dcm.dat
7	model$_{1,1,0}$ $\eta = 4$ $R = 0.2984$	680.5 ± 0.6 0.0056 ± 0.0006	⋯ ⋯	⋯ ⋯		↑ $F = 22$ $Q_F = 3.8 \times 10^{-14}$	↑ $F = 14$ $Q_F = 2.2 \times 10^{-16}$	↑ $F = 11$ $Q_F < 10^{-16}$	1hjd710R110S.dat
8	model$_{2,1,0}$ $\eta = 7$ $R = 0.2897$	680.7 ± 0.3 0.0057 ± 0.0008	7354 ± 61 0.0056 ± 0.0008	⋯ ⋯		⋯ ⋯ ⋯	↑ $F = 6.9$ $Q_F = 0.00012$	↑ $F = 5.9$ $Q_F = 3.6 \times 10^{-6}$	1hjd710R210S.dat
9	model$_{3,1,0}$ $\eta = 10$ $R = 0.2870$	680.7 ± 0.4 0.0057 ± 0.0006	2986 ± 39 0.0031 ± 0.0008	7360 ± 55 0.0056 ± 0.0006	⋯ ⋯	⋯ ⋯ ⋯	⋯ ⋯ ⋯	← $F = 4.9$ $Q_F = 0.0021$	1hjd710R310S.dat
10	model$_{4,1,0}$ $\eta = 13$ $R = 0.2851$	680.5 ± 0.5 0.0057 ± 0.0006	3560 ± 21 0.0031 ± 0.0006	6964 ± 113 0.0036 ± 0.0009	7449 ± 58 0.0056 ± 0.0009	⋯ ⋯ ⋯	⋯ ⋯ ⋯	⋯ ⋯ ⋯	1hjd710R410S.dat

Note. Otherwise as in Table A7.

Table A9

All Data Circular Orbits (Section 5.1.3: Second Alternative)

		Search between 8000 and 80,000 days								
		Period analysis: All original data = 1hjdAlgol.dat						Fisher Test		
$\mathcal{M}$	Model	P_1 and A_1(days)	P_2 and A_2(days)	P_3 and A_3(days)	P_4 and A_4(days)	P_5 and A_5(days)	P_6 and A_6(days)	model$_{5,1,1}$	model$_{6,1,1}$	dcm.dat
1	model$_{4,1,1}$	12377 ± 50	24633 ± 578	42318 ± 240	120817 ± 31482 Lp	⋯	⋯	↑	↑	1hjd16R411S.dat
Um	$\eta = 14$	0.0188 ± 0.0008	0.018 ± 0.004	0.085 ± 0.004	0.6 ± 0.7 Ad	⋯	⋯	$F = 57$	$F = 31$	
Ad, Lp	$R = 0.3284$					⋯	⋯	$Q_F < 10^{-16}$	$Q_F < 10^{-16}$	
2	model$_{5,1,1}$	10144 ± 30	12294 ± 109	24247 ± 872	42422 ± 640	120740 ± 41002 Lp	⋯		←	1hjd16R511S.dat
Um	$\eta = 17$	0.0097 ± 0.0004	0.018 ± 0.001	0.018 ± 0.002	0.08 ± 0.01	0.6 ± 0.5 Ad	⋯		$F = 4.6$	
Ad, Lp	$R = 0.3047$						⋯		$Q_F = 0.0032$	
3	model$_{6,1,1}$	10778 ± 256 If	11219 ± 206 If	11368 ± 182 If	23475 ± 625	42617 ± 267	96213 ± 20664 Lp		⋯	1hjd16R611S.dat
Um	$\eta = 20$	0.08 ± 0.02 Ad	0.3 ± 0.1 Ad	0.28 ± 0.08 Ad	0.016 ± 0.001	0.078 ± 0.006	0.4 ± 0.2 Ad		⋯	
If, Ad, Lp	$R = 0.3015$						⋯		⋯	

		Search between 500 and 8000 days					
		Period analysis: Five-signal residuals = 1hjd16R511SResiduals.dat			Fisher Test		
$\mathcal{M}$	Model	P_1 and A_1(days)	P_2 and A_2(days)	P_3 and A_3(days)	model$_{2,1,0}$	model$_{3,1,0}$	dcm.dat
4	model$_{1,1,0}$	680.6 ± 0.4	⋯	⋯	↑	↑	1hjd710R110L.dat
	$\eta = 4$	0.0055 ± 0.0008	⋯	⋯	$F = 26$	$F16$	
	$R = 0.2962$				$Q_F < 10^{-16}$	$Q_F < 10^{-16}$	
5	model$_{2,1,0}$	680.7 ± 0.5	7395 ± 37	⋯	⋯	↑	1hjd710R210L.dat
	$\eta = 7$	0.0057 ± 0.0009	0.0061 ± 0.0006	⋯	⋯	$F = 6.2$	
	$R = 0.2861$				⋯	$Q_F = 0.00032$	
6	model$_{3,1,0}$	680.5 ± 0.5	7034 ± 148 If, Sp	7478 ± 82 If	⋯	⋯	1hjd710R310L.dat
Um	$\eta = 10$	0.0056 ± 0.0008	0.003 ± 0.001	0.006 ± 0.001	⋯	⋯	
If, Sp	$R = 0.2837$				⋯	⋯	

Note. Otherwise as in Table A7.

Table A10

First 226^{y} Data Eccentric Orbits (Section 5.2)

Col. 1	Col. 2	Col. 3	Col. 4	Col. 5	Col. 6	Col. 7	Col. 8	Col. 9	Col. 10
		Search between 8000 and 80,000 days							
		Period analysis: All original data=2hjdAlgol.dat				Fisher Test			
$\mathcal{M}$	Model	P_1 and A_1(days)	P_2 and A_2(days)	P_3 and A_3(days)	P_4 and A_4(days)	model$_{2,2,1}$	model$_{3,2,1}$	model$_{4,2,1}$	dcm.dat
1	model$_{1,2,1}$	92489 ± 1016 Lp	⋯	⋯	⋯	↑	↑	↑	2hjd14R121S.dat
	$\eta = 7$	0.320 ± 0.004	⋯	⋯	⋯	$F = 160$	$F = 104$	$F = 77$	
Lp	$R = 0.4443$					$Q_F < 10^{-16}$	$Q_F < 10^{-16}$	$Q_F < 10^{-16}$	
2	model$_{2,2,1}$	26623 ± 107	84215 ± 1466 Lp	⋯	⋯	⋯	↑	↑	2hjd14R221S.dat
	$\eta = 12$	0.028 ± 0.001	0.300 ± 0.005	⋯	⋯	⋯	$F = 35$	$F = 26$	
Lp	$R = 0.3243$					⋯	$Q_F < 10^{-16}$	$Q_F < 10^{-16}$	
3	model$_{3,2,1}$	20592 ± 172	24870 ± 190	78589 ± 2004	⋯	⋯	⋯	↑	2hjd14R321S.dat
	$\eta = 17$	0.014 ± 0.002	0.030 ± 0.008	0.282 ± 0.007	⋯	⋯	⋯	$F = 17$	
	$R = 0.3000$					⋯	⋯	$Q_F = 2.2 \times 10^{-16}$	
4	model$_{4,2,1}$	14911 ± 125	20739 ± 242	26644 ± 99	53512 ± 806	⋯	⋯	⋯	2hjd14R421S.dat
Um	$\eta = 22$	0.0206 ± 0.0004	0.0420 ± 0.0006	2.9 ± 1.6 Ad	3.0 ± 1.6 Ad	⋯	⋯	⋯	
Ad	$R = 0.2887$					⋯	⋯	⋯	
		Search between 500 and 8000 days							
		Period analysis: Three-signal residuals = 2hjd14R321SResiduals.dat				Fisher Test			
$\mathcal{M}$	Model	P_1 and A_1(days)	P_2 and A_2(days)	P_3 and A_3(days)		model$_{2,2,0}$	model$_{3,2,0}$		dcm.dat
5	model$_{1,2,0}$	680.1 ± 0.6	⋯	⋯		↑	↑		2hjd58R120S.dat
	$\eta = 6$	0.0061 ± 0.0006	⋯	⋯		$F = 15$	$F = 11$		
	$R = 0.2914$					$Q_F = 1.5 \times 10^{-14}$	$Q_F < 10^{-16}$		
6	model$_{2,2,0}$	680.3 ± 0.3	7287 ± 40	⋯		⋯	↑		2hjd58R220S.dat
	$\eta = 11$	0.0063 ± 0.0008	0.007 ± 0.001	⋯		⋯	$F = 6.2$		
	$R = 0.2816$			⋯		⋯	$Q_F = 9.8 \times 10^{-6}$		
7	model$_{3,2,0}$	679.9 ± 0.4	7080 ± 46	7757 ± 87 Sp		⋯	⋯		2hjd58R320S.dat
Um	$\eta = 16$	0.0066 ± 0.0006	0.006 ± 0.001	0.006 ± 0.001		⋯	⋯		
Sp	$R = 0.2775$					⋯	⋯		

Note. Otherwise as in Table A7.

Table A11

First 185^y Data Eccentric Orbits (Section 5.3)

Col. 1	Col. 2	Col. 3	Col. 4	Col. 5	Col. 6	Col. 7	Col. 8	Col. 9	Col. 10
		Search between 8000 and 80,000 days							
		Period analysis: All original data=3hjdAlgol.dat				Fisher Test			
$\mathcal{M}$	Model	P_1 and A_1(days)	P_2 and A_2(days)	P_3 and A_3(days)	P_4 and A_4(days)	$\text{model}_{2,2,1}$	$\text{model}_{3,2,1}$	$\text{model}_{4,2,1}$	dcm.dat
1	$\text{model}_{1,2,1}$	64454 ± 880	⋯	⋯	⋯	↑	↑	↑	3hjd14R121S.dat
	$\eta = 7$	0.258 ± 0.005	⋯	⋯	⋯	$F = 118$	$F = 69$	$F = 50$	
	$R = 0.3407$					$Q_F < 10^{-16}$	$Q_F < 10^{-16}$	$Q_F < 10^{-16}$	
2	$\text{model}_{2,2,1}$	23477 ± 144	120755 ± 24037 Lp	⋯	⋯	⋯	↑	↑	3hjd14R221S.dat
Um	$\eta = 12$	0.031 ± 0.002	0.5 ± 0.9 Ad	⋯	⋯	⋯	$F = 16$	$F = 12$	
Ad, Lp	$R = 0.2534$					⋯	$Q_F = 5.6 \times 10^{-15}$	$Q_F < 10^{-16}$	
3	$\text{model}_{3,2,1}$	14197 ± 134	22873 ± 289	97561 ± 23777 Lp	⋯	⋯	⋯	↑	3hjd14R321S.dat
Um	$\eta = 17$	0.010 ± 0.001	0.029 ± 0.002	0.3 ± 0.8 Ad	⋯	⋯	⋯	$F = 7.9$	
Ad, Lp	$R = 0.2424$					⋯	⋯	$Q_F = 2.1 \times 10^{-7}$	
4	$\text{model}_{4,2,1}$	12370 ± 296	15429 ± 222	20037 ± 420	62992 ± 2499	⋯	⋯	⋯	3hjd14R421S.dat
	$\eta = 22$	0.018 ± 0.002	0.008 ± 0.002	0.015 ± 0.002	0.25 ± 0.01	⋯	⋯	⋯	
	$R = 0.2369$					⋯	⋯	⋯	
		Search between 500 and 8000 days							
		Period analysis: Three-signal residuals = 3hjd14R421SResiduals.dat					Fisher Test		
$\mathcal{M}$	Model	P_1 and A_1(days)	P_2 and A_2(days)	P_3 and A_3(days)		$\text{model}_{2,2,0}$	$\text{model}_{3,2,0}$		dcm.dat
5	$\text{model}_{1,2,0}$	679.7 ± 0.6	⋯	⋯		↑	↑		3hjd58R120S.dat
	$\eta = 6$	0.0072 ± 0.0009	⋯	⋯		$F = 6.0$	$F = 5.8$		
	$R = 0.2286$					$Q_F = 1.8 \times 10^{-5}$	$Q_F = 1.2 \times 10^{-8}$		
6	$\text{model}_{2,2,0}$	679.6 ± 0.4	3387 ± 17	⋯		⋯	↑		3hjd58R220S.dat
	$\eta = 11$	0.0074 ± 0.0007	0.0051 ± 0.0008	⋯		⋯	$F = 5.6$		
	$R = 0.2247$			⋯		⋯	$Q_F = 4.2 \times 10^{-5}$		
7	$\text{model}_{3,2,0}$	676 ± 1 If	678 ± 12 If	3387 ± 18		⋯	⋯		3hjd58R320S.dat
Um	$\eta = 16$	0.011 ± 0.002	0.016 ± 0.004	0.0053 ± 0.0008		⋯	⋯		
If	$R = 0.2211$					⋯	⋯		

Note. Otherwise as in Table A7.

Table A12
All Data: Comparison of Circular Orbit Results

Col. 1	Col. 2	Col. 3	Col. 4	Col. 5	Col. 6
	Table A8: Circular $e = 0 \equiv K_2 = 1$			Table A9: Circular $e = 0 \equiv K_2 = 1$	
	Best model $\mathcal{M} = 4 + 5 + 9$			Best model $\mathcal{M} = 2 + 5$	
	(days)	(days)		(days)	(days)
$\mathcal{M} = 4$	$P_4 = 145456 \pm 16180$ Lp	$A_4 = 0.9 \pm 0.2$ Ad	$\mathcal{M} = 2$	$P_5 = 120740 \pm 41002$ Lp	$A_5 = 0.6 \pm 0.5$ Ad
$\mathcal{M} = 4$	$P_3 = 42610 \pm 556$	$A_3 = 0.088 \pm 0.004$	$\mathcal{M} = 2$	$P_4 = 42422 \pm 640$	$A_4 = 0.08 \pm 0.01$
$\mathcal{M} = 4$	$P_2 = 24773 \pm 526$	$A_2 = 0.018 \pm 0.001$	$\mathcal{M} = 2$	$P_3 = 24247 \pm 872$	$A_3 = 0.018 \pm 0.002$
$\mathcal{M} = 4$	$P_1 = 12352 \pm 58$	$A_1 = 0.0188 \pm 0.0006$	$\mathcal{M} = 2$	$P_2 = 12294 \pm 109$	$A_2 = 0.018 \pm 0.002$
$\mathcal{M} = 5$	$P_1 = 10175 \pm 83$	$A_1 = 0.0087 \pm 0.0005$	$\mathcal{M} = 2$	$P_1 = 10144 \pm 30$	$A_1 = 0.0097 \pm 0.0004$
$\mathcal{M} = 9$	$P_3 = 7360 \pm 55$	$A_1 = 0.0056 \pm 0.0006$	$\mathcal{M} = 5$	$P_3 = 7395 \pm 37$	$A_3 = 0.0061 \pm 0.0006$
$\mathcal{M} = 9$	$P_1 = 680.7 \pm 0.4$	$A_1 = 0.0056 \pm 0.0006$	$\mathcal{M} = 5$	$P_3 = 680.7 \pm 0.5$	$A_1 = 0.0057 \pm 0.0009$
$\mathcal{M} = 9$	$P_2 = 2986 \pm 39$	$A_2 = 0.0031 \pm 0.0008$			

Note. Cols. 1–3: periods and amplitudes of best model $\mathcal{M} = 4 + 5 + 9$ from Table A8. Cols. 4–6: periods and amplitudes of best model $\mathcal{M} = 2 + 6$ from Table A9.

Table A13
All Data: Comparison of Eccentric and Circular Orbit Results

Col. 1	Col. 2	Col. 3	Col. 4	Col. 5	Col. 6	Col. 7	Col. 8
	Table A7: Eccentric $e > 0 \equiv K_2 = 2$			Table A9: Circular $e = 0 \equiv K_2 = 1$		Connection	Effect
$\mathcal{M} = 3$	$P_{e,5} = 79999 \pm 1216$	$A_{e,5} = 0.287 \pm 0.005$	$\mathcal{M} = 2$	$P_{c,7} = 120740 \pm 41002$ Lp	$A_{c,7} = 0.6 \pm 0.5$ Ad	$P_{e,5} \approx 1 \times P_{c,7}$	Correct-*p*
			$\mathcal{M} = 2$	$P_{c,6} = 42422 \pm 640$	$A_{c,6} = 0.08 \pm 0.01$	$P_{e,5} \approx 2 \times P_{c,6}$	Half-*p*
$\mathcal{M} = 3$	$P_{e,4} = 24742 \pm 141$	$A_{e,4} = 0.029 \pm 0.001$	$\mathcal{M} = 2$	$P_{c,5} = 24247 \pm 872$	$A_{c,5} = 0.018 \pm 0.002$	$P_{e,4} \approx 1 \times P_{c,5}$	Correct-*p*
			$\mathcal{M} = 2$	$P_{c,4} = 12294 \pm 109$	$A_{c,4} = 0.018 \pm 0.001$	$P_{e,4} \approx 2 \times P_{c,4}$	Half-*p*
$\mathcal{M} = 3$	$P_{e,3} = 20358 \pm 128$	$A_{e,3} = 0.013 \pm 0.001$	$\mathcal{M} = 2$	$P_{c,3} = 10144 \pm 91$	$A_{c,3} = 0.0097 \pm 0.0004$	$P_{e,3} \approx 2 \times P_{c,3}$	Half-*p*
$\mathcal{M} = 6$	$P_{e,2} = 7269 \pm 29$	$A_{e,2} = 0.007 \pm 0.001$	$\mathcal{M} = 5$	$P_{c,2} = 7395 \pm 37$	$A_{c,2} = 0.0061 \pm 0.0006$	$P_{e,2} \approx 1 \times P_{c,2}$	Correct-*p*
$\mathcal{M} = 6$	$P_{e,1} = 680.4 \pm 0.4$	$A_{e,1} = 0.0064 \pm 0.0007$	$\mathcal{M} = 5$	$P_{c,1} = 680.7 \pm 0.5$	$A_{c,1} = 0.0057 \pm 0.0009$	$P_{e,1} \approx 1 \times P_{c,1}$	Correct-*p*

Note. Cols. 1–3: eccentric orbit results (Table A7). Cols. 4–6: circular orbit results (Table A9). Col. 7: connection between eccentric and circular orbit periods. Col. 8: Effects are explained in Section 5.5. Eccentric and circular orbit periods are denoted by subscripts "e" and "c," respectively.

Table A14
Eccentric Orbit Results for Three Samples

Col. 1	Col. 2	Col. 3	Col. 4	Col. 5	Col. 6	Col. 7	Col. 8	Col. 9	Col. 10
	All data: $\Delta T = 86{,}171^{\mathrm{d}}$, $n = 2224$			First 226^{y} data: $\Delta T = 82602^{\mathrm{d}}$, $n = 2174$			First 185^{y} data: $\Delta T = 67680^{\mathrm{d}}$, $n = 1731$		
	Table A7			Table A10			Table A11		
	(days)	(days)		(days)	(days)		(days)	(days)	Effect
$\mathcal{M} = 3$	$P_3 = 79999 \pm 1216$	$A_3 = 0.287 \pm 0.005$	$\mathcal{M} = 3$	$P_3 = 78589 \pm 2004$	$A_3 = 0.282 \pm 0.007$	$\mathcal{M} = 4$	$P_4 = 62992 \pm 2499$	$A_4 = 0.25 \pm 0.01$	Correct-*p*
$\mathcal{M} = 3$	$P_2 = 24742 \pm 142$	$A_2 = 0.029 \pm 0.001$	$\mathcal{M} = 3$	$P_2 = 24870 \pm 190$	$A_2 = 0.030 \pm 0.008$	$\mathcal{M} = 4$	$P_1 = 12370 \pm 296$	$A_1 = 0.018 \pm 0.002$	Half-*p*
$\mathcal{M} = 3$	$P_1 = 20358 \pm 128$	$A_3 = 0.013 \pm 0.001$	$\mathcal{M} = 3$	$P_1 = 20592 \pm 172$	$A_1 = 0.014 \pm 0.002$	$\mathcal{M} = 4$	$P_2 = 20037 \pm 420$	$A_2 = 0.015 \pm 0.002$	Correct-*p*
$\mathcal{M} = 6$	$P_2 = 7290 \pm 29$	$A_2 = 0.007 \pm 0.001$	$\mathcal{M} = 6$	$P_2 = 7287 \pm 40$	$A_2 = 0.007 \pm 0.001$	$\mathcal{M} = 4$	$P_3 = 15429 \pm 222$	$A_3 = 0.008 \pm 0.002$	Double-*p*
$\mathcal{M} = 6$	$P_1 = 680.4 \pm 0.4$	$A_2 = 0.0064 \pm 0.0007$	$\mathcal{M} = 6$	$P_1 = 680.3 \pm 0.3$	$A_1 = 0.0063 \pm 0.0008$	$\mathcal{M} = 6$	$P_1 = 679.6 \pm 0.4$	$A_1 = 0.0074 \pm 0.0007$	Correct-*p*
						$\mathcal{M} = 6$	$P_2 = 3387 \pm 17$	$A_2 = 0.0051 \pm 0.0008$	

Note. Cols. 1–3: all data eccentric orbit results (Table A7). Cols. 4–6: first 226^{y} data eccentric orbit results (Table A10). Cols. 7–9: first 185^{y} data eccentric orbit results (Table A11). Col. 10: first 185^{y} data period effect explained in Section 5.5.

Table A15
Detection Limits (Section 6.2)

Col. 1	Col. 2	Col. 3	Col. 4	Col. 5	Col. 6	Col. 7	Col. 8	Col. 9	Col. 10	Col. 11	Col. 12	Col. 13
	m_3	p_3	a_3	a_3	$v_{\min}$	$v_{\max}$	$\Delta a_{\min}$	$\Delta a_{\max}$	$\Delta a_{\min}$	$\Delta a_{\max}$	$\mu_{\min}$	$\mu_{\max}$
	Table 1				During $\Delta t = p_3$		During $\Delta t = 5^{\mathrm{y}}$		During $\Delta t = 20^{\mathrm{y}}$		During $\Delta t = 1^{\mathrm{y}}$	
Candidate	($m_\odot$)	(yr)	(au)	(mas)	(km s^{-1})	(km s^{-1})	(mas)	(mas)	(mas)	(mas)	(mas yr^{-1})	(mas yr^{-1})
Algol H	2.50	219.0	44.7	1569	−2	10	4	225	64	888	0	47
Algol G	0.27	66.4	26.1	911	−8	16	25	427	379	1479	0	89
Algol F	0.43	33.7	16.2	572	−10	18	61	515	739	1144	0	109
Algol E	0.26	27.8	14.6	510	−12	20	79	547	835	1020	0	118
Algol D	0.24	20.0	11.7	416	−14	22	123	591	832	832	0	133
Algol C	1.2	1.9	2.1	75	−30	38	151	151	151	151	0	153

Note. Col. 1: candidate. Cols. 2–5: mass, period, and semimajor axis (m_3, p_3, and a_3). Cols. 6–7: radial velocity limits during $\Delta t = p_3$ (Equations (21)–(22): $v_{\min}$, $v_{\max}$). Cols. 8–11: distance change limits during $\Delta t = 5^{\mathrm{y}}$ and $\Delta t = 20^{\mathrm{y}}$ (Equations (23)–(24): $\Delta a_{\min}$, $\Delta a_{\max}$). Cols. 12–13: proper motion limits (Equations (25)–(26): $\mu_{\min}$, $\mu_{\max}$).

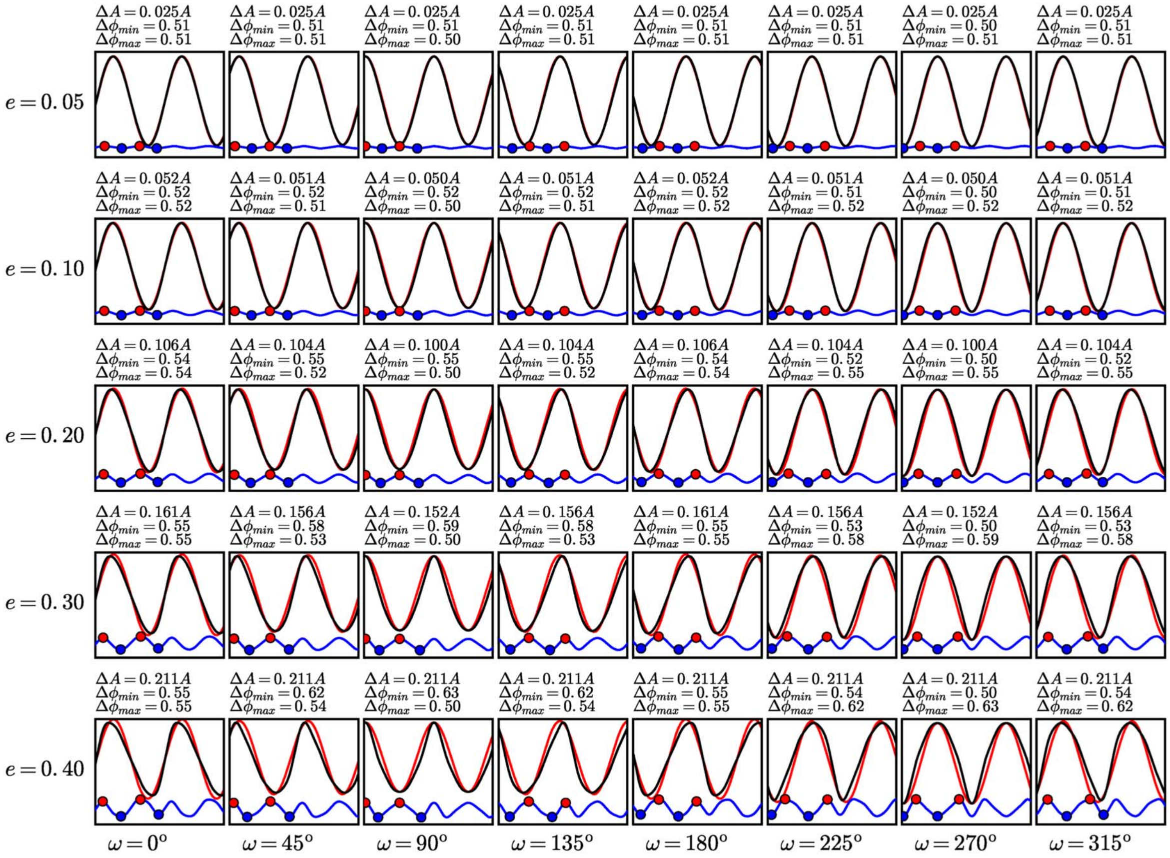

Figure A1. Case I. Black lines show 40 eccentric orbit $O - C_{e>0}$ curves (Equation (A2)) having parameters specified in Table A1 (Case I). Red lines show the respective circular orbit $O - C_{e=0}$ curves (Equation (A1)). Blue lines denote the difference curves $(O - C)_{\rm diff}$ (Equation (A3)). Parameters ΔA, $\Delta\phi_{\rm min}$, and $\Delta\phi_{\rm max}$ (Equations (A4)–(A6)) are given above each panel. Blue and red circles denote the first two $(O - C)_{\rm diff}$ curve minima and maxima. To save space, we show no quantitative *xy*-axis label values, and we offset the $(O - C)_{\rm diff}$ curve below the $O - C_{e>0}$ and $O - C_{e=0}$ curves. Units are $[t]$ = HJD (*x*-axis) and $[O - C]$ = days (*y*-axis).

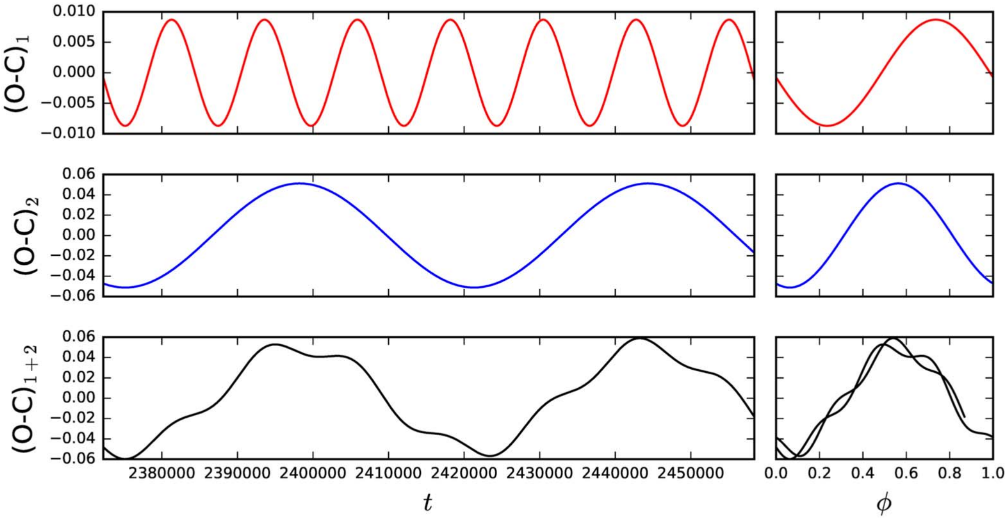

Figure A2. Case II: Interference of two circular orbit $(O - C)_{\rm e=0}$ curves. Red and blue curve periods are $p_1 = 12{,}295^{\rm d}$ and $p_1 = 46{,}159^{\rm d}$, respectively. Other parameters are given in Table A1. The black curve shows the combined $(O - C)_{1+2}$ effect having a period $P_1 = 46{,}122^{\rm d}$. All curves are shown as a function of time (left-hand panels: t) and phase (right-hand panels: ϕ). Left-hand panel units are $[t]$ = HJD and [O − C] = days. Right-hand panel units are $[\phi]$ = dimensionless and [O − C] = days.

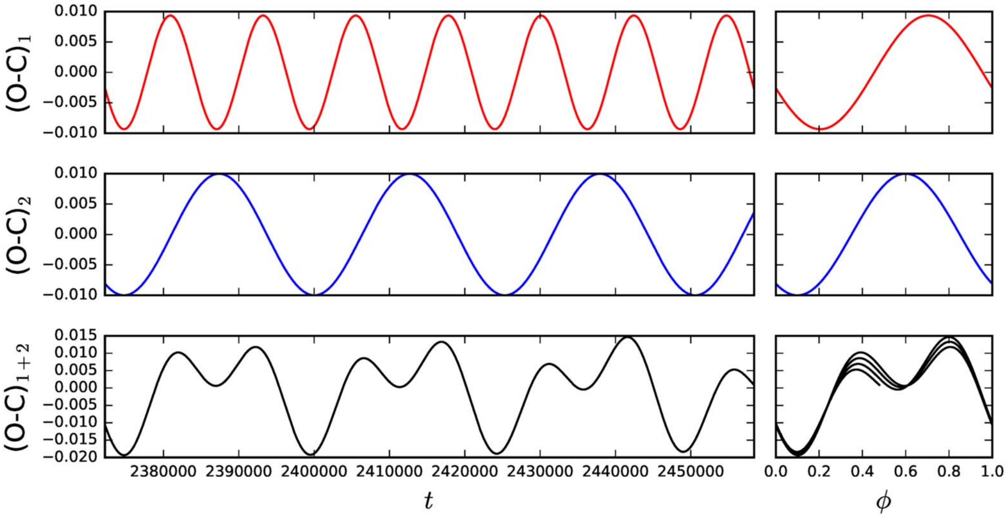

Figure A3. Case III: Interference of two circular orbit $(O-C)_{\mathrm{e}=0}$ curves. Red and blue curve periods are $p_1 = 12{,}304^{\mathrm{d}}$ and $p_2 = 25{,}274^{\mathrm{d}}$. The black curve shows combined $(O-C)_{1+2}$ effect having a period $P_1 = 24{,}771^{\mathrm{d}}$. Otherwise, as in Figure A2.

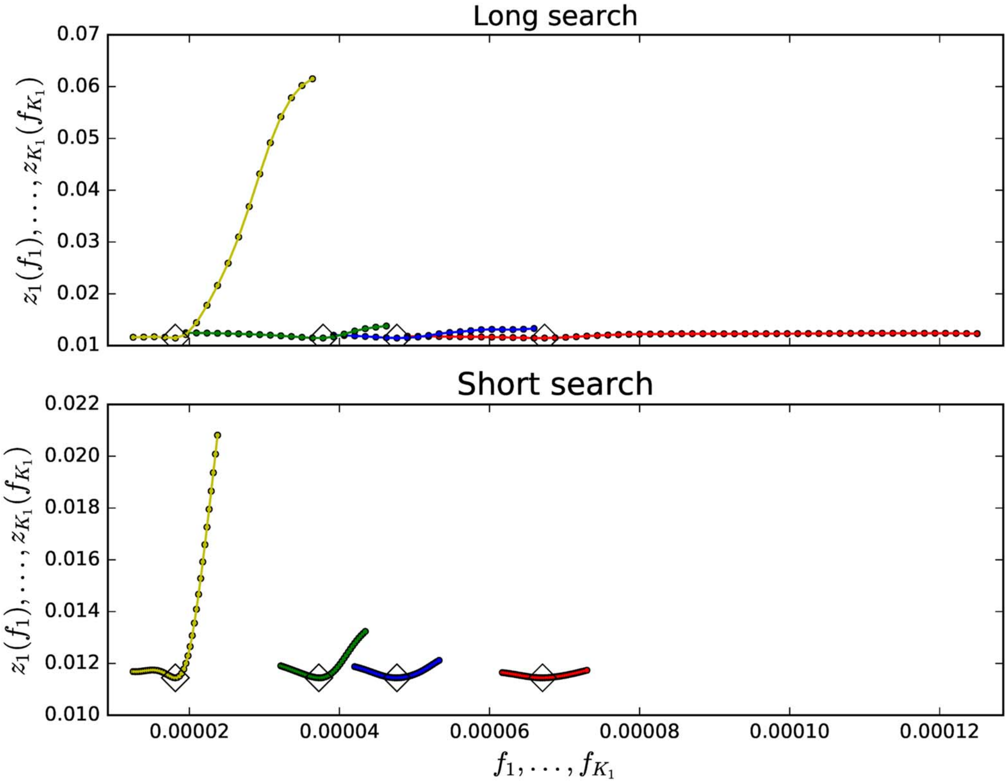

Figure A4. All data: Unstable four-signal eccentric orbit model periodograms (Table A7: $\mathcal{M} = 4$). The upper and lower panels show long- and short-search periodograms (Equation (10)). Their colors are red ($z_1(f_1)$), blue ($z_2(f_2)$), green ($z_3(f_3)$), and yellow ($z_4(f_4)$). Open diamonds denote the locations of the best frequencies. Their corresponding periods are $P_1 = 14{,}912^{\mathrm{d}}$, $P_2 = 20{,}984^{\mathrm{d}}$, $P_3 = 26{,}846^{\mathrm{d}}$, and $P_4 = 55{,}172^{\mathrm{d}}$ (Table A7: $\mathcal{M} = 4$). Units are frequencies $[f_1] =$, ..., $= [f_4] = \mathrm{day}^{-1}$ and periodogram slices $[z_1(f_1)] =$, ..., $= [z_4(f_4)] =$ days.

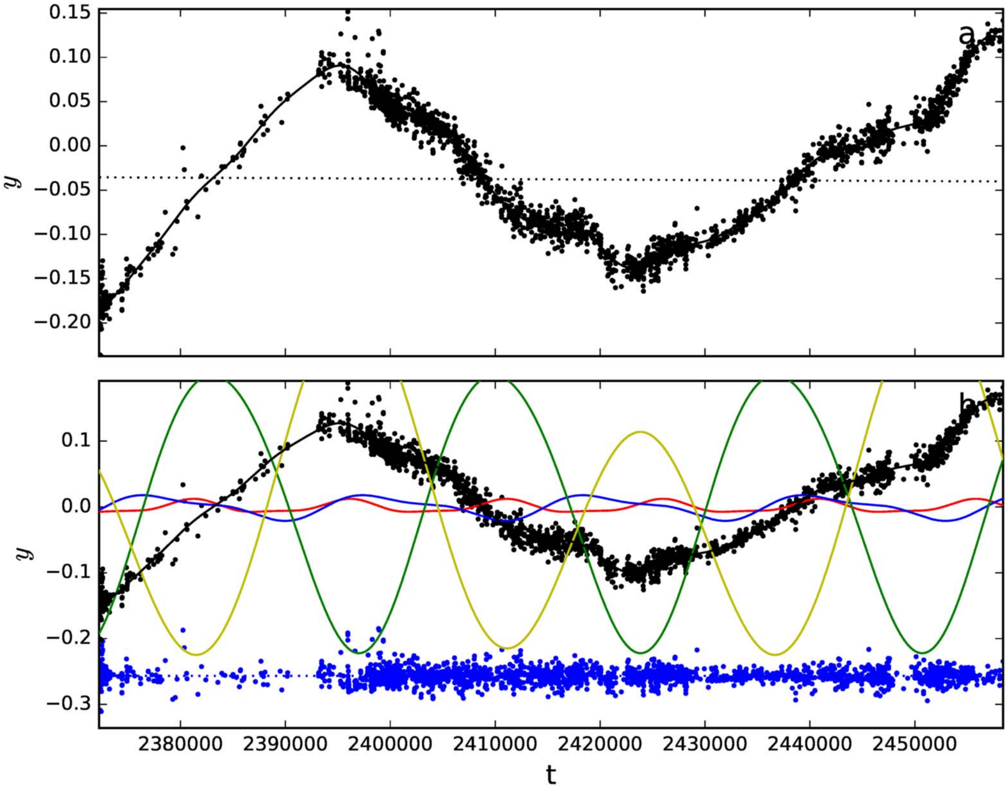

Figure A5. All data: unstable four-signal eccentric orbit model (Table A7: $\mathcal{M} = 4$). (a) Data (black dots), model $g(t)$ (continuous black line), and $p(t)$ trend (dotted black line). (b) Data minus $p(t)$ trend (black dots), $g(t)$ minus $p(t)$ (black line), $g_1(t)$ signal (red line), $g_2(t)$ signal (blue line), $g_3(t)$ signal (green line), and $g_4(t)$ signal (yellow line). Signal periods are $P_1 = 14{,}912^{\rm d}$, $P_2 = 20{,}984^{\rm d}$, $P_3 = 26{,}846^{\rm d}$, and $P_4 = 55{,}172^{\rm d}$. Residuals (blue dots) are offset to -0.15 (dotted blue line). Units are $[t]$ = days and $[y]$ = days.

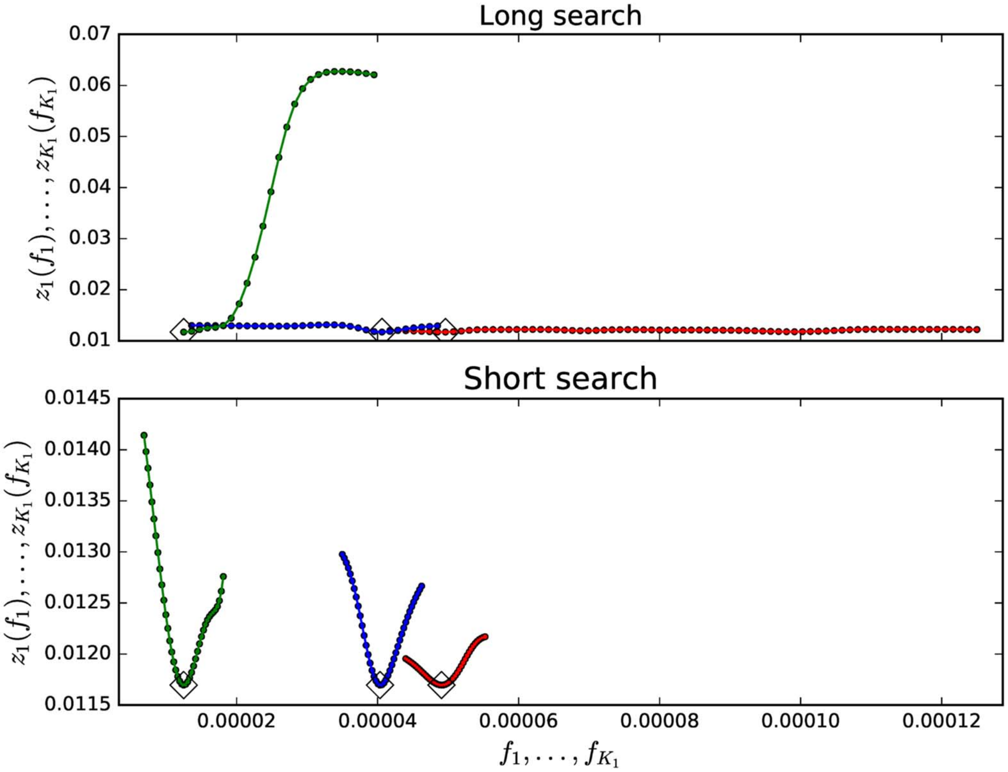

Figure A6. All data: stable three-signal eccentric orbit periodograms (Table A7: $\mathcal{M} = 3$). The best periods are at $P_1 = 20{,}358^{\rm d}$, $P_2 = 24{,}742^{\rm d}$, and $P_3 = 79{,}999^{\rm d}$. Otherwise as in Figure A4.

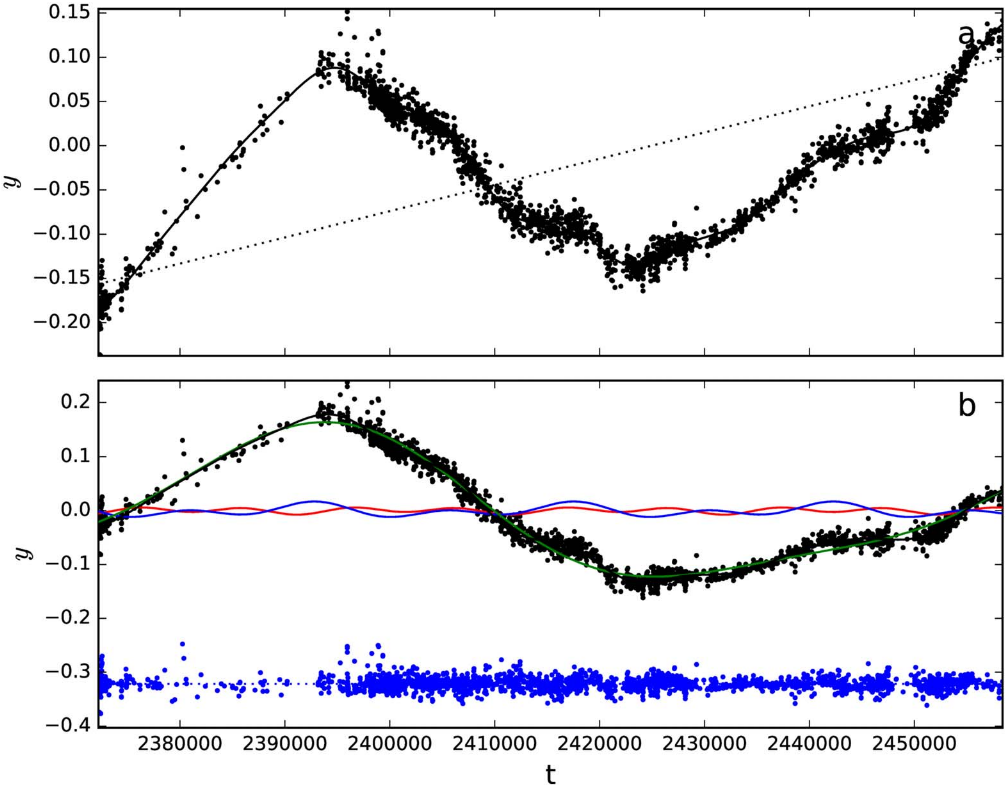

Figure A7. All data: stable three-signal eccentric orbit model (Table A7: $\mathcal{M} = 3$). Signal periods are $P_1 = 20{,}358^{\mathrm{d}}$, $P_2 = 24{,}742^{\mathrm{d}}$, and $P_3 = 79{,}999^{\mathrm{d}}$. Otherwise as in Figure A5.

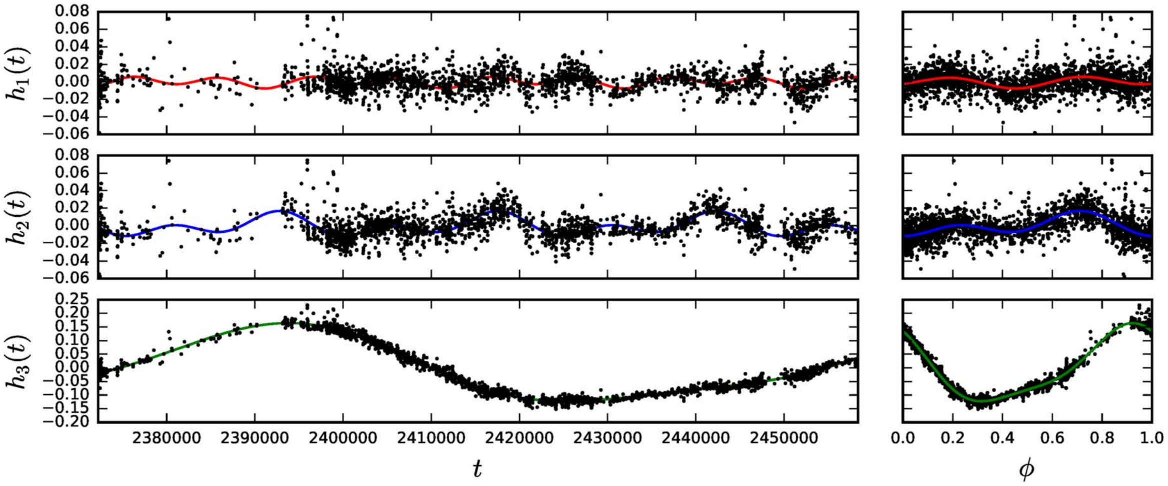

Figure A8. All data: three signals $y_{i,j}$ (Equation (20)) of the stable eccentric orbit model (Table A7: $\mathcal{M} = 3$). Each signal is plotted as a function of time (t) and phase (ϕ). Signal curve colors are as in Figure A7. Signal periods are $P_1 = 20{,}358^{\mathrm{d}}$, $P_2 = 24{,}742^{\mathrm{d}}$, and $P_3 = 79{,}999^{\mathrm{d}}$. Left-hand panel units are $[t]$ = days and $[h_1(t)] = [h_3(t)] = [h_3(t)]$ = days. Right-hand panel units are $[\phi]$ = dimensionless and $[h_1(t)] = [h_3(t)] = [h_3(t)]$ = days.

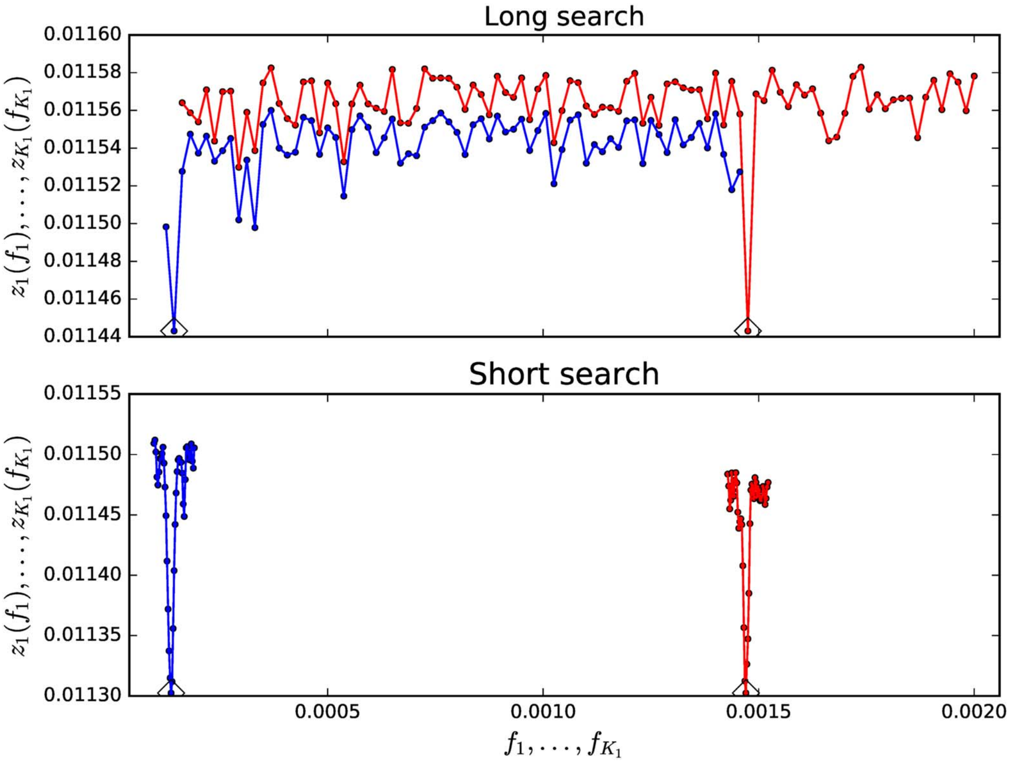

Figure A9. Periodograms for residuals of the $\mathcal{M}=3$ model of all data (Figure A7, blue dots): two-signal model periodograms (Table A7: $\mathcal{M}=6$). The best periods are at $P_1 = 680^{\mathrm{d}}.4$ and $P_2 = 7290^{\mathrm{d}}$. Otherwise as in Figure A4.

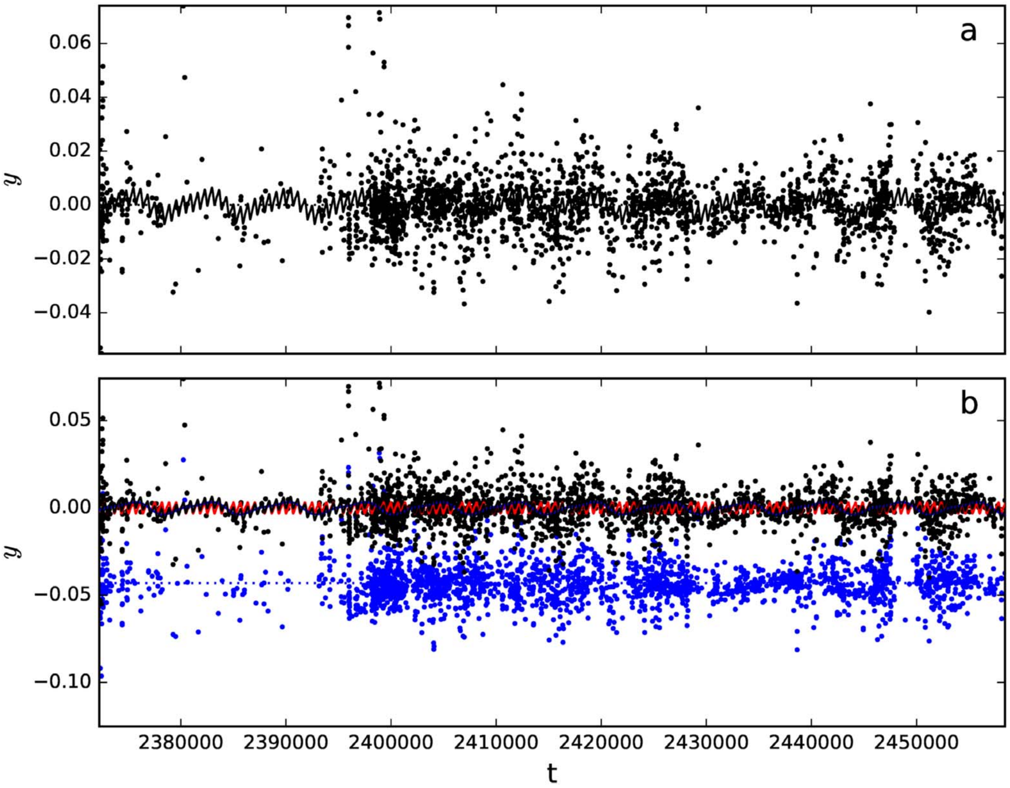

Figure A10. Model for residuals of $\mathcal{M}=3$ model for all data (Figure A7, blue dots): two signals have periods $P_1 = 680^{\mathrm{d}}.4$ and $P_2 = 7290^{\mathrm{d}}$ (Table A7, $\mathcal{M}=6$ model). Otherwise as in Figure A5.

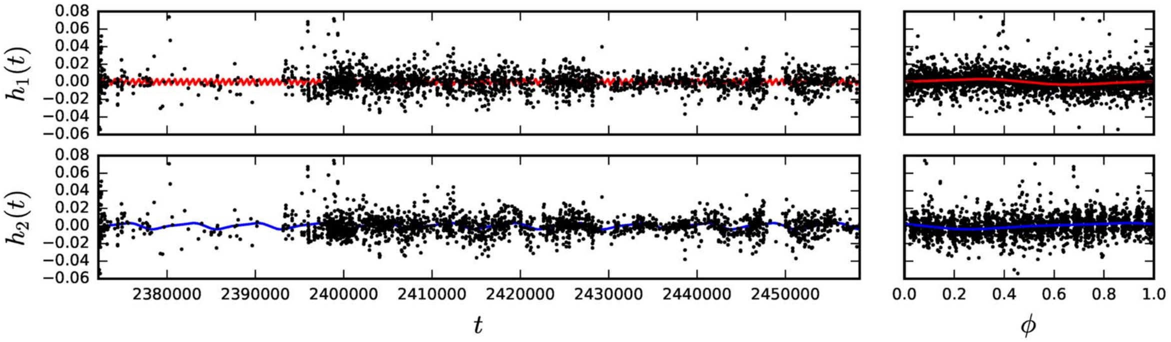

Figure A11. Signals in residuals of the $\mathcal{M} = 3$ model for all data (Figure A7, blue dots): two signals $y_{i,j}$ (Equation (20)) have periods $P_1 = 680^{\rm d}.4$ and $P_2 = 7290^{\rm d}$ (Table A7, $\mathcal{M} = 6$ model). Otherwise as in Figure A8.

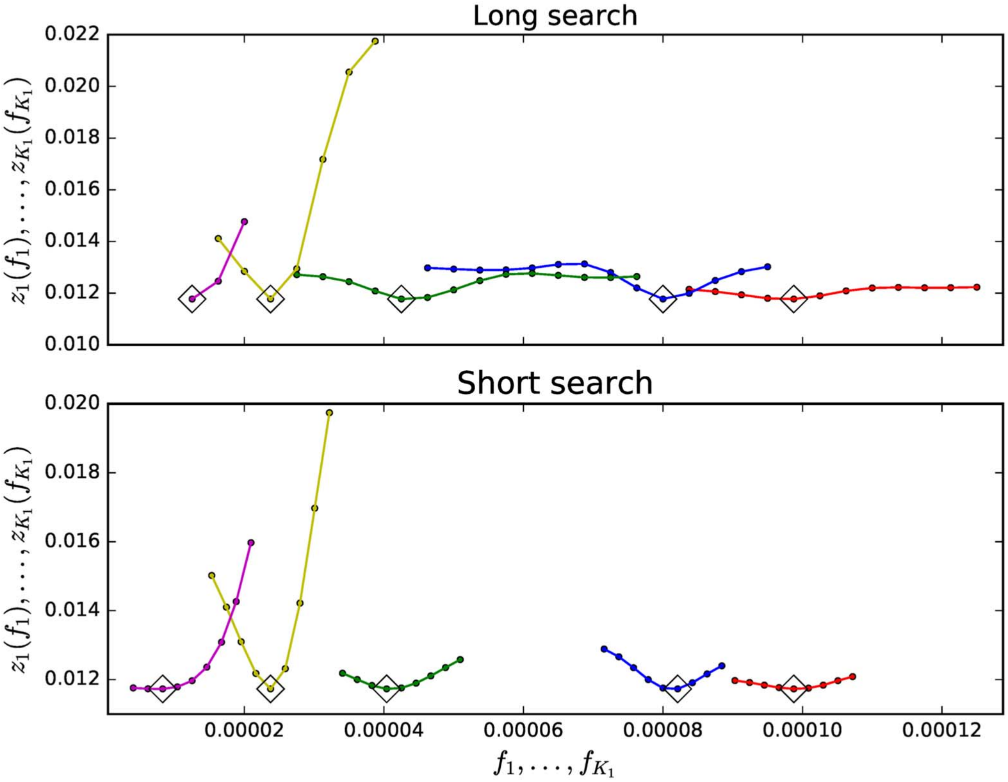

Figure A12. All data: five-signal circular orbit model periodograms (Table A9: $\mathcal{M} = 2$). The best periods are at $P_1 = 10{,}144^{\rm d}$, $P_2 = 12{,}294^{\rm d}$, $P_3 = 24{,}247^{\rm d}$, $P_4 = 42{,}422^{\rm d}$, and $P_5 = 120{,}740^{\rm d}$. Otherwise as in Figure A4.

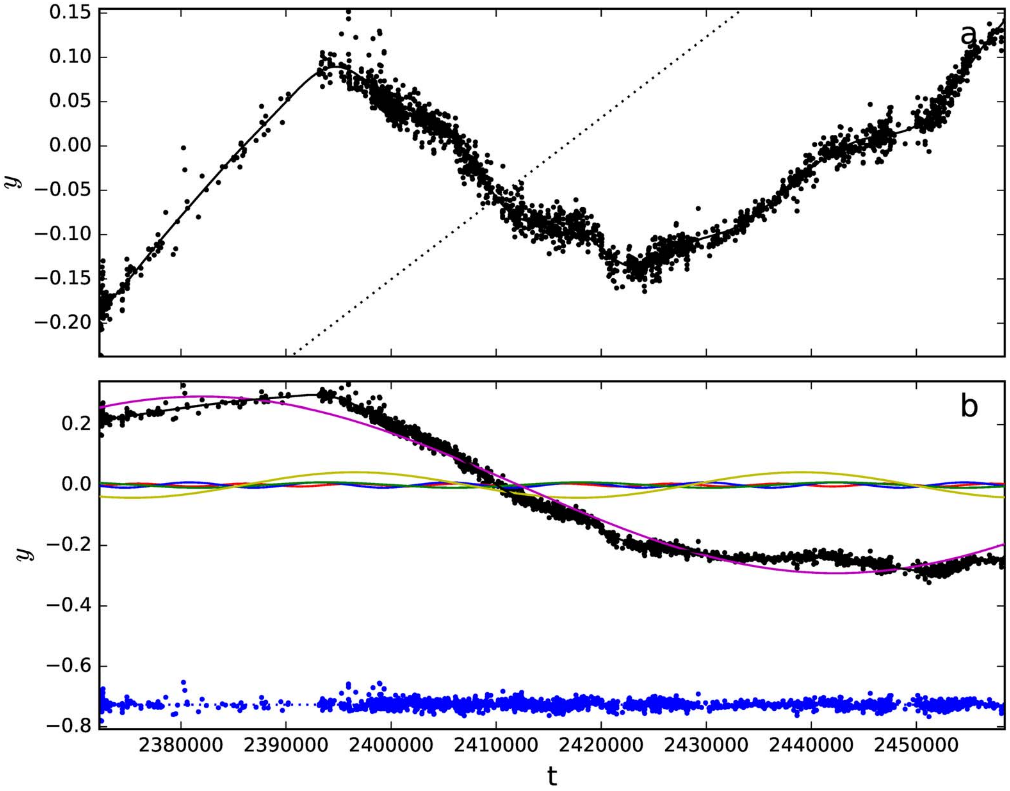

Figure A13. All data: five-signal circular orbit model (Table A9: $\mathcal{M} = 2$). The signal periods are $P_1 = 10{,}144^{\rm d}$, $P_2 = 12{,}294^{\rm d}$, $P_3 = 24{,}247^{\rm d}$, $P_4 = 42{,}422^{\rm d}$, and $P_5 = 120{,}740^{\rm d}$. Otherwise as in Figure A5.

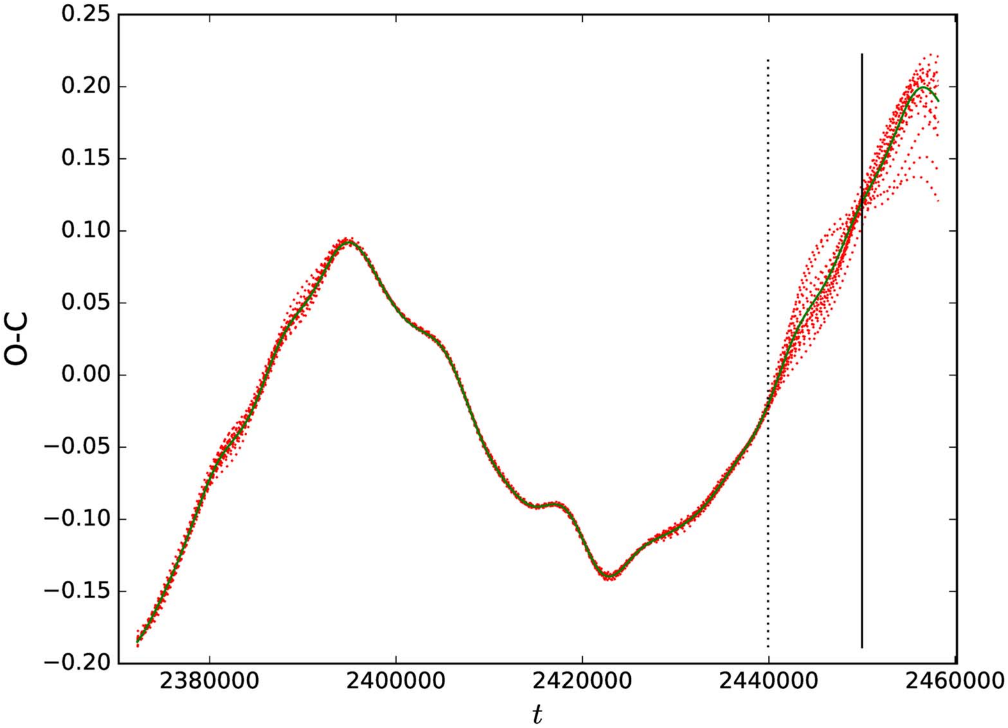

Figure A14. First $185^{\rm y}$ data eccentric orbit analysis (Section 5.3). The green line denotes the $g(t)$ model $\mathcal{M} = 4 + 6$ (Figure 3). Dotted red lines show models for 20 bootstrap samples. The last $50^{\rm y}$ data prediction begins from the dotted vertical line. The continuous vertical line is the data turning point in Figure 3(b). Units are $[t]$ = HJD and $[{\rm O} - {\rm C}]$ = days.

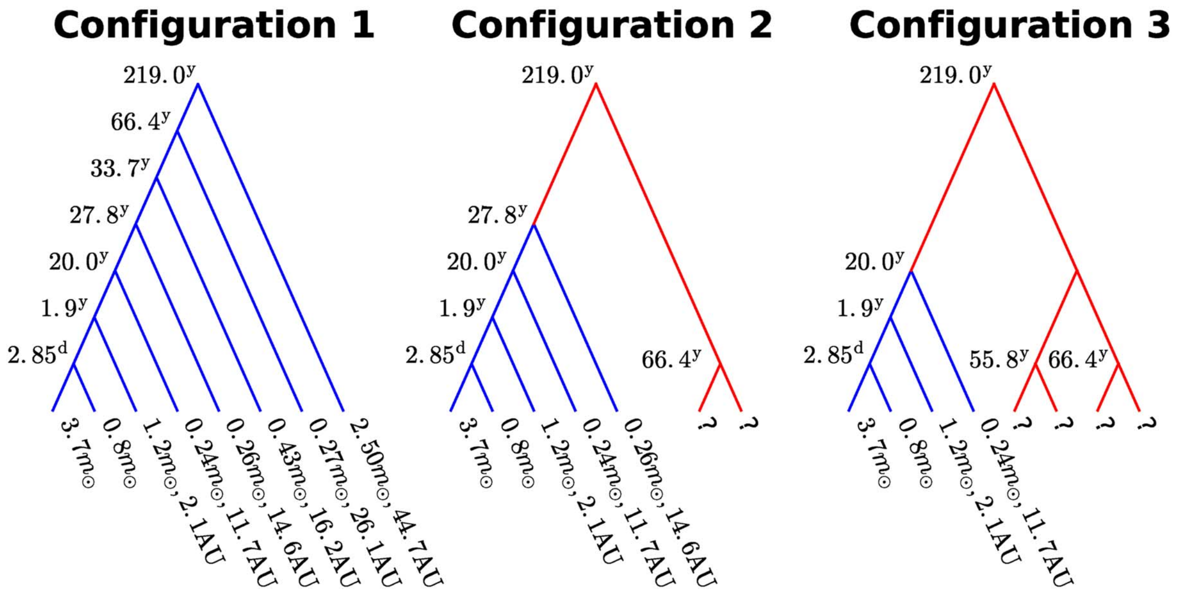

Figure A15. Alternative configurations. Configuration 1: eight members are cEB and six WOSs on circular orbits (Table 1: $i = 90°$). In the next configurations, red lines highlight differences from this first configuration. Configuration 2: seven members are cEB and five WOSs. Red lines illustrate a long-period $66.^{\mathrm{y}}4$ binary on a distant $219.^{\mathrm{y}}0$ orbit. Configuration 3: eight members are cEB and six WOSs. Red lines illustrate two long-period $55.^{\mathrm{y}}8$ and $66.^{\mathrm{y}}4$ binaries on a distant $219.^{\mathrm{y}}0$ orbit.

ORCID iDs

Lauri Jetsu https://orcid.org/0000-0001-6418-5137

References

Allen, M. 2004, Understanding Regression Analysis (New York: Springer), https://books.google.hn/books?id=XQIjngEACAAJ
Applegate, J. H. 1992, ApJ, 385, 621
Baron, F., Monnier, J. D., Pedretti, E., et al. 2012, ApJ, 752, 20
Bayer, A. E., & Seljak, U. 2020, JCAP, 2020, 009
Borkovits, T., Forgács-Dajka, E., & Regály, Z. 2005, in ASP Conf. Ser. 333, Tidal Evolution and Oscillations in Binary Stars, ed. A. Claret, A. Giménez, & J. P. Zahn (San Francisco, CA: ASP), 128
Bours, M. C. P., Marsh, T. R., Breedt, E., et al. 2014, MNRAS, 445, 1924
Curtiss, R. H. 1908, ApJ, 28, 150
Draper, N. R., & Smith, H. 1998, Applied Regression Analysis (New York: Wiley) doi:10.1002/SERIES1345
Efron, B., & Tibshirani, R. 1986, StaSc, 1, 54
Efron, B., & Tibshirani, R. 1994, An Introduction to the Bootstrap (London: Taylor and Francis), https://books.google.fi/books?id=gLlpIUxRntoC
Eggen, O. J. 1948, ApJ, 108, 1
Esmer, E. M., Baştürk, Ö., Hinse, T. C., Selam, S. O., & Correia, A. C. M. 2021, A&A, 648, A85
Fabrycky, D., & Tremaine, S. 2007, ApJ, 669, 1298
Frieboes-Conde, H., Herczeg, T., & Høg, E. 1970, A&A, 4, 78
Goodricke, J. 1783, RSPT, 73, 474
Hajdu, T., Borkovits, T., Forgács-Dajka, E., et al. 2019, MNRAS, 485, 2562
Hoffman, D. I., Harrison, T. E., McNamara, B. J., et al. 2006, AJ, 132, 2260
Horne, J. H., & Baliunas, S. L. 1986, ApJ, 302, 757
Irwin, J. B. 1952, ApJ, 116, 211
Jetsu, L. 2020, OJAp, 3, 4
Jetsu, L., & Pelt, J. 1999, A&AS, 139, 629
Jetsu, L., & Pelt, J. 2000, A&A, 353, 409
Jetsu, L., & Porceddu, S. 2015, PLoSO, 10, e0144140
Jetsu, L., Porceddu, S., Lyytinen, J., et al. 2013, ApJ, 773, 1
Kim, C. H., Kreiner, J. M., Zakrzewski, B., et al. 2018, ApJS, 235, 41
Kiseleva, L. G., Eggleton, P. P., & Mikkola, S. 1998, MNRAS, 300, 292
Kozai, Y. 1962, AJ, 67, 591
Kreiner, J. M., Kim, C.-H., & Nha, I.-S. 2001, An Atlas of O-C Diagrams of Eclipsing Binary Stars (Krakow: Wydawnictwo Naukowe AP)
Kwee, K. K. 1958, BAN, 14, 131
Lehtinen, J., Jetsu, L., Hackman, T., Kajatkari, P., & Henry, G. W. 2011, A&A, 527, A136
Li, M. C. A., Rattenbury, N. J., Bond, I. A., et al. 2018, MNRAS, 480, 4557
Lohr, M. E., Norton, A. J., Payne, S. G., West, R. G., & Wheatley, P. J. 2015, A&A, 578, A136
Manzoori, D. 2016, AstL, 42, 329
Miller, R. 1981, Simultaneous Statistical Inference (New York: Springer), doi:10.1007/978-1-4613-8122-8
Mueller, M. 1995, AcPP, 88A, S49
Porceddu, S., Jetsu, L., Markkanen, T., & Toivari-Viitala, J. 2008, Cambridge Archaeological Journal, 18, 327
Porceddu, S., Jetsu, L., Markkanen, T., et al. 2018, OAst, 27, 232
Powell, B. P., Kostov, V. B., Rappaport, S. A., et al. 2021, AJ, 161, 162
Reinhold, T., Reiners, A., & Basri, G. 2013, A&A, 560, A4
Roy, A. E. 2005, Orbital Motion (Bristol: IOP Publishing)
Soderhjelm, S. 1974, IBVS, 885, 1
Soderhjelm, S. 1975, A&A, 42, 229
Song, S., Mai, X., Mutel, R. L., et al. 2019, AJ, 157, 184
Tokovinin, A. 2021, AJ, 161, 144
Torra, F., Castañeda, J., Fabricius, C., et al. 2021, A&A, 649, A10
van Leeuwen, F. 2007, A&A, 474, 653
Wilson, R. E. 1953, GCRV
Wolf, M., Diethelm, R., & Šarounová, L. 1999, A&A, 345, 553
Zasche, P., & Uhlař, R. 2013, MNRAS, 429, 3472
Zasche, P., & Wolf, M. 2007, AN, 328, 928
Zavala, R. T., Hummel, C. A., Boboltz, D. A., et al. 2010, ApJL, 715, L44